Development of Methods for Improved Data Integrity and Efficient Testing of Wind Tunnel Models for Dynamic Test Conditions in Unsteady and Nonlinear Flight Regimes

Eugene H. D. Heim

Thesis submitted to the Faculty of the Virginia Polytechnic Institute and State University in partial fulfillment of the requirements for the degree of

Masters of Science
In
Aerospace Engineering

Frederick H. Lutze, Advisor
Jay M. Brandon, Mentor
William H. Mason, Chair
Craig A. Woolsey

December 2003
Blacksburg, Virginia

Keywords: Uncertainty, Static, Forced Oscillation, Wind Tunnel Testing, Efficient Testing, Data Integrity

Development of Methods for Improved Data Integrity and Efficient Testing of Wind Tunnel Models for Dynamic Test Conditions in Unsteady and Nonlinear Flight Regimes

Eugene H. D. Heim

(ABSTRACT)

Today's high performance aircraft are operating in expanded flight envelopes, often maneuvering at high angular rates at high angles-of-attack, even above maximum lift. Current aerodynamic models are inadequate in predicting flight characteristics in the expanded envelope, such as rapid aircraft departures and other unusual motions. Unsteady flows of aircraft are of real concern. The ability to accurately measure aerodynamic loads directly impacts the ability to accurately model and predict flight. Current wind tunnel testing techniques do not adequately address the data fidelity of a test point under the influence of fluctuating loads and moments. Additionally, forced oscillation test techniques, one of the primary tools used to develop dynamic models, do not currently provide estimates of the uncertainty of the results during an oscillation cycle. Further, in testing models across a range of flight conditions, there are frequently parts of the envelope which are well behaved and require few data points to arrive at a sound answer, and other parts of the envelope where the responses are much more active and require a large sample of data to arrive at an answer with statistical significance. Currently, test methods do not factor changes of flow physics into data acquisition schemes, so in many cases data are obtained over more iterations than required, or insufficient data may be obtained to determine a valid estimate. Methods of providing a measure of data integrity for static and forced oscillation test techniques are presented with examples. A method for optimizing required forced oscillation cycles based on decay of uncertainty gradients and balance tolerances is also presented.

Acknowledgements

Foremost, appreciation goes to my parents, Linda Chase and Richard Heim. It was your encouragement and support, which enabled me to reach for my dreams. The ethics and values you instilled in me granted me the ability to achieve my goals far beyond my own expectations. I hope you can share in the joy of my accomplishments and be proud of your son.

My mentor, Jay Brandon, has been directly involved with many aspects of my work. But far more than that you have exemplified what a real engineer should be. I have been shocked by your brilliancy, diligence, efficiency, and pedagogical excellence for which I will be aspiring for all my life. Your guidance, patience, and selflessness during the development of this work are greatly appreciated. The experience working with you has been an enjoyable time period that I will never forget. I have been fortunate to have the opportunity to work under your supervision and I look forward with great anticipation to working and learning from you for many years to come.

I must express my deepest gratitude to all of my future colleagues in the Vehicle Dynamics Branch as well as the Dynamics and Controls Branch. None of this work would have been imaginable without the immeasurable contributions from you all. In particular I would like to thank Norma Campbell, Fred Lallman and Wes O'Neal for their countless hours of assistance with the data acquisition system, data reduction processes and instrumentation. The wind tunnel tests that provided the data necessary for this work would not have been possible without the extraordinary commitment to excellence of Gene Adams and Charley Debro or without the leadership of Gautam Shah and dedication of Kevin Cunningham, John Foster, Sue Grafton, Eric Stewart and Dan Vicroy. Of course, none of this work would have been possible without the devotion and leadership of my Branch Secretaries Lori Brown and Susan Conry and my Branch Head Daniel Murri. I am immensely proud and eternally grateful to be part of this team.

I also want to express my appreciation to my committee members: Dr. William Mason and Dr. Craig Woolsey. You have provided, with kindness, your insight and suggestions, which improved my understanding, and broadened my vision.

Dr. Hugh Coleman, Dr. Glenn Steele and Dr. Michael Hemsch provided invaluable statistical insight necessary for the uncertainty analysis. I thank you. It is with absolute certainly I can say I look forward to working with you again.

I wish to thank Mike Czarnecki and Richard Faison of Wyle Laboratories, Jim Hallissy of the Research Facilities Branch, Lou Lang of Neff Instruments Corporation, and Ray Rhew of the Advanced Model and Sensor Systems Branch. Thank you for all the help you gave me during this work.

I have no shame in admitting this thesis was a long and arduous process. I must express my gratefulness to my family and friends for their patience, selflessness, and above all care-packages, emails, phone calls, and distractions. I am truly grateful to be blessed with such understanding and loving family and friends.

Finally, I wish to express my gratefulness for my advisor, the late Dr. Frederick H. Lutze, who passed away December 2, 2003. Dr. Lutze exemplified the ideals of integrity, tuff competence and pedagogical excellence. He was so much more than a professor and an advisor; he was a roll model and an inspiration for all of us. I can say without reservation I am a better

engineer and a better man for having known him. The world is a little dimmer now he is gone but it is a whole lot brighter because he was here.

Eugene H. D. Heim

December 2003
Blacksburg, Virginia

Table of Contents

Nomenclature

Roman

A	Axial force
a', b', c'	Coefficients of test section calibration factor
B	Estimate of systematic error
b	Wing span
b^2	Estimate of variance of systematic error
b_{xy}	Estimate of covariance of systematic error between b_x and b_y
C	Linear interaction coefficient matrix
c_{11}, c_{12}, c_{13}, etc.	Coefficients of linear interaction matrix
Cal.	Indicates from a calibration
$\bar{c}$	Mean aerodynamic chord
c_{prime}	Test section calibration factor
C_X	Aerodynamic coefficients
F	Indicates balance voltages
FS	Full-scale range
g_m	10-cycle moving average of maximum gradient of rolling standard deviation of interpolated points around an oscillation cycle
H	Coverage factor
J	Number of independent variables
K	Generic non-dimensionalization constant
k	Balance sensitivity constant vector
L	Length of model
l	Rolling moment
m	Pitching moment
M	Inverse linear interaction matrix
m_q	Slope of pressure transducer calibration constants
$[m_{i,j}]$	Elements of M
N	Number of readings or Normal force where appropriate
n	Yawing moment
NEFF	Indicates error from data acquisition system
new	Indicates new variable; not used in determination of regression coefficients
p	y-intercept of linear fit
P	Estimate of precision limit
$P_{Cal.}$	Pressure applied during the pressure transducer calibration.
P_p	Pressure
Prob	Probability
P_x	Precision limit
$P_{\bar{x}}$	Precision limit of the mean

Q	Common error sources for x_i and x_k
q	Dynamic pressure
$\overline{q}$	Average Dynamic pressure
q_m	Measured dynamic pressure
r	Result
$\bar{r}$	Mean of multiple results
s	Slope of linear fit
S	Wing reference area
S^2	Estimate of variance of random error
S_r	Standard deviation of multiple results
$S_{\bar{r}}$	Standard deviation of the mean of multiple results
S_x	Sample standard deviation
$S_{\bar{x}}$	Sample standard deviation of the mean
S_{xy}	Estimate of covariance of random error between S_x and S_y
t	Time
U	Uncertainty
u	Estimate of uncertainty
u^2	Estimate of variance of total errors
V	Excitation voltage of balance
$V_{Cal.}$	Voltage from pressure transducer calibration
V_p	Voltage of pressure transducer during calibration
V_q	Voltage of pressure transducer during testing
x	Generic variable
$\bar{x}$	Mean of a sample
$\overline{X}$	Average balance loads
X	Aerodynamic loads
X_I	Balance loads where I can be R for run or T for tare
y	Generic variable
Y	Side force

Greek

α	Angle-of-attack
β	Systematic error of parent population unless otherwise noted
δ	Total measurement error
ε	Random error of parent population
φ	Gradient
$\overline{\theta}$	Average angular position
$\theta_x, \theta_y, \theta_z$	Rotation angle about body x, y or z axis
κ	Diagonal matrix of balance sensitivities
μ	Mean of parent population
σ	Standard deviation of the parent population
$\overline{\sigma}$	Standard deviation of the mean of the parent population

σ^2	Variance
τ	Normalized deviation of reading from parent population mean
ψ	Model yaw angle

Subscripts

A	Axial force
Cal.	Indicates from a calibration
c_{prime}	Test section calibration factor
C_X	Aerodynamic coefficients
F	Indicates balance voltages
FS	Full-scale range
h,i,j,k	Indices
int	Indicates interpolated
k	Balance sensitivity constant vector
l	Rolling moment
m	Pitching moment
max	Indicates maximum value
$m_{i,j}$	Coefficients of *M*
N	Normal force
n	Yawing moment
NEFF	Indicates error from data acquisition system
new	Indicates new variable; not used in determination of regression coefficients
q	Dynamic pressure
$\overline{q}$	Average Dynamic pressure
q_m	Measured dynamic pressure
r	Result
$\overline{r}$	Mean of multiple results
R	Indicates run
-regress	Indicates uncertainty from a regression
RSS	Indicates root-sum-square
T	Indicates tare
t	Time
true	Indicates true value
U	Uncorrected loads as opposed to uncertainty
V_q	Voltage of pressure transducer
x	Generic variable
$\overline{x}$	Mean of a sample
$\overline{X}$	Average balance loads
X_I	Balance loads
y	Generic variable
Y	Side force
z	Indicates a “zero” measurement
α	Angle-of-attack

$\bar{\theta}$	Average angular position
θ	Angular position

List of Tables

List of Figures

1 Introduction

1-1 Background of testing

1-1.1 Static test considerations

Static wind tunnel tests are inherently "un-static" or unsteady with time. These unsteady effects are usually small at low angles-of-attack, α and have traditionally been time averaged or simply filtered out and thus assumed negligible. Unsteady aerodynamics become significant near maximum lift and often result in stall or loss of control departures in flight. Repeats of static tests at high α often result in multiple state, discontinuous data over very small increments in α and sideslip. For example reference [1] described several repeat static α-sweeps of the F/A-18E which exhibited discontinuous multiple states, i.e. opposite signs, in rolling moment around α = 15º. Even though we can acknowledge that the concept of "static" aerodynamics is an ideal simplification, current data analysis and modeling techniques depend on that assumption. Therefore, a repeatable value of the forces or moments needs to be arrived at to fulfill the need for static data, and quantification of the confidence bounds due not only unsteady aerodynamic effects, but also the other factors involved in test measurements need to be available to enable useful interpretations of the data.

1-1.2 Dynamic data

Forced oscillation and rotary balance testing are the key sources of dynamic aerodynamic information for aircraft simulation and modeling. The rotary balance tests result in steady-state rotational rate aerodynamic information as the model is rotated about its velocity vector. The forced oscillation tests provide aerodynamic measurements while the model is sinusoidally oscillated about one of the body axes. Traditionally only frequencies near the Dutch roll natural frequency and short period natural frequency of the aircraft were tested over small amplitudes to estimate damping derivatives. These damping derivatives were then assumed to be linear with angular rate. Forced oscillation tests have documented effects of reduced frequency in the 1960's [2], however modeling of those effects has only recently begun to be addressed in current testing and simulation. This effect of reduced frequency may be an indication of time-dependence in the aerodynamic response due to unsteady motions of the model. Additional drivers at work in precipitating a change in how forced oscillation data are obtained is that with the improved computer and data storage capabilities today, we are now measuring and saving entire time histories of the forces and moments on the model during the test instead of relying on the traditional hardware-based data reduction schemes which produced the standard linear derivatives.

1-2 Current Testing Needs

Aerodynamic coefficient build-up equations have been used to model aerodynamic characteristics of airplanes for simulation and analysis for over 75 years. Dynamic aerodynamic

characteristics have traditionally been modeled by damping derivatives - linear with angular rate. These damping derivatives traditionally have been obtained using forced oscillation wind tunnel tests. These tests involve measuring forces and moments on a model during sinusoidal oscillations at set frequencies and amplitudes. Although this linear representation of damping effects has worked well in the past, today's high performance aircraft are operating in expanded flight envelopes, often maneuvering at high angular rates at high angles-of-attack, even above maximum lift. Current models are inadequate for predicting flight characteristics in the expanded envelope, such as rapid aircraft departures and other unusual motions [3].

1-2.1 Nonlinear and unsteady flows in static tests

Static aerodynamic information is essential for any aerodynamic model as it provides the basis for predicting flight performance and aircraft stability. The expanded envelope of today's high performance aircraft requires ground testing at high angles-of-attack in nonlinear and unsteady flight regimes. Nonlinear aerodynamics has always posed a modeling problem while unsteady effects have traditionally been neglected. However today unsteady flows of aircraft are of real concern as with the pre-production F/A –18E wing drop problem, which prompted the Abrupt Wing Stall (AWS) program [4]. The ability to accurately measure static aerodynamic loads directly impacts the ability to accurately model and predict flight.

1-2.2 New modeling methods for dynamic data

The continuing development of dynamic test methods such as forced oscillation, rotary balance, ramp [5], multi-axis, wide-band sweeps (Schroeder sweeps), oscillatory coning, free-to-roll, etc. have opened new doors for modeling non-linear and unsteady aerodynamics. Recent modeling approaches include single-point [5], indicial [3], fuzzy logic [6], state-space [7], and the list goes on and on. Each of these models had limited success. Moreover, few if any of these papers provided any quantitative assessment of the integrity of the data. In fact it is common practice not to provide uncertainty estimations, instrumentation tolerances or even the range of the data. It is important to know how well the data has been measured that models are being applied to. Large uncertainties may indicate an absence of accounting for some important variables in the test design and math model development, as well as indicating instrumentation uncertainties and flow unsteadiness.

1-3 Current techniques for assessment of data integrity

1-3.1 Test conduct approaches

One proposed method of quantifying data integrity of a wind tunnel test result is through Statistical Quality Control (SQC). SQC requires replication over significant amounts of time with check-standard models for defined test conditions. It is suggested in time all error sources: instrumentation, environmental, human, etc. will be exercised and thus be expressed in the data. The time scales required to exercise all error sources may be on the order of days, months or even years. The information provided by this technique is then used to determine if the location (mean) and dispersion (variance) are moving with time. If location and dispersion are constant

the process is said to be in a state of "statistical control". The dispersion of the check standard is then scaled to give a measure of reproducibility to the customer [8].

The other end of the spectrum is Modern Design of Experiments (MDOE). MDOE involves tailoring the experiment process to meet defined uncertainty objectives through randomization, blocking, and replication. For example, if angle-of-attack, Mach, and Reynolds number were independent variables of the test matrix; these variables would all be changed on every data point and set in random order. One has to wonder what implications this technique has in the presence of unsteady or nonlinear aerodynamics? Blocking, or obtaining, the data in blocks of time is said to 'defend against systematic shifts that can occur from one block of time to another' [9]. The example given for selecting blocks is to schedule block boundaries at staff shift changes. This would reduce unexplained variance due to different techniques and skill levels of the tunnel personnel. Replication is simply repeating the process.

Both SQC and MDOE would require the current static and dynamic testing process to change dramatically and would not provide a mechanism to address data integrity for data already collected.

1-3.2 Uncertainty Analysis

An uncertainty analysis could be done by Monte Carlo simulation where the random errors and elemental systematic errors for each variable are assumed to belong to some distribution, such as a Gaussian distribution. These errors are then randomly selected and added to the assumed true values of the independent variables to get a "measured" value. The measured values are then used in the data reduction equation to calculate a result. This process is repeated N times. The mean and standard deviation are then calculated to estimate the uncertainty.

Uncertainty propagation quantifies the effects of elemental systematic and random uncertainties as they are propagated through data reduction equations to a final result. The technique is best suited for identifying significant error sources during the planning phase of an experiment. However it can be applied during and/or after the experiment is over [10].

1-4 Improved data integrity and efficient testing

Uncertainty propagation is a practical approach for an online real-time estimation of data integrity. The assumptions involved with uncertainty propagation require an understanding of basic statistical concepts such as the mean, standard deviation, and probability distribution function. Methods of providing a measure of data integrity through estimation of propagated uncertainty for body-axis aerodynamic coefficients from static and forced oscillation tests will be presented with examples. Finally, a method of determining how many repeat cycles of forced oscillation testing are needed based on decay of uncertainty gradients and a user specified threshold will be presented. This procedure could reduce test time required to conduct a forced oscillation test substantially while insuring that enough data has been acquired for accurate estimates of the force and moment coefficients. Additionally, the test engineer is provided with quantitative error bound estimates for the forced oscillation test results for the first time.

2 Statistical Considerations for Propagation of Uncertainties

2-1 Basic concepts and definitions

Error or inaccuracy is an inherent part of every measurement. The application of experimental data in an analytical solution requires an understanding of the experimental uncertainties involved. Consider an experiment that requires several measurements or readings of a variable, x. The i and i+1 measurements are shown in Figure 2.1. Assuming the true value of x is known, the inaccuracy or total measurement error, δ of each reading is the difference between the measured value and the true value. The distribution of all possible readings is called the parent distribution or parent population. This distribution often consists of an infinite number of readings. Collecting the parent population experimentally is simply not practical. The set of values obtained is usually a sample of the population. Typically, as more measurements are taken the random variation within the sample would produce a histogram as shown in Figure 2.2. As the number of readings approached infinity the distribution may form a smooth curve such as that in Figure 2.3.

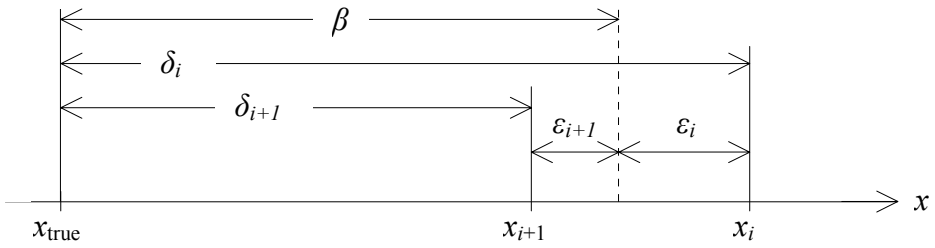

Figure 2.1 Errors in the measurement of a variable x for two readings.

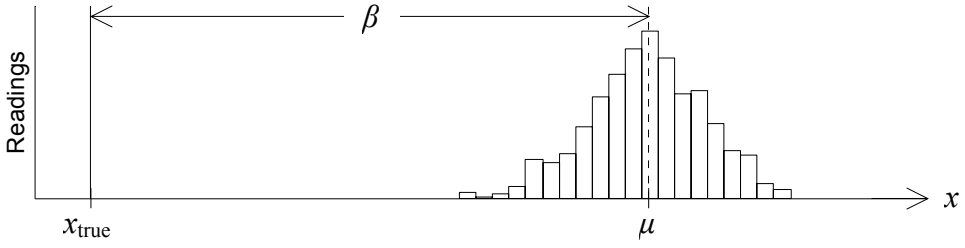

Figure 2.2 Errors in the measurement of a variable x: histogram of multiple readings.

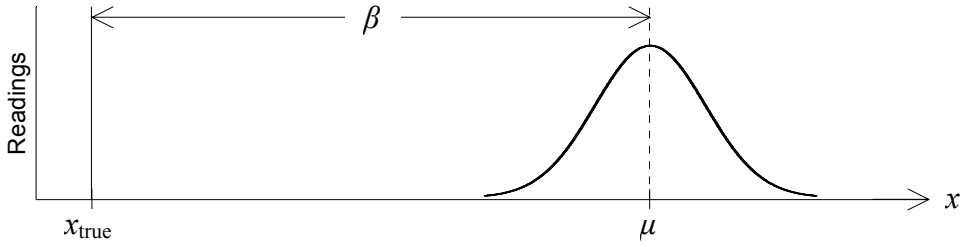

Figure 2.3 Errors in the measurement of a variable x: histogram of an infinite number of readings.

The difference between the mean, μ of an infinite number of readings and the true value is the only theoretical constant component of the total error of each measurement. This systematic component of the error is referred to as the bias error, β. The random component of the total error for each measurement is the precision error, ε.

2-1.1 Gaussian parent distribution

In cases where the variation in the readings come from many small random errors each of equal magnitude, with each error being just as likely to be negative as positive, the smooth distribution of an infinite number of readings coincides with the Gaussian distribution. The Gaussian distribution has been shown to describe more experimental and instrumentation variation than any other statistical distribution. The Gaussian distribution curve, otherwise referred to as the probability density function, has an area of 1. In other words, the probability that any measurement, no matter how unlikely, will be included under the distribution curve is 100%. The probability that a reading, x_i will fall within $\pm\Delta x$ about the mean μ is

$$\text{Prob}(\tau_1) = \int_{-\tau_1}^{\tau_1} \frac{1}{\sqrt{2\pi}} e^{-\tau^2/2} d\tau \tag{2.1}$$

where the normalized deviation of x_i from μ is defined as

$$\tau = \frac{x_i - \mu}{\sigma} \tag{2.2}$$

Here μ and σ are the distribution mean and standard deviation respectively such that

$$\mu = \lim_{N\to\infty} \tfrac{1}{N} \sum_{i=1}^{N} x_i \tag{2.3}$$

$$\sigma = \lim_{N\to\infty} \sqrt{\tfrac{1}{N} \sum_{i=1}^{N} (x_i - \mu)^2} \tag{2.4}$$

The square of the standard deviation is the variance of the distribution.

2-1.2 Confidence intervals of a Gaussian parent distribution

Equation (2.1) has shown we can be 100% confident any reading may exist between ±∞. A more practical "degree of goodness" would be to know the probability any reading would fall under the "meatier" part of the bell curve. If various values of τ are solved for, it can be shown that a τ of 1.96 gives a probability of 95%. Furthermore the probability expression for τ = 1.96 can be written as

$$\text{Prob}(\tau = 1.96) = \text{Prob}(-1.96 \le \frac{x_i - \mu}{\sigma} \le 1.96) = 0.95 \tag{2.5}$$

Rearranging to isolate x_i,

$$\text{Prob}(\mu - 1.96\sigma \le x_i \le \mu + 1.96\sigma) = 0.95 \tag{2.6}$$

we can be 95% confident a single reading x_i will fall within ±1.96σ of the mean of the distribution.

2-1.3 Samples from a Gaussian parent distribution

The set of values obtained when making measurements is only a sample of the infinite parent population, which formed the Gaussian distribution. Therefore the statistical properties of a finite distribution must be considered. The mean of a sample population is defined as

$$\bar{x} = \tfrac{1}{N}\sum_{i=1}^{N} x_i \tag{2.7}$$

where N is the number of readings, x_i. The precision index of a sample population, also known as the sample standard deviation, is given by

$$S_x = \sqrt{\tfrac{1}{N-1}\sum_{i=1}^{N}(x_i - \bar{x})^2} \tag{2.8}$$

where the (N-1) occurs because the sample mean $\bar{x}$ is used instead of μ. One degree of freedom is lost because the same sample used to calculate S_x was already used to calculate $\bar{x}$.

Generally the sample mean and the population mean will not be the same. The question then becomes how close are the two means? What if several samples are collected? Each sample would have a different mean and standard deviation. However, the sample means will be normally distributed with mean μ and standard deviation, $\bar{\sigma}$ such that

$$\bar{\sigma} = \frac{\sigma}{\sqrt{N}} \tag{2.9}$$

This implies the uncertainty of the mean due to random error can be decreased by taking many readings. However, this is a function of rapidly diminishing returns due to the inverse square root. Again, the standard deviation is not known so the sample standard deviation must be used as an estimate such that the sample standard deviation of the mean is defined by

$$S_{\bar{x}} = \frac{S_x}{\sqrt{N}} \tag{2.10}$$

2-1.4 Confidence intervals of a sample population

The parent population standard deviation, σ is not known and must be estimated by the sample standard deviation, S_x. The confidence limit for a sample is the precision limit, P_x where

$$P_x = HS_x \tag{2.11}$$

and the precision limit of the mean is defined as

$$P_{\bar{x}} = HS_{\bar{x}} = \frac{HS_x}{\sqrt{N}} \tag{2.12}$$

The coverage factor, H is generally taken as 2 for a 95% confidence interval. This assumes a large sample size and the parent population has Gaussian distributed error. A coverage factor of 2 will converge to a 95% confidence interval as the sample size approaches infinity. This implies, for $H = 2$, we will be 95% confident that the next reading will be within $\bar{x} \pm P_x$ or μ will be within $\bar{x} \pm P_{\bar{x}}$. A sample size of at least 10 will be considered appropriate for a coverage factor of 2 [11].

2-1.5 Statistical rejection of "wild" readings

Occasionally "wild" measurements are recorded. These points are out of line with the others and are sometimes called "outliers". They have a tendency to displace the sample mean and widen the precision limits. If these points can be verified as a problem with the experiment then they can be discarded. However this is usually not the case and a statistical cleansing must be used. Chauvenet's criterion for statistical rejection of wild readings from a sample population does that. It rejects readings beyond the confidence interval defined by

$$\text{Prob}(\tau) = 1 - \frac{1}{2N} \tag{2.13}$$

where

$$\tau = \frac{x_i - \bar{x}}{S_x} = \frac{x_{\max}}{S_x} \tag{2.14}$$

Here x_{max} is the maximum allowable deviation from the sample mean, $\bar{x}$. Beyond x_{max} the readings are rejected. Chauvenet's criterion can only be used once for a given sample. It may be applied "online" or as readings are being recorded if and only if all previous readings are used in the calculation of the new τ. In other words, rejected readings from the previous N reading sample are used when Chauvenet's criterion is applied for the new N+1 reading sample. Those readings rejected from the N reading sample may or may not be considered "wild" when Chauvenet's criterion is applied to the N+1 reading sample. For example if the 45th reading x_{45} of a sample of 100 readings can be considered "wild" by τ_{100} it may be rejected and $\bar{x}$ and S_x can be recalculated without x_{45}. However, when the next reading x_{101} is recorded, $\bar{x}$ and S_x will in all likelihood change and x_{45} could quite possibly not be considered wild by τ_{101}.

2-1.6 Systematic error estimation

There will always be some uncertainty associated with the estimate of the systematic or bias error, β in a measurement. Typically the bias error estimate, B is taken as the accuracy of the instrument given by the manufacturer or calibration laboratory. As we will see in chapter 4 the term "accuracy" is often used with different meanings from manufacturer to manufacturer and even from calibration laboratory to calibration laboratory. In general every instrument, even if from the same assembly line, has a different systematic error. Manufacturers, sometimes, sample their product line and test the systematic error of instruments in the sample. This bias error estimate should be given with the same level of confidence as the precision limits used by the customer, typically with 95% confidence. However this is not always what is done. The instrument can be sent to a calibration laboratory to be calibrated against a standard, or another instrument that has a much better accuracy. Calibration will minimize the bias error in the instrument but only to the accuracy of the standard used.

2-2 Uncertainty of measurements

Estimations for systematic errors, B and random errors, P have been presented, but what about the overall uncertainty, U in a measurement? There are two ways of combining the two error estimates: straight addition and root-sum-square. We will use the RSS method, as it remains a 95% confidence interval whereas the straight addition increased the uncertainty to 99% confidence limits. The total estimate of the uncertainty thus is given by

$$U_{x_{RSS}} = \left(B^2 + P_x^2\right)^{\frac{1}{2}} \tag{2.15}$$

or

$$U_{\bar{x}_{RSS}} = \left(B^2 + P_{\bar{x}}^2\right)^{\frac{1}{2}} \tag{2.16}$$

2-2.1 Theory of propagation of uncertainties

The uncertainties discussed thus far have been of a single measured variable. Often the result of interest cannot directly be measured and must be computed from a system of measured

variables in some type of data reduction equation. How do the systematic and random errors of each variable propagate through the data reduction equation to yield a systematic and random error in the final result? Consider a Taylor series expansion of the function

$$r = r(x, y) \tag{2.17}$$

of the measured variables x and y such that

$$r_k = r_{true} + \frac{\partial r}{\partial x}(x_k - x_{true}) + \frac{\partial r}{\partial y}(y_k - y_{true}) + ... + H.O.T. \tag{2.18}$$

Neglecting the higher order terms and taking r_{true} to the left-hand side relates the total error in the k^{th} determination of the result r to the total errors in the measured variables such that

$$\delta_{r_k} = r_k - r_{true} = \varphi_x(\beta_{x_k} + \varepsilon_{x_k}) + \varphi_y(\beta_{y_k} + \varepsilon_{y_k}) \tag{2.19}$$

where

$$\varphi_x = \frac{\partial r}{\partial x},\ \varphi_y = \frac{\partial r}{\partial y} \tag{2.20}$$

The variance of the distribution of the total errors for N determinations of the result is given by

$$\sigma_{\delta_r}^2 = \lim_{N\to\infty} \frac{1}{N} \sum_{k=1}^{N} \delta_{r_k}^2 \tag{2.21}$$

Taking the limit as N approaches infinity gives

$$\begin{aligned} \sigma_{\delta_r}^2 &= \varphi_x^2\sigma_{\beta_x}^2 + \varphi_y^2\sigma_{\beta_y}^2 + 2\varphi_x\varphi_y\sigma_{\beta_x\beta_y} \\ &+ \varphi_x^2\sigma_{\varepsilon_x}^2 + \varphi_y^2\sigma_{\varepsilon_y}^2 + 2\varphi_x\varphi_y\sigma_{\varepsilon_x\varepsilon_y} \end{aligned} \tag{2.22}$$

assuming there are no systematic error/random error correlations. Of course in reality the exact σ's are never known so estimates must be used. The estimate of the variance of the distribution of total errors, u_c^2 is

$$\begin{aligned} u_c^2 &= \varphi_x^2 b_x^2 + \varphi_y^2 b_y^2 + 2\varphi_x\varphi_y b_{xy} \\ &+ \varphi_x^2 S_x^2 + \varphi_y^2 S_y^2 + 2\varphi_x\varphi_y S_{xy} \end{aligned} \tag{2.23}$$

Here $b^2$and S^2 are the estimates of the variances of the systematic and random errors respectively and b_{xy} and S_{xy} are the estimates of the covariance of the systematic and random errors respectively in x and y. The variance is the average of the squared deviation of a variable from its mean, the covariance is the average of the products of the deviations of two variables from

their means. The covariance is a measure of correlation between two variables. Consider a general function

$$r = r(x_1, x_2, ..., x_J) \tag{2.24}$$

the estimate of the variance of the distribution of the total errors in the result is

$$\begin{aligned} u_c^2 &= \sum_{i=1}^{J} \varphi_i^2 b_i^2 + 2\sum_{i=1}^{J-1}\sum_{k=i+1}^{J} \varphi_i \varphi_k b_{ik} \\ &+ \sum_{i=1}^{J} \varphi_i^2 \varphi_i^2 + 2\sum_{i=1}^{J-1}\sum_{k=i+1}^{J} \varphi_i \varphi_k S_{ik} \end{aligned} \tag{2.25}$$

The final estimate of the uncertainty of the result is given by

$$U_r = K u_c \tag{2.26}$$

Again, assuming a large sample size ($N > 9$) and Gaussian distributed error, $K = 2$ for a 95% confidence limit. This results in the uncertainty propagation equations

$$B_r^2 = \sum_{i=1}^{J} \varphi_i^2 B_i^2 + 2\sum_{i=1}^{J-1}\sum_{k=i+1}^{J} \varphi_i \varphi_k B_{ik} \tag{2.27}$$

$$(2S_r)^2 = \sum_{i=1}^{J} \varphi_i^2 (2S_i)^2 + 2\sum_{i=1}^{J-1}\sum_{k=i+1}^{J} \varphi_i \varphi_k 4S_{ik} \tag{2.28}$$

where B is given as an estimate of the systematic error with 95% confidence such that $B=2b$. From this point forward ($2S_x$) will be referred to as the precision limit for computational simplification.

2-2.2 Discussion of correlated systematic errors

Correlated errors are those that are not independent of each other. For example if two variables are measured with the same instrument the systematic errors in those variables from that instrument will be the same. Likewise if two instruments are calibrated against the same standard all systematic errors of measurements made with those instruments will be correlated with one another. There is no statistical approach with which to make an estimate of the covariance in systematic errors. The approach that consistently gives the best approximation for correlated systematic errors is [11]

$$B_{ik} = \sum_{j=1}^{Q} (B_i)_j (B_k)_j \tag{2.29}$$

where Q is the number of common elemental error sources for variables x_i and x_k. Equation (2.29) assumes perfect correlation between B_i and B_k. Correlation of systematic errors can sometimes be advantageous. Consider measuring the difference between two readings with the same bias error of the variable x with the same instrument such that

$$r = x_2 - x_1 \tag{2.30}$$

Using the systematic uncertainty propagation equation yields

$$\begin{aligned} B_r^2 &= \varphi_1^2 B_1^2 + \varphi_2^2 B_2^2 + 2\varphi_1\varphi_2 B_{12} \\ &= B_1^2 + B_2^2 - 2B_1 B_2 \\ &= B^2 + B^2 - 2B^2 \\ &= 0 \end{aligned} \tag{2.31}$$

since the bias errors for each measurement are the same. Here the systematic error, B in each reading is correlated, equal and the partial derivatives with respect to each variable are of equal magnitude and opposite sign, which yields a systematic error in the result of zero. If the partial derivatives are not of opposite sign, such as in an average, the correlation will be additive. Consider an average of two readings where each reading again has equal bias, B and the biases are correlated.

$$r = \frac{x_1 + x_2}{2} \tag{2.32}$$

Thus

$$\begin{aligned} B_r^2 &= \varphi_1^2 B_1^2 + \varphi_2^2 B_2^2 + 2\varphi_1\varphi_2 B_1 B_1 \\ &= \left(\frac{1}{2}\right)^2 B^2 + \left(\frac{1}{2}\right)^2 B^2 + 2\left(\frac{1}{2}\right)^2 B^2 \\ &= B^2 \end{aligned} \tag{2.33}$$

as opposed to if the biases are were uncorrelated

$$B_r^2 = \varphi_1^2 B_1^2 + \varphi_2^2 B_2^2 = \left(\frac{1}{2}\right)^2 B_1^2 + \left(\frac{1}{2}\right)^2 B_2^2 = \frac{B^2}{2} \tag{2.34}$$

Equations (2.31), (2.33) and (2.34) demonstrate why careful consideration of correlated systematic error sources should always be part of planning the calibration process.

2-2.3 Random errors direct from the result

Correlated random errors are often too difficult or impossible to predict in the planning phase of an experiment and thus are often not modeled. If multiple results are available the

random uncertainty can be directly calculated from the result. For example consider a result that is determined N times with individual values

$$r_1, r_2, ..., r_N$$

which have an average of

$$\bar{r} = \frac{1}{N}\sum_{k=1}^{N} r_k \tag{2.35}$$

and a standard deviation of

$$S_r = \sqrt{\frac{1}{N-1}\sum_{k=1}^{N}(r_k - \bar{r})^2} \tag{2.36}$$

and

$$S_{\bar{r}} = \frac{S_r}{\sqrt{N}} \tag{2.37}$$

The random uncertainty calculated directly from the result inherently includes the effects of all correlated random error sources.

Random errors are traditionally defined as errors that do not correlate with anything; and example being broadband white noise. Structural dynamics, vortex shedding, the fan beat frequency, etc. along with white noise are potential sources of variation in wind tunnel data. Many of these sources could possibly be correlated with the signal content from the balance and differential pressure transducer. The term "random" will be used to define all content that is unsteady or not fixed.

2-2.4 Uncertainty in regressions

Experimental information is often modeled by a regression. Calibration constants, interpolations, and curve fits of the final results are examples of common regressions of experimental data. The regression, like the final result, inherits the uncertainty of the experimental data. For example consider a linear least-squares curve fit of N data pairs such that

$$y = sx_{new} + p \tag{2.38}$$

where

$$s = \frac{N\sum_{i=1}^{N} x_i y_i - \sum_{i=1}^{N} x_i \sum_{i=1}^{N} y_i}{N\sum_{i=1}^{N}(x_i)^2 - \left(\sum_{i=1}^{N} x_i\right)^2} \tag{2.39}$$

and

$$p = \frac{N\sum_{i=1}^{N}(x_i)^2\sum_{i=1}^{N}y_i - \sum_{i=1}^{N}x_i\sum_{i=1}^{N}(x_i y_i)}{N\sum_{i=1}^{N}(x_i)^2 - \left(\sum_{i=1}^{N}x_i\right)^2} \tag{2.40}$$

The slope, s and y-intercept, p are functions of every data pair. The regression then becomes

$$y = \frac{N\sum_{i=1}^{N}x_i y_i - \sum_{i=1}^{N}x_i\sum_{i=1}^{N}y_i}{N\sum_{i=1}^{N}(x_i)^2 - \left(\sum_{i=1}^{N}x_i\right)^2}x_{new} + \frac{N\sum_{i=1}^{N}(x_i)^2\sum_{i=1}^{N}y_i - \sum_{i=1}^{N}x_i\sum_{i=1}^{N}(x_i y_i)}{N\sum_{i=1}^{N}(x_i)^2 - \left(\sum_{i=1}^{N}x_i\right)^2} \tag{2.41}$$

The uncertainty of y at a measured or specified value of x is found by applying the uncertainty propagation equations [11] to obtain

$$\begin{aligned} U_y^2 = &\sum_{i=1}^{N}\left(\frac{\partial y}{\partial y_i}\right)^2(2S_{y_i})^2 + \sum_{i=1}^{N}\left(\frac{\partial y}{\partial y_i}\right)^2(2S_{x_i})^2 \\ &+ \sum_{i=1}^{N}\left(\frac{\partial y}{\partial y_i}\right)^2 B_{y_i}^2 + 2\sum_{i=1}^{N-1}\sum_{k=i+1}^{N}\left(\frac{\partial y}{\partial y_i}\right)\left(\frac{\partial y}{\partial y_k}\right)B_{y_i y_k} \\ &+ \sum_{i=1}^{N}\left(\frac{\partial y}{\partial x_i}\right)^2 B_{x_i}^2 + 2\sum_{i=1}^{N-1}\sum_{k=i+1}^{N}\left(\frac{\partial y}{\partial x_i}\right)\left(\frac{\partial y}{\partial x_k}\right)B_{x_i x_k} \\ &+ 2\sum_{i=1}^{N-1}\sum_{k=i+1}^{N}\left(\frac{\partial y}{\partial x_i}\right)\left(\frac{\partial y}{\partial y_k}\right)B_{x_i y_k} \\ &+ \left(\frac{\partial y}{\partial x_{new}}\right)^2 B_{x_{new}}^2 + \left(\frac{\partial y}{\partial x_{new}}\right)^2(2S_{x_{new}})^2 \\ &+ 2\sum_{i=1}^{N}\left(\frac{\partial y}{\partial x_{new}}\right)\left(\frac{\partial y}{\partial x_i}\right)B_{x_{new}x_i} + 2\sum_{i=1}^{N}\left(\frac{\partial y}{\partial x_{new}}\right)\left(\frac{\partial y}{\partial y_i}\right)B_{x_{new}y_i} \end{aligned} \tag{2.42}$$

The first seven terms of Eq. (2.42) are the uncertainty contributions of the data pairs. The eighth and ninth terms arise from uncertainty in x_{new}. The tenth term is necessary if the same instrument used to measure x_i is used to measure x_{new} and the last term is only necessary if x_{new} and y_i have common error sources. Note the partial derivatives with respect to x_i and y_i are functions of x_{new}. Reference [11] suggests an additional fit be applied to the uncertainty curve, U_y such that in general

$$U_y = U_{y-regress}(x_{new}) \tag{2.43}$$

Here $U_{y-regress}(x_{new})$ is any curve fit that models the uncertainty common to the experiment, which generated the x_i and y_i data pairs. For example, if a pressure transducer is to be calibrated it is often sent to a calibration laboratory. The calibration lab then generates the x_i and y_i data pairs necessary for the calibration with their instrumentation and standards. The calibrated transducer is then returned to the customer with a calibration report, which includes the calibration x_i and y_i data pairs and calibration constants from a regression of the calibration data If the uncertainties of the x_i and y_i data pairs used in the calibration are available the uncertainty of the regression, $U_{y-regress}(x_{new})$ can be estimated by the first seven terms in Eq. (2.42). The additional uncertainty due to x_{new} from the customer's instrumentation can be combined with that from the calibration so the uncertainty of y is

$$U_y = U_{y-regress}(x_{new}) + \left(\frac{\partial y}{\partial x_{new}}\right)^2 \left(B_{x_{new}}^2 + (2S_{x_{new}})^2\right) \tag{2.44}$$

Every calibration report is different and usually includes a measure of accuracy of the instrument. It is common for this "degree of goodness" to be listed as percent reading or percent full scale of the instrument output. In general these statements are regressions of the calibration data. It is up the experimentalist to discuss the meaning and assumptions of any uncertainty statements with the calibration laboratory.

Analytical determinations of the partial derivatives of higher order polynomial regressions are prohibitive especially with multiple independent variables and numerous data pairs. Numerical approximations are typically used in such situations.

3 Description of Tests

3-1 Introduction

A static wind tunnel test is optimally defined as having steady free stream flow over a steady motionless model. The term "static" is a bit of a misnomer as real flows are always unsteady and models are never entirely motionless. The reality is that flows can be established that are very near steady conditions for sufficiently small Reynolds numbers. The incoming free stream flow can be 'characterized by a time-independent mean flow with a superimposed additive fluctuating contribution most often characterized by a turbulence level' [12]. The free stream flow is also non-uniform. The interaction of the flow with the model generates additional fluctuations in the flow, which in turn produces fluctuations in the loads on the model. Along with the unsteady free stream there can be any number of factors that may induce dynamic motions of an otherwise "static" model. The system is generally a combination of the free stream flow, unsteady flow induced by the model, vibrations of the support structure or the tunnel itself, aeroelastics of the model, etc. Static wind tunnel test conditions and models are at best quasi-steady and quasi-static respectively. These quasi states lead to inherent variation in the data. The "data" is often but not limited to voltages measured from a balance.

Forced oscillation tests are inherently subject to unsteady flow conditions as the models are deliberately oscillated. The tests involve measuring forces and moments on a model during sinusoidal oscillations at set frequencies and amplitudes. The frequency of oscillation is ideally constant however this not the reality nor is the oscillation purely sinusoidal. Again, the test conditions are quasi-sinusoidal.

Static and forced oscillation wind tunnel tests were conducted at the 14- by 22-Foot Subsonic Tunnel at NASA Langley Research Center (figure 3.1). The test had three objectives. First the tests were to provide the necessary data to assess the influence of blockage of two different model support structures on the aerodynamic coefficients of a fighter and a generic civil transport configuration. No corrections for blockage or any other type were made so that the impact of blockage between the two supports would be apparent. The second was to provide data necessary for simulation and modeling. Finally the test was to provide data necessary to support an uncertainty analysis of the calculated body axis aerodynamic coefficients for static and forced oscillation tests.

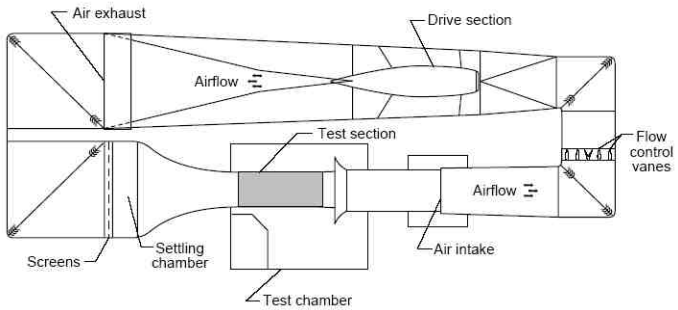

Figure 3.1 Schematic of 14- by 22-Foot Subsonic Tunnel [13].

The 14- by 22-Foot Subsonic Tunnel provided a unique ability to test with closed and open test sections. The tests consisted of measuring the forces and moments with an internal strain-gage balance and wall pressures from electronically scanned pressure (ESP) modules when the test section was closed. The uncertainty of the measurements from the ESP system is beyond the scope of this thesis and will not be quantified.

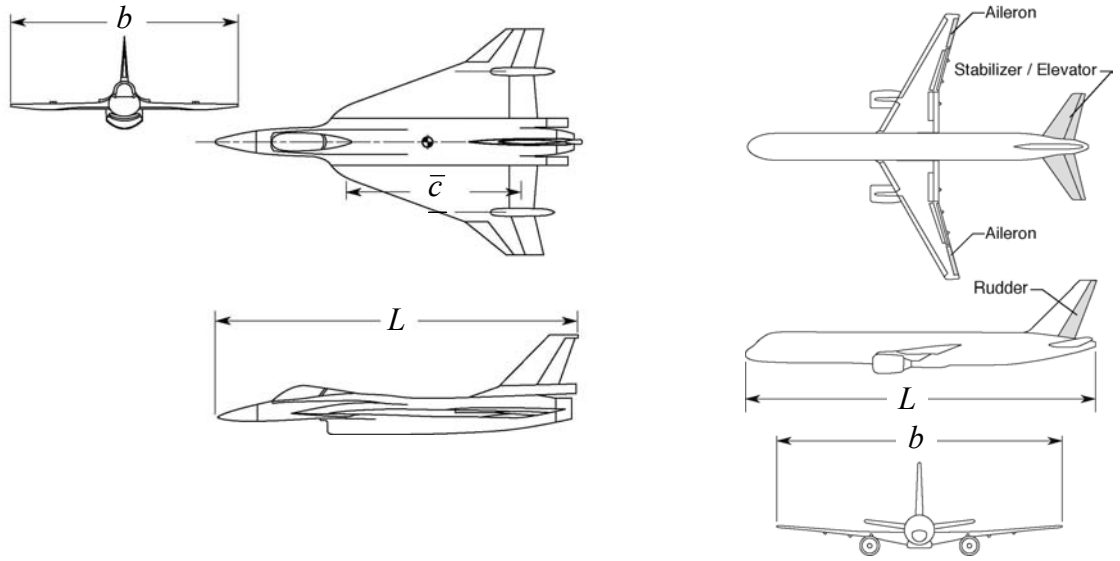

S	=	19.44	ft^2
b	=	5.83	ft
$\bar{c}$	=	4.45	ft
L	=	9.76	ft

(a)

S	=	5.90	ft^2
b	=	6.85	ft
$\bar{c}$	=	0.92	ft
L	=	8.54	ft

(b)

Figure 3.2 Schematics of (a) fighter model [3] and (b) generic civil transport model [14]. Note drawings are to scale with respect to one another.

3-2 Description of models

The models used in the test are part of current simulation and modeling studies. Each model produces a unique flow-field and brings its own inherent uncertainty. The Generic Civil Transport (GCT) has a high-aspect ratio wing of roughly 7.95. Its flow field is dramatically different than that of the highly swept wing of the fighter model, which has a vortex dominated flow field. Three-view drawings of the two models are shown in figure 3.2. The civil transport was tested at a dynamic pressure of 10 psf at a range of α's of ±90º. Few adverse model dynamics during the test were encountered. The fighter model on the other hand was planned for testing at a range of α's of ±90º and with a dynamic pressure of 6.7 psf, however model dynamics resulted in exceedance of balance limits around α = 50º. Balance limits forced the test to be run at a q of 0.95 psf to achieve the desired α schedule.

3-3 Description of model supports

The model supports used were the Forced Oscillation (FO) rig, and the Small Model Support (SMS). The Forced Oscillation rig provides the capability of static and dynamic testing, however it is primarily used for dynamic testing. Forced oscillation testing is literally forcing oscillations in the pitch, roll, or yaw axis (Click hyperlinks for videos). Figure 3.3 displays three possible mounting configurations. The models can be mounted with the sting thru the top or bottom of the model for pitch or yaw oscillations or mounted with a straight or bent sting for roll oscillations. Angle-of-attack is set by rotating the turntable with the model mounted ±90 degrees to wings level (i.e. ±90 degrees of bank). The advantages of using the FO rig primarily rest with dynamic testing. One advantage for static testing is the model orientation theoretically never changes with respect to the gravity vector, as the angle-of-attack is set. This leads to the assumption of a level turntable and a constant weight tare. The major drawback of the FO rig with respect to static testing is blockage. It has overall more projected area than the SMS. The FO support post is suspected to influence the aerodynamic performance of the model. The post also becomes a problem at large ±α's. The post blankets the model at high α's for pitch and yaw mounts thus requiring a configuration change to continue large α sweeps. The sting is a potential source of aerodynamic interference for top mounts as it may blanket the vertical tail. The FO rig can be used to generate sideslip depending on the setup. Top or bottom mounting in the yaw axis allows arbitrary selection of sideslip, the sideslip for a roll axis mount will vary with the angle-of-attack and no sideslip is possible for pitch mounts.

(a) *(b)* *(c)*

Figure 3.3 Fighter model mounted right wing up on the Forced Oscillation rig ; (a) bottom mount for pitch oscillations with a closed test section, (b) aft mount for roll oscillations with a closed test section, and (c) top mount for yaw oscillations with an open test section (Click on pictures for larger view).

The SMS (figure 3.4a) has no dynamic testing capabilities. It is the primary model support for static testing. It has the ability to arbitrarily set a constant sideslip angle from ±90º with the turntable and α's from -10º to 90º.

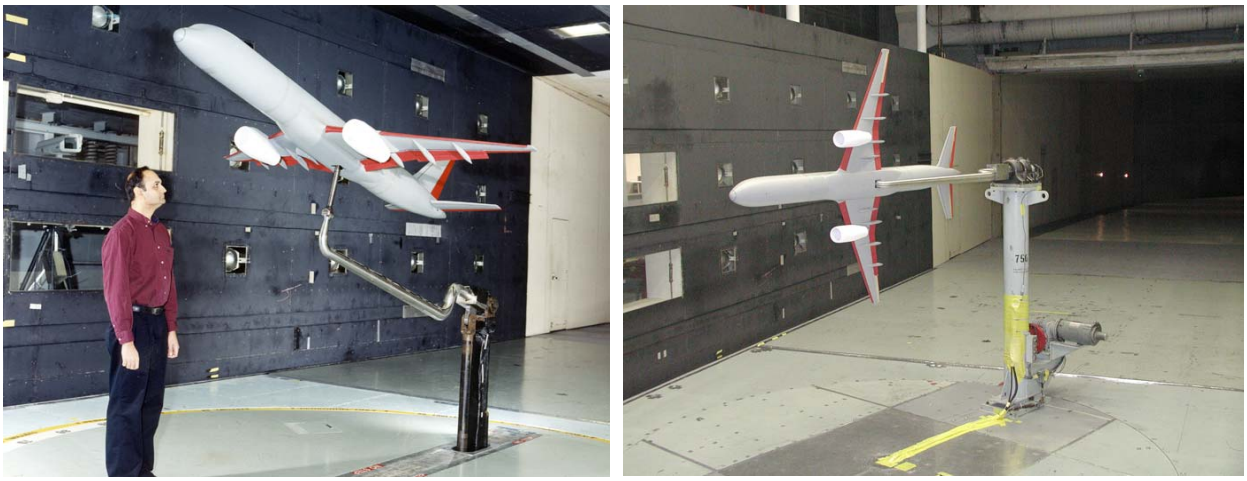

(a) *(b)*

Figure 3.4 Generic civil transport model in closed test section; (a) mounted wings level on SMS and (b) bottom mounted for roll oscillations on forced oscillation rig with "bent" sting [14].

4 Uncertainty of Instrumentation

4-1 Introduction

The uncertainty of an aerodynamic coefficient is an amalgamation of countless elemental error sources. Wind tunnel turbulence, flow angularity, vibrations, electromagnetics, installation effects, environmental effects, test technique, and even operator error all affect the quality of the coefficients in addition to instrumentation accuracies, calibration regressions, and data reduction algorithms. This report will encompass those sources quantifiable without further testing, i.e. the instrumentation accuracies, calibration regressions, and data reduction algorithms used.

4-2 General error sources and paths

Wind tunnel test procedures and instrumentation vary with facility, test engineer, and certainly with the test objectives. The data reduction procedures used to estimate aerodynamic coefficients for static and forced oscillation are conceptually similar. Balance and attitude/orientation measurements are recorded first with the wind off. These measurements are collectively called tares. They are used to subtract weights and inertial effects from the forces and moments recorded with the wind on. Tares are acquired from the data acquisition system as voltages. The data acquisition system contributes its own uncertainties to the voltages output from the balance and attitude/orientation instruments. The acquired tare is then sent to a workstation for conversion to engineering units, corrections, interpolations, and data reduction. Each one of those steps contributes error as well as round-off error from operating in the digital environment. Round-off error will be considered negligible relative to other error sources and will not be quantified, however it is important to note all computations are in a finite digital domain.

Errors from data acquisition in the tare and wind-on runs combine with errors from the balance sensitivities, interaction coefficients and model attitude/orientation sensitivities. Tares are typically recorded at attitudes/orientations with a slightly larger range but fewer set points than wind-on runs for static tests and thus tare values will be interpolated for data reduction. Forced oscillation tests are similar in that the tare must be interpolated, however this is due to sampling and will be discussed in detail in subsequent chapters. Interpolations are treated as regressions for uncertainty propagation. As such the uncertainties from tare forces and moments (ordinate) and tare attitudes/orientations (abscissa) combine with uncertainties from the wind on run attitudes/orientations to give a final uncertainty in the interpolated tare forces and moments. The uncertainty from the data acquisition system also combines with errors in the pressure transducer sensitivity and dynamic pressure correction uncertainties to yield a final uncertainty on dynamic pressure.

Figure 4.1 illustrates how error sources from tares and wind on runs combine with sensitivities of instruments (calibration regressions), interpolations and finally into the data reduction equation to produce uncertainty on the body axis aerodynamic coefficients. Blue and Green are used to represent error paths of tare measurements and wind on run measurements

respectively. Error sources are listed in rounded rectangles. Red is used to illustrate error contributions from both tare measurements and wind on run measurements.

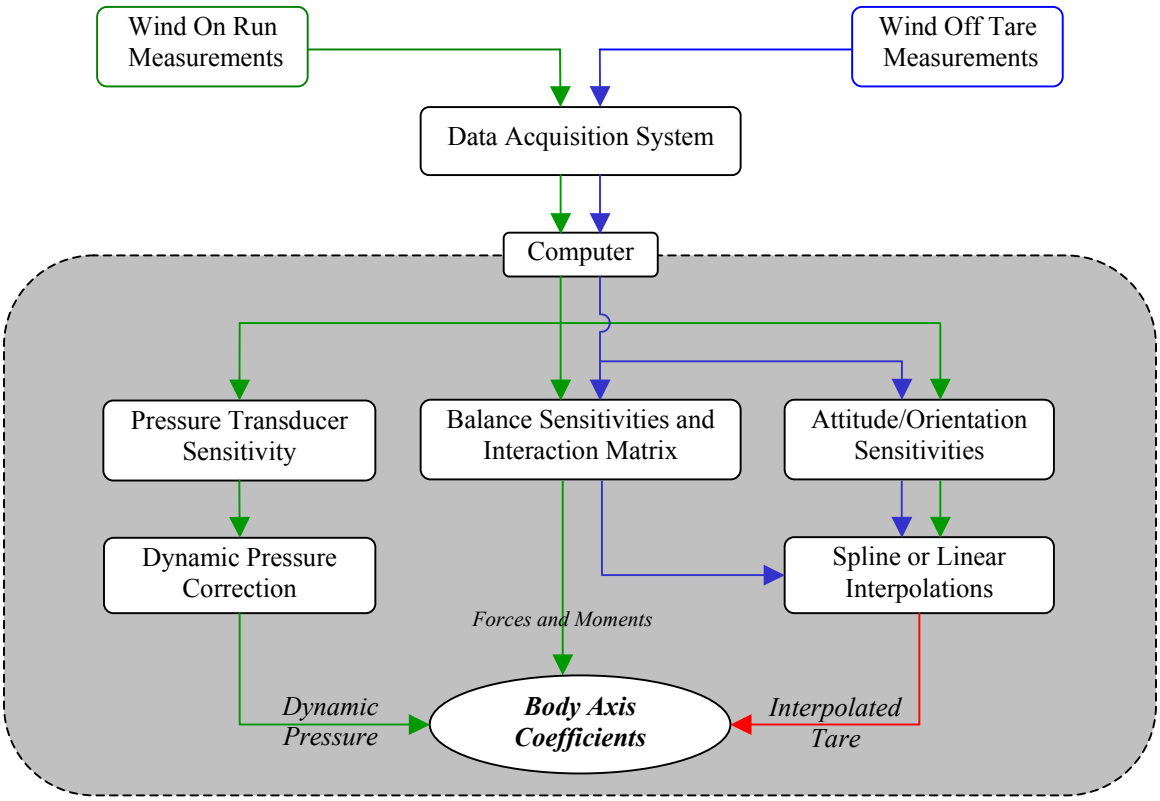

Figure 4.1 Error sources and paths from wind on run measurements and wind off tare measurements that contribute to aerodynamic coefficient uncertainties.

4-2.1 Data acquisition system

Typical wind tunnel tests use a data acquisition computer with analog-to-digital converters (ADC) and amplifiers to convert and record signals from instrumentation used in the test. For this test all balance and transducer voltages were measured and acquired with a ±10.24-V 16 bit NEFF 620 data acquisition system. The system can be set with anti-aliasing filters of 1 (or 4-Hz depending on the ADC card), 10, 100, or 1000-Hz. ADC cards can be sample-and-hold or progressive scan. Two gain settings are available for each channel. The preamp gain can be 1, 8, 64, or 512. A post amplifier can be used to provide auto-ranging over a 1-to-32 gain range in six binary steps. If auto-ranging is used, the 3 least significant bits are used to report the post amplifier gain. This results in 12 bits of resolution with 1 sign bit as apposed to 15 bits of resolution with 1 sign bit if auto ranging is not used.

NEFF provided a system error budget upon request. The uncertainty of the data acquisition system varies with the filter used, the total gain (preamp* post amp.), and the drift in temperature from calibration. The breakdown of systematic and random error estimations provided in the system error budget is listed in Table 4.1. It is assumed the estimations are made with 95% confidence and each channel is independent. Full scale range, FS is given in Volts and is defined by

$$FS = \frac{10.24}{\text{total gain}} \tag{4.1}$$

Table 4.1 NEFF data acquisition error sources and accuracies.

NEFF Error Sources & Accuracies		
Systematic Errors		
Basic Accuracy	± (0.02% FS + 2μV)	
Gain Stability	±0.002% FS / DEG. C	
Zero Stability	±1μV / DEG. C	
Random Errors		
RTO	±2.5mV / total gain	
RTI	Filter Setting (Hz)	RTI (V)
	1	±1.00E-06
	10	±1.00E-06
	100	±2.00E-06
	1000	±6.00E-06

The individual systematic and random errors are root-sum-squared such that the bias of the NEFF is

$$B_{NEFF} = \sqrt{(\text{Basic Accuracy})^2 + (\text{Gain Stability})^2 + (\text{Zero Stability})^2} \tag{4.2}$$

and the precision limit is

$$(2S_{NEFF}) = \sqrt{(\text{RTO})^2 + (\text{RTI})^2} \tag{4.3}$$

where RTO and RTI are the element of temperature coefficient Relative To Output and Relative To Input respectively [15] These uncertainties will be combined with every sample from the data acquisition system.

4-2.2 Pressure transducer accuracy

The differential pressure transducer used was a Rosemount model 1221. It had a range of 0 to 36-psf with a manufacture's specified combined non-linearity and hysteresis of ±0.12 % of full scale. This simply specifies the instrument is within ±0.043-psf of some specified linear model or sensitivity (20-volts/psid). The transducer was then calibrated to a combined non-linearity and hysteresis of ±0.024 % of full scale (±0.009-psf) with a reported sensitivity of 20.00221-volts/psid. This measure of accuracy is merely the percentage full scale of the maximum difference between the calibration data and a linear least-squares fit of the data using a linear model.

The reference standard used to apply the pressure to the transducer during calibration and the voltmeter used to read the output voltage of the transducer are listed in Table 4.2 along with their respective manufacture's listed accuracies. These accuracies are considered systematic

errors. The calibration laboratory is a well-controlled environment. Thus any random errors from the calibration are considered to be negligible.

Table 4.2 Manufacturer's reported accuracies of pressure transducer calibration instrumentation.

Rosemount Differential Pressure Transducer Calibration Instrumentation Accuracies		
CALIBRATION INSTRUMENT	**RANGE**	**MANUFACTURER'S ACCURACY**
Ruska Quartz Pressure Standard	0-100 TORR	±0.003% full scale + 0.010% reading
Fluke DVM, Model No. 8842A	0.1 μVDC -1000 VDC	±0.0035% reading + 0.0002V*

*Accuracy varies with range setting. Accuracy listed is for 20 VDC setting.

Table 4.3 Strain-gauge balance accuracies

FF10C Strain-gauge Balance Accuracies		
Component	**Full Scale (lb or in*lb)**	**Accuracy % FS (95% conf.)**
Normal	400	±0.06
Axial	200	±0.10
Pitch	2000	±0.06
Roll	1230	±0.10
Yaw	2000	±0.05
Side	200	0.08

4-2.3 Balance accuracies

The balance used in the tests was an internal strain-gauge balance, called FF10C. This balance is considered to have relatively low interactions. As a result only the linear interaction terms of the entire non-linear second order interaction model were used to reduce the wind tunnel data. The calibration laboratory provided accuracies with 95% confidence of the non-linear model (Table 4.3). Accuracies for a linear model would in all likelihood be worse. It is beyond the scope of this thesis to evaluate the accuracies of a new linear model. It will be assumed the accuracies given in table 4.3 are representative of those of a linear model. It should be noted these estimates are for the full scale condition. The actual balance accuracies are neither constant or linear over the range of the balance; however, the actual variation of the accuracy over the measurement range was not known. Therefore, variation of accuracy with measurement load was not considered.

4-2.4 Model attitude/orientation

The model attitude/orientation is measured by a variety of different instruments depending on the type of test and model support. Static tests on the SMS use an angle measurement system called a QFLEX to measure the attitude of the model. The QFLEX is mounted internal to the model. This system consists of two orthogonal accelerometers in the longitudinal plane of the model with one accelerometer parallel to the longitudinal axis.

The forced oscillation support system, which will also be discussed later, provides a single degree of freedom oscillation about one of the body axes. It uses an angular displacement transducer (ADT) to measure the angle of oscillation. The angle-of-attack is then set by the test section turntable requiring the model to be mounted such that the lateral-directional axis is in the vertical plane, or with a ±90º bank.

The accuracies from calibrations of the QFLEX and ADT are listed in table 4.4. The QFLEX accuracy is listed as two times the standard deviation of the difference between the calibration data and a linear fit. The ADT is listed as maximum nonlinearity in percent full scale, which is understood to be the maximum difference between the calibration data and a linear fit in percent full scale. The accuracy of the turntable was not available and had to be estimated from previous experience.

Table 4.4 Angular measurement system accuracies

Angular Measurement Systems		
Instrument	Range (Degrees)	Accuracy (Degrees)
QFLEX	±180	±0.005
ADT	±30	±0.016% FS
Turntable	±180	±0.1

5 Dynamic Pressure Uncertainty

5-1 Introduction

The preceding chapters discussed the necessary mathematical tools and assumptions that will be applied to estimate the uncertainty in wind tunnel aerodynamic force and moment coefficients from this point forward. The uncertainties of aerodynamic force and moment coefficients from any wind tunnel tests are functions of the uncertainties in the measured free stream dynamic pressure. An example is presented which illustrates how uncertainties from instrumentation calibration and uncertainties from wind tunnel calibration propagate through the data reduction to the final estimate of dynamic pressure. This formulation will be used to determine the aerodynamic coefficients and their uncertainties in subsequent chapters.

5-2 Pressure measurement process

The free stream dynamic pressure was determined from the difference between a static probe in the contraction cone and static atmospheric reservoir in the control room [12]. This static delta was measured by a differential pressure transducer, which output a voltage, V_q for a given pressure differential or measured dynamic pressure, q_m such that

$$q_m = m_q(V_q - V_{q_z}) \tag{5.1}$$

where V_{q_z} was the wind off voltage and m_q is the sensitivity constant from a linear least squares regression of the pressure transducer calibration data. The test section was calibrated by measuring the dynamic pressure in the test section, $q_{Cal.}$ and the pressure differential from the contraction cone and the reservoir, $q_{m_{Cal.}}$. The ratio of the two pressures, $c_{prime_{Cal.}}$ where

$$c_{prime_{Cal.}} = \frac{q_{Cal.}}{q_{m_{Cal.}}} \tag{5.2}$$

was fit with a second order least-squares regression as a function of $q_{m_{Cal.}}$. The measured dynamic pressure was then corrected to the dynamic pressure of the empty test section by a test section flow calibration factor, c_{prime} where

$$c_{prime} = a' + b' q_m + c' q_m^2 \tag{5.3}$$

Here *a'*, *b'*, and *c'* are coefficients from a second order least-squares regression of the test section flow calibration data. The corrected dynamic pressure, q is

$$q = q_m c_{prime} \tag{5.4}$$

5-3 Uncertainty in dynamic pressure

The calculated dynamic pressure is a function of four coefficients and two measured variables. Each coefficient is in turn a function of the calibration data from which it arose. The pressure transducer calibration laboratory chose a first order linear regression, such as Eq. (2.38), to model the calibration data for the Rosemount differential pressure transducer. However, as shown in Eq. (5.1), the data reduction program for the aerodynamic coefficients neglects the y-intercept. The calibration laboratory and data reduction models respectively are

$$P_p = \frac{N\sum_{i=1}^{N} V_{Cal_{\cdot i}} P_{Cal_{\cdot i}} - \sum_{i=1}^{N} V_{Cal_{\cdot i}} \sum_{i=1}^{N} P_{Cal_{\cdot i}}}{N\sum_{i=1}^{N} (V_{Cal_{\cdot i}}^2) - \left(\sum_{i=1}^{N} V_{Cal_{\cdot i}}\right)^2} (V_p) + \frac{\sum_{i=1}^{N} (V_{Cal_{\cdot i}}^2) \sum_{i=1}^{N} P_{Cal_{\cdot i}} - \sum_{i=1}^{N} V_{Cal_{\cdot i}} \sum_{i=1}^{N} (V_{Cal_{\cdot i}} P_{Cal_{\cdot i}})}{N\sum_{i=1}^{N} (V_{Cal_{\cdot i}}^2) - \left(\sum_{i=1}^{N} V_{Cal_{\cdot i}}\right)^2} \quad (5.5)$$

or

$$q_m = m_q (V_q - V_{q_z}) + b_q \quad (5.6)$$

where P_p and V_p are equivalent to q_m and $(V_q - V_{q_z})$ respectively and b_q is the y-intercept. The slope of Eq. (5.1), m_q, can be expanded as a function of the calibration constants so that

$$q_m = \frac{N\sum_{i=1}^{N} V_{Cal_{\cdot i}} P_{Cal_{\cdot i}} - \sum_{i=1}^{N} V_{Cal_{\cdot i}} \sum_{i=1}^{N} P_{Cal_{\cdot i}}}{N\sum_{i=1}^{N} (V_{Cal_{\cdot i}}^2) - \left(\sum_{i=1}^{N} V_{Cal_{\cdot i}}\right)^2} (V_q - V_{q_z}) \quad (5.7)$$

Here $V_{Cal_{\cdot i}}$ and $P_{Cal_{\cdot i}}$ are the data pairs from the differential pressure transducer calibration. The uncertainties of Eqns (5.6) and (5.7) are determined using Eq. (2.42) such that

$$\begin{aligned} U_{q_m}^2 = & \sum_{i=1}^{N} \left(\frac{\partial q_m}{\partial V_{Cal_{\cdot i}}}\right)^2 B_{V_{Cal_{\cdot i}}}^2 + 2\sum_{i=1}^{N-1} \sum_{k=i+1}^{N} \left(\frac{\partial q_m}{\partial V_{Cal_{\cdot i}}}\right)\left(\frac{\partial q_m}{\partial V_{Cal_{\cdot k}}}\right) B_{V_{Cal_{\cdot i}} V_{Cal_{\cdot k}}} + \sum_{i=1}^{N} \left(\frac{\partial q_m}{\partial V_{Cal_{\cdot i}}}\right)^2 (2S_{V_{Cal_{\cdot i}}})^2 \\ & + \sum_{i=1}^{N} \left(\frac{\partial q_m}{\partial P_{Cal_{\cdot i}}}\right)^2 B_{V_{Cal_{\cdot i}}}^2 + 2\sum_{i=1}^{N-1} \sum_{k=i+1}^{N} \left(\frac{\partial q_m}{\partial P_{Cal_{\cdot i}}}\right)\left(\frac{\partial q_m}{\partial P_{Cal_{\cdot k}}}\right) B_{P_{Cal_{\cdot i}} P_{Cal_{\cdot k}}} + \sum_{i=1}^{N} \left(\frac{\partial q_m}{\partial P_{Cal_{\cdot i}}}\right)^2 (2S_{P_{Cal_{\cdot i}}})^2 \\ & + \left(\frac{\partial q_m}{\partial V_q}\right)^2 B_{V_q}^2 + \left(\frac{\partial q_m}{\partial V_{q_z}}\right)^2 B_{V_{q_z}}^2 + 2\left(\frac{\partial q_m}{\partial V_q}\right)\left(\frac{\partial q_m}{\partial V_{q_z}}\right) B_{V_q V_{q_z}} \\ & + \left(\frac{\partial q_m}{\partial V_q}\right)^2 (2S_{V_q})^2 + \left(\frac{\partial q_m}{\partial V_{q_z}}\right)^2 (2S_{V_{q_z}})^2 \end{aligned} \quad (5.8)$$

The biases of variables from the same instrument were considered perfectly correlated. For example the covariance of two applied pressures from the calibration is

$$B_{P_{Cal_{\cdot i}} P_{Cal_{\cdot k}}} = (0.01\%\ P_{Cal_{\cdot i}} + 0.003\%\ P_{\mathrm{FS}}) * (0.01\%\ P_{Cal_{\cdot k}} + 0.003\%\ P_{\mathrm{FS}}) \tag{5.9}$$

where P_{FS} is full scale of the pressure standard, 100 Torr or 1.934 psi and $P_{Cal_{\cdot i}}$ and $P_{Cal_{\cdot k}}$ are individual pressure readings from the calibration. Figure 5.1 shows how the uncertainties from Eqs. (5.5) and (5.7) compare with the accuracy quoted on the calibration report, ±0.024 % FS.

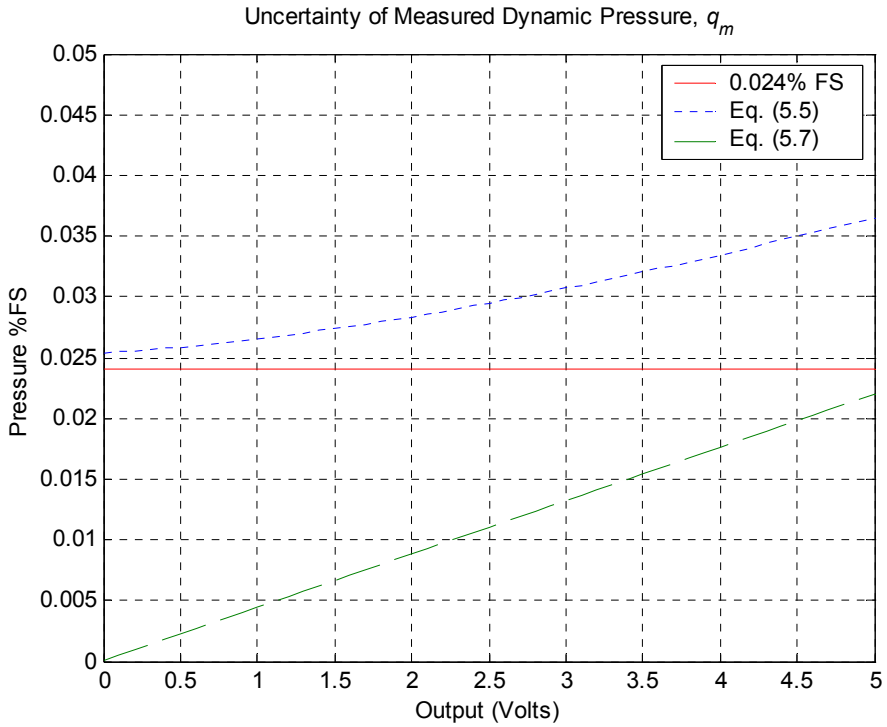

Figure 5.1 Uncertainties from different models of the measured dynamic pressure compared to quoted accuracy on calibration report.

Figure 5.1 is an excellent example of how the uncertainty of a regression varies with the independent variables and especially how dramatically the uncertainty curve can change from model to model. All three first order linear models for the measured dynamic pressure could very well be considered acceptable, as each of them provides a good approximation of the sensitivity. However, their uncertainties are quite different. One way to validate the actual uncertainty variation over the range of the transducer is to repeat the calibration multiple times with small step sizes between set points.

A regression of the uncertainty associated with the calibration data in Eq. (5.7) is necessary to avoid carrying tables of the calibration data around for new values of V. Following Eq. (2.44)

$$U_{q_m}^2 = U_{q_m - regress}^2 + m_q^2 \left(B_{V_q}^2 + B_{V_{q_z}}^2 - 2B_{V_q V_{q_z}} + (2S_{V_q})^2 + (2S_{V_{q_z}})^2 \right) \tag{5.10}$$

where

$$U_{q_m-regress} = 1.59\text{x}\,10^{-6}(V_q - V_{q_z}) \tag{5.11}$$

The next step in the dynamic pressure measurement process is to apply the test section flow calibration correction or the dynamic pressure correction, c_{prime}. Recall from Eqns. (5.2) and (5.3), c_{prime} is a function of the test section flow calibration data and the measured dynamic pressure from the wind tunnel test. Different instruments were used to record $q_{Cal.}$, $q_{m_{Cal.}}$ and q_m. Thus, no correlated bias exists between them except for installation effects between $q_{m_{Cal.}}$ and q_m from the static probe in the contraction cone and common pressure lines, neither of which will be quantified.

The systematic error associated with $c_{prime_{Cal.}}$ is

$$B^2_{C_{prime_{Cal.}}} = \left(\frac{\partial c_{prime_{Cal.}}}{\partial q_{Cal.}}\right)^2 B^2_{q_{Cal.}} + \left(\frac{\partial c_{prime_{Cal.}}}{\partial q_{m_{Cal.}}}\right)^2 B^2_{q_{m_{Cal.}}} = \left(\frac{1}{q_{m_{Cal.}}}\right)^2 B^2_{q_{Cal.}} + \left(-\frac{c_{prime_{Cal.}}}{q_{m_{Cal.}}}\right)^2 B^2_{q_{m_{Cal.}}} \tag{5.12}$$

Each transducer that recorded $q_{m_{Cal.}}$ and q_{Cal} had a manufacturer's accuracy of 0.01% FS with a full scale range of 1.0 psi. Neglecting installation effects the biases of $q_{m_{Cal.}}$ and q_{Cal} are equal such that $B_{q_{mCal.}} = B_{q_{Cal.}}$ but are not correlated. Clearly the biases between individual measurements of $q_{m_{Cal.}}$ and between individual measurements of q_{Cal} are correlated. How should these correlations be accounted for with $c_{prime_{Cal.}}$ in the regression of the test section flow calibration data? Recall $c_{prime_{Cal.}} = f(q_{cal.}, q_{m_{Cal.}})$. The covariance approximation $B_{c_{primeCal.i}\,c_{primeCal.k}}$ is given by

$$\begin{aligned} B_{c_{primeCal.i}\,c_{primeCal.k}} &= \left(\frac{\partial c_{prime_{Cal.i}}}{\partial q_{Cal._i}}\right)\left(\frac{\partial c_{prime_{Cal.k}}}{\partial q_{Cal._k}}\right) B_{q_{Cal.i}\,q_{Cal.k}} + \left(\frac{\partial c_{prime_{Cal.i}}}{\partial q_{m_{Cal.i}}}\right)\left(\frac{\partial c_{prime_{Cal.k}}}{\partial q_{m_{Cal.k}}}\right) B_{q_{mCal.i}\,q_{mCal.k}} \\ &= \left(\frac{1}{q_{m_{Cal_i.}}}\right)\left(\frac{1}{q_{m_{Cal_k.}}}\right) B_{q_{Cal.i}} B_{q_{Cal.k}} + \left(-\frac{c_{prime_{Cal.i}}}{q_{m_{Cal.i}}}\right)\left(-\frac{c_{prime_{Cal.k}}}{q_{m_{Cal.k}}}\right) B_{q_{mCal.i}} B_{q_{mCal.k}} \\ &= \frac{1 + c_{prime_{Cal.i}}\, c_{prime_{Cal.k}}}{q_{m_{Cal.i}}\, q_{m_{Cal.k}}} B^2_{q_{Cal.}} \end{aligned} \tag{5.13}$$

Multiple q-sweeps, all at the same measured dynamic pressures, were made during the test section flow calibration. Equation (2.12) will be used to estimate the random uncertainty of each of the 18 individual $c_{prime_{Cal.i}}$ with a confidence of 95%. The random uncertainty of each $q_{m_{Cal.k}}$ measurement will be considered negligible until better estimates are available. The total uncertainty of c_{prime} can now be determined following Eq. (2.42) such that

$$
\begin{aligned}
U_{c_{prime}}^2 = & \sum_{i=1}^{N}\left(\frac{\partial c_{prime}}{\partial V_{Cal\cdot i}}\right)^2 B_{V_{Cal\cdot i}}^2 + 2\sum_{i=1}^{N-1}\sum_{k=i+1}^{N}\left(\frac{\partial c_{prime}}{\partial V_{Cal\cdot i}}\right)\left(\frac{\partial c_{prime}}{\partial V_{Cal\cdot k}}\right)B_{V_{Cal\cdot i}V_{Cal\cdot k}} \\
& + \sum_{i=1}^{N}\left(\frac{\partial c_{prime}}{\partial P_{Cal\cdot i}}\right)^2 B_{V_{Cal\cdot i}}^2 + 2\sum_{i=1}^{N-1}\sum_{k=i+1}^{N}\left(\frac{\partial c_{prime}}{\partial P_{Cal\cdot i}}\right)\left(\frac{\partial c_{prime}}{\partial P_{Cal\cdot k}}\right)B_{P_{Cal\cdot i}P_{Cal\cdot k}} \\
& + \sum_{i=1}^{N}\left(\frac{\partial c_{prime}}{\partial V_{Cal\cdot i}}\right)^2 (2S_{V_{Cal\cdot i}})^2 + \sum_{i=1}^{N}\left(\frac{\partial c_{prime}}{\partial P_{Cal\cdot i}}\right)^2 (2S_{P_{Cal\cdot i}})^2 \\
& \sum_{i=1}^{N}\left(\frac{\partial c_{prime}}{\partial c_{prime_{Cal\cdot i}}}\right)^2 B_{c_{prime_{Cal\cdot i}}}^2 + 2\sum_{i=1}^{N-1}\sum_{k=i+1}^{N}\left(\frac{\partial c_{prime}}{\partial c_{prime_{Cal\cdot i}}}\right)\left(\frac{\partial c_{prime}}{\partial c_{prime_{Cal\cdot k}}}\right)B_{c_{prime_{Cal\cdot i}}c_{prime_{Cal\cdot k}}} \\
& + \sum_{i=1}^{N}\left(\frac{\partial c_{prime}}{\partial q_{m_{Cal\cdot i}}}\right)^2 B_{q_{m_{Cal\cdot i}}}^2 + 2\sum_{i=1}^{N-1}\sum_{k=i+1}^{N}\left(\frac{\partial c_{prime}}{\partial q_{m_{Cal\cdot i}}}\right)\left(\frac{\partial c_{prime}}{\partial q_{m_{Cal\cdot k}}}\right)B_{q_{m_{Cal\cdot i}}q_{m_{Cal\cdot k}}} \\
& + \sum_{i=1}^{N}\left(\frac{\partial c_{prime}}{\partial c_{prime_{Cal\cdot i}}}\right)^2 (2S_{c_{prime_{Cal\cdot i}}})^2 + \sum_{i=1}^{N}\left(\frac{\partial c_{prime}}{\partial q_{m_{Cal\cdot i}}}\right)^2 (2S_{q_{m_{Cal\cdot i}}})^2 \\
& + \left(\frac{\partial c_{prime}}{\partial V_q}\right)^2 B_{V_q}^2 + \left(\frac{\partial c_{prime}}{\partial V_{q_z}}\right)^2 B_{V_{q_z}}^2 + 2\left(\frac{\partial c_{prime}}{\partial V_q}\right)\left(\frac{\partial c_{prime}}{\partial V_{q_z}}\right)B_{V_qV_{q_z}} \\
& + \left(\frac{\partial c_{prime}}{\partial V_q}\right)^2 (2S_{V_q})^2 + \left(\frac{\partial c_{prime}}{\partial V_{q_z}}\right)^2 (2S_{V_{q_z}})^2
\end{aligned}
\tag{5.14}
$$

Equation (5.14) simplifies to the form given by Eq. (2.44) as the only unknowns prior to the test are V_q and V_{q_z}. The total uncertainty for c_{prime} is thus

$$
\begin{aligned}
U_{c_{prime}}^2 &= U_{c_{prime}-regress}^2 + \left(\frac{\partial c_{prime}}{\partial q_m}\right)^2 U_{q_m}^2 \\
&= U_{c_{prime}-regress}^2 + (b'+2c'q_m)^2 U_{q_m}^2
\end{aligned}
\tag{5.15}
$$

where $U_{c_{prime}-regress} = f(V_q, V_{q_z})$ is a curve fit of the uncertainty from the coefficients, *a*, *b* and *c* in c_{prime}. A 5th order fit was chosen such that

$$
\begin{aligned}
U_{c_{prime}-regress} = & 1.82x10^{-8}q_m^5 - 1.55x10^{-6}q_m^4 + 4.39x10^{-5}q_m^3 \\
& - 4.01x10^{-4}q_m^2 - 1.19x10^{-3}q_m + 2.66x10^{-2}
\end{aligned}
\tag{5.16}
$$

Figure 5.2 shows the ($q_{m_{Cal.}}$, $c_{prime_{Cal.}}$) data pairs recorded in the calibration in black dots. Red dots show the ($q_{m_{Cal.}}$, $c_{prime_{Cal.}}$) data pairs rejected by Chauvenet's criterion and consequently

not used. The solid blue line is the mean of $c_{prime_{Cal.}}(q_{m_{Cal.}})$. The solid black line is Eq. (5.2) with its uncertainty, $U_{c_{prime}}$ in dashed black lines. The blue error bars are the typical two times the standard deviation, or $2S_x$ (commonly mistaken as 2σ).

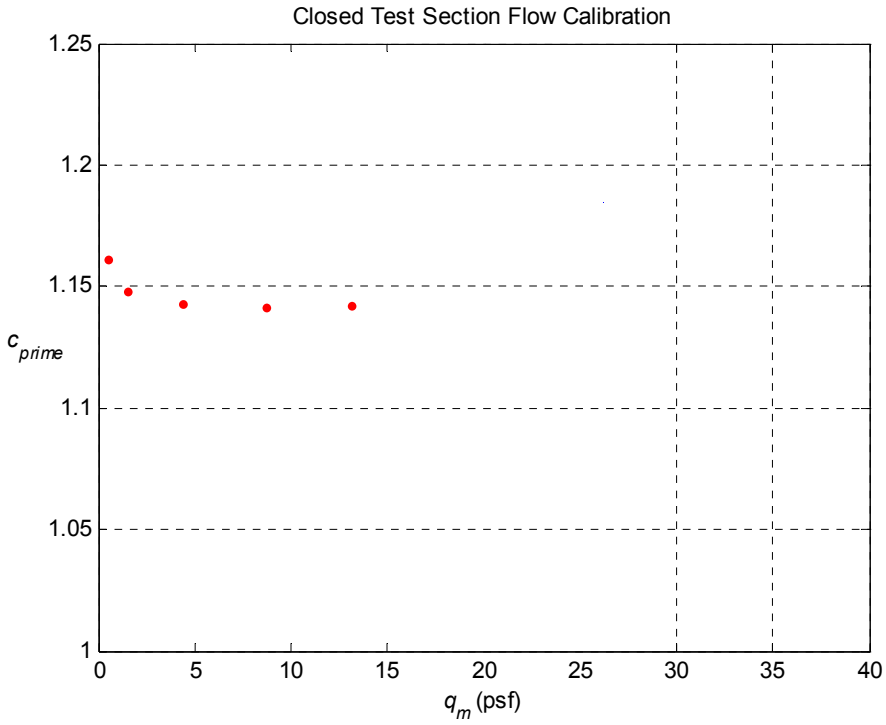

Figure 5.2 Closed test section flow calibration data with calibration uncertainty curves. Note the difference between the typical $2S_x$ error bars and the uncertainty.

The total uncertainty in the dynamic pressure is determined in the same manner as Eq. (5.14). After working through the algebra

$$U_q^2 = q_m^2 U_{c_{prime}-regress}^2 + (a'+2b'q_m + 3c'q_m^2)^2 U_{q_m}^2 \tag{5.17}$$

The uncertainty curves in figure 5.2 deserve some discussion. Recall the propagation of uncertainty equations assumes a first order Taylor series expansion of the variance about the nominal conditions is sufficient to approximate the variance. This results in the root-sum-square of the gradients of the function with respect to the independent variables times the variance of the independent variables. A parametric study was done on the second-order regression of the test section flow calibration data. Figure 5.3a is a locus of the gradients with respect to the calibration data as they vary with the new q_m. Assuming no correlations and the uncertainty of each data point is equal to unity; figure 5.3b shows how the summation of the squared gradients results in the shapes of the uncertainty of c_{prime} in figure 5.2. Note the uncertainty for each calibration data point is in reality not equal. The uncertainties, which are large at low q and small at high q, are then scaled by the gradients in figure 5.3a. This is why the uncertainty curve in figure 5.3b is slightly different than the uncertainty of c_{prime} in figure 5.2. The odd shapes of the uncertainty cures are due to the root-sum-square of the gradients of the higher-order regression.

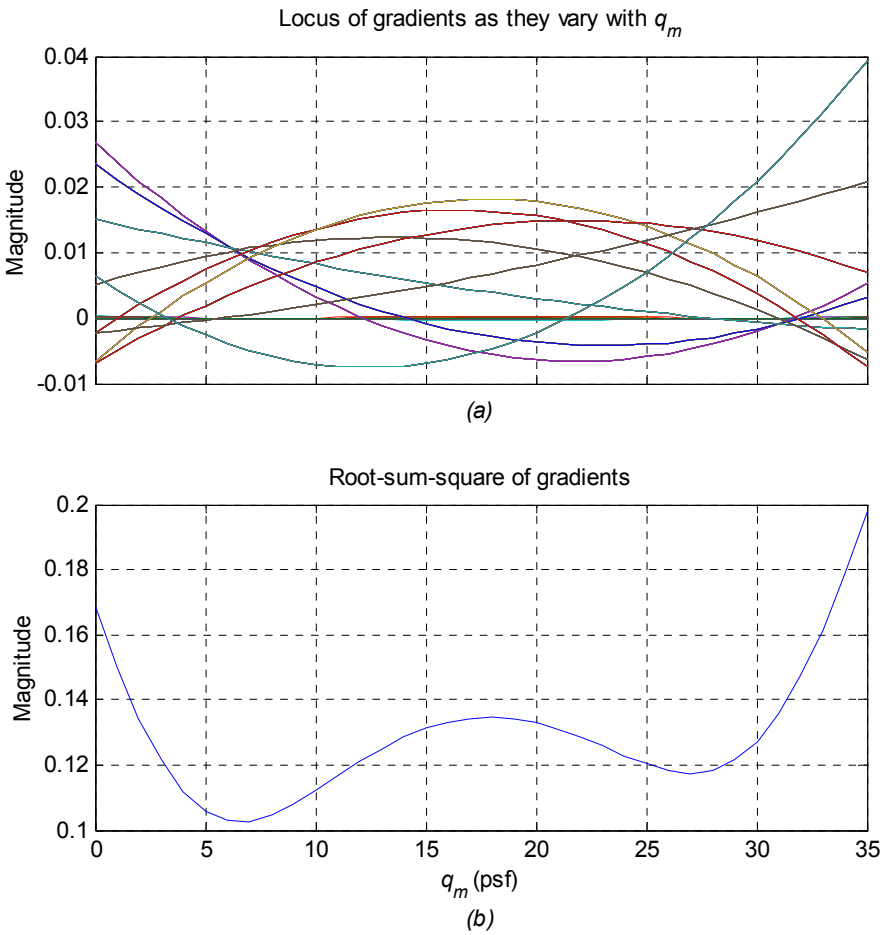

Figure 5.3 Influence of gradients on uncertainty curve. (a) Locus of gradients of c_{prime} with respect to individual measurements, $q_{m_{Cal.}}$ and $c_{prime_{Cal.}}$ as they vary with q_m. (b) Root-sum-square of gradients assuming no correlations and all uncertainties are equal to unity.

6 Uncertainty of Static Tests

6-1 Introduction

Model forces and moments are determined from measuring the voltages of a six-component internal strain-gauge balance with the wind on, which is called a "run", and with the wind off, called a "tare". The tare in a static test is a weight tare, meaning it is the loads of the balance due to the gravitational force. Usually, but not necessarily, the tare is taken before the run. Then the tare is subtracted from the run to yield the aerodynamic forces and moments.

6-2 Static force and moment measurement process

The first step in the data reduction process is to subtract the zero-load balance readings or just "zeros", voltages of the balance acquired before a run or tare is executed. These zeros, denoted with z subscripts are then subtracted from subsequent balance measurements for that run or tare to remove any voltage changes not associated with the test. The zeros for runs and tares are always taken at the same model position.

The next step is to convert the voltages to engineering units. This is done with sensitivity constants provided by the balance calibration laboratory. All balance sensitivities and interactions, which will be discussed later, are functions of the excitation voltage. The balance calibration was conducted with an excitation voltage, V = 5.000 Volts. The excitation voltage of the balance during testing however varies from 5 Volts by as much as ±0.003 Volts. The excitation voltage, V_I where the subscript I is R for run or T for tare, is measured during testing with the data acquisition system and then used to correct the measured balance voltages by applying the ratio of V_R/V or V_T/V to the balance measurements. This approach introduces only the uncertainty of the data acquisition system on V_R and V_T. The uncertainty of the excitation voltage during calibration, V will be considered negligible as the calibration laboratory is assumed a well-controlled environment. The normal force of the balance for a run is thus

$$N_{R_U} = \frac{k_N}{V}\left(V_{N_R}\frac{V_R}{V} - V_{N_{R_z}}\frac{V_{R_z}}{V}\right) = \frac{k_N}{V^2}\left(V_{N_R}V_R - V_{N_{R_z}}V_{R_z}\right) \tag{6.1}$$

where k_N is the normal force sensitivity constant in units of lbf/(mV/V) or in-lbf/(mV/V). V_{N_R} and $V_{N_{R_z}}$ are the measured voltages of the run and zero values, respectively, of the balance normal force channel. The subscript U indicates uncorrected or measured which indicates no interactions have been removed. Let k be a vector of sensitivity constants, V_{F_I} be a vector of balance voltages, and X_I be a vector of forces and moments such that

$$k = \begin{bmatrix} k_N & k_A & k_m & k_l & k_n & k_Y \end{bmatrix}^T \tag{6.2}$$

$$V_{F_I} = \begin{bmatrix} V_{N_I} & V_{A_I} & V_{m_I} & V_{l_I} & V_{n_I} & V_{Y_I} \end{bmatrix}^T \tag{6.3}$$

$$X_I = \begin{bmatrix} N_I & A_I & m_I & l_I & n_I & Y_I \end{bmatrix}^T \tag{6.4}$$

The general form of Eq. (6.1) is then

$$X_{I_{U_i}} = \frac{k_i}{V^2}\left(V_{X_{I_i}} V_I - V_{X_{I_{z_i}}} V_{I_z}\right) \tag{6.5}$$

where

$$i = 1,2,...,6$$

The subscript *i* indicates the force or moment considered. The forces and moments measured from the balance have contributions of the other forces and moments due to inherent balance interactions. Considering only the linear interactions the measured normal force, for example, would be

$$N_{T_U} = c_{1,1}N_T + c_{1,2}A_T + c_{1,3}m_T + c_{14}l_T + c_{1,5}n_T + c_{1,6}Y_T \tag{6.6}$$

where $c_{1,1}$, $c_{1,2}$, etc. are the linear interaction coefficients from the balance interaction matrix, C such that

$$C = \begin{bmatrix} c_{1,1} & c_{1,2} & \cdots & c_{1,6} \\ c_{2,1} & c_{2,2} & & \vdots \\ \vdots & & \ddots & \vdots \\ c_{6,1} & \cdots & \cdots & c_{6,6} \end{bmatrix} \tag{6.7}$$

The corrected forces and moments are then computed from the measured forces and moments with the linear interactions removed. For example, the corrected tare normal force is

$$N_T = \left(N_{T_U} - \left(c_{1,2}A_T + c_{1,3}m_T + c_{14}l_T + c_{1,5}n_T + c_{1,6}Y_T\right)\right)/c_{1,1} \tag{6.8}$$

In general the uncorrected balance loads are

$$X_{I_U} = CX_I \tag{6.9}$$

Solving for X_I yields

$$X_I = C^{-1}X_{I_U} \tag{6.10}$$

Equation (6.10) is the generic form for forces and moments from either a run or a tare. As discussed in Ch. 4, for various reasons tares are not always recorded at the same orientation as every set point in a run. Thus tare values must be interpolated. The data reduction program

currently uses a cubic spline to interpolate tare values, $X_{T_{\text{int}}}$. The aerodynamic loads, X are then found by subtracting the interpolated tare forces and moments from the run forces and moments such that

$$X_i = X_{R_i} - X_{T_{\text{int}_{i,h}}} \tag{6.11}$$

Here

$$X_{T_{\text{int}_{i,h}}} = s_{0_{i,h}} + s_{1_{i,h}}\alpha_R + s_{2_{i,h}}\alpha_R^2 + s_{3_{i,h}}\alpha_R^3 \tag{6.12}$$

where $s_{0_{i,h}}, s_{1_{i,h}}, s_{2_{i,h}}$ and $s_{3_{i,h}}$ are the coefficients of the cubic spline for the h^{th} interval of the i^{th} component. The aerodynamic coefficients, C_X are then calculated as

$$C_{X_i} = \frac{X_i}{qK_i} \tag{6.13}$$

where

$$K = \begin{bmatrix} S & S & S\bar{c} & Sb & Sb & S \end{bmatrix}^T \tag{6.14}$$

6-3 Uncertainty of static aerodynamic coefficients

The combined systematic uncertainties of the balance sensitivities and the balance interactions are provided in table 4.3. As discussed in Ch. 4 these uncertainties are for a non-linear interaction model and are given at the calibration full scale condition. They are assumed to be representative of the accuracies for a linear model.

The uncertainty of the measured balance loads using the uncertainty propagation equations results in

$$\begin{aligned} U_{X_{I_{U_i}}}^2 = U_{k_i-regress}^2 &+ \frac{k_i^2}{V^4}\left[V_I^2\left(B_{V_{F_{I_i}}}^2 + (2S_{V_{F_{I_i}}})^2\right) + V_{I_z}^2\left(B_{V_{F_{I_{z_i}}}}^2 + (2S_{V_{F_{I_{z_i}}}})^2\right)\right] \\ &+ \frac{k_i^2}{V^4}\left[V_{F_{I_i}}^2\left(B_{V_I}^2 + (2S_{V_I})^2\right) + V_{F_{I_{z_i}}}^2\left(B_{V_{I_z}}^2 + (2S_{V_{I_z}})^2\right)\right] \\ &- 2\frac{k_i^2}{V^4}\left[V_I V_{I_z} B_{V_{F_{I_i}} V_{F_{I_{z_i}}}} + V_{F_{I_i}} V_{F_{I_{z_i}}} B_{V_I V_{I_z}}\right] \end{aligned} \tag{6.15}$$

where $U_{k_i-regress}$ is the uncertainty from the balance calibration data that remains in the sensitivity constant. Let $M = C^{-1}$ where $M = [m_{i,j}]$ and let κ be a diagonal matrix of k such that

$$\kappa = \begin{bmatrix} k_N & 0 & \cdots & \cdots & \cdots & 0 \\ 0 & k_A & \ddots & & & \vdots \\ \vdots & \ddots & k_m & \ddots & & \vdots \\ \vdots & & \ddots & k_l & \ddots & \vdots \\ \vdots & & & \ddots & k_n & 0 \\ 0 & \cdots & \cdots & \cdots & 0 & k_Y \end{bmatrix} \tag{6.16}$$

The uncertainty of the corrected forces and moments follows as

$$\begin{aligned} U_{X_{I_i}}^2 &= B_{[X_{I_i}]}^2 \\ &+ \left(\frac{[m_{i,1\ldots6}]\kappa V_{F_I}}{V^2} \right)^2 \left(B_{V_I}^2 + (2S_{V_I})^2 \right) + \left(\frac{[m_{i,1\ldots6}]\kappa V_{F_{I_z}}}{V^2} \right)^2 \left(B_{V_{I_z}}^2 + (2S_{V_{I_z}})^2 \right) \\ &+ \frac{V_I^2}{V^4} \sum_{j=1}^{6} \left(m_{i,j} k_j \right)^2 \left(B_{V_{F_{I_j}}}^2 + (2S_{V_{F_{I_j}}})^2 \right) + \frac{V_{I_z}^2}{V^4} \sum_{j=1}^{6} \left(m_{i,j} k_j \right)^2 \left(B_{V_{F_{I_{z_j}}}}^2 + (2S_{V_{F_{I_{z_j}}}})^2 \right) \\ &- \frac{2}{V^4} \left([m_{i,1\ldots6}]\kappa V_{F_I} \right) \left([m_{i,1\ldots6}]\kappa V_{F_{I_z}} \right) B_{V_I V_{I_z}} - 2 \frac{V_I V_{I_z}}{V^4} \sum_{j=1}^{6} \left(m_{i,j} k_j \right)^2 B_{V_{F_{I_j}} V_{F_{I_{z_j}}}} \end{aligned} \tag{6.17}$$

where $B_{[X_{I_i}]}$ is the combined uncertainty from $m_{i,j}$ and k_i, the sensitivity coefficients and the balance interaction coefficients, respectively for the i^{th} balance component. The balance accuracies provided in table 4.3 will be used to estimate $B_{[X_{I_i}]}$.

The cubic spline interpolation, with N data pairs, can be expressed in functional form as

$$X_{T_{\text{int}_{i,h}}} = f\left([m_{i,1\ldots6}], k, V, [V_T], V_{T_z}, [V_{F_T}], V_{F_{T_z}}, \alpha_T, \alpha_R \right) \tag{6.18}$$

where $[V_T]$ and α_T are 1 x N vectors and $[V_{F_T}]$ is a 6 x N matrix. The uncertainty of the interpolated tare, $X_{T_{\text{int}_{i,h}}}$ is then expressed in Eq. (6.19). The first two terms in Eq. (6.19) are necessary to propagate the estimates of uncertainties associated with the balance interactions and sensitivities. The partial derivatives are taken with respect to $[X_{T_{i,j}}]$ because the estimates in table 4.3 are the uncertainties of the corrected components. $[X_T]$ is the 6 x N matrix of tare loads used to generate the spline coefficients. The third through sixth terms propagate the uncertainty of the excitation voltages for each set point in the tare and the tare zeros. Terms seven through ten propagate the uncertainty of the voltages from the balance channels and the respective zeros. The last four terms account for the uncertainty of the orientation during the tare and the orientation the interpolation is evaluated at, α_R.

$$
\begin{aligned}
U^2_{X_{T_{\mathrm{int}_{i,h}}}} &= \sum_{j=1}^{N}\left(\frac{\partial X_{T_{\mathrm{int}_{i,h}}}}{\partial[X_{T_{i,j}}]}\right)^2 B^2_{[X_{T_{i,j}}]} + 2\sum_{j=1}^{N-1}\sum_{k=j+1}^{N}\frac{\partial X_{T_{\mathrm{int}_{i,h}}}}{\partial[X_{T_{i,j}}]}\frac{\partial X_{T_{\mathrm{int}_{i,h}}}}{\partial[X_{T_{i,k}}]}B_{[X_{T_{i,j}}][X_{T_{i,k}}]} \\
&+ \sum_{j=1}^{N}\left(\frac{\partial X_{T_{\mathrm{int}_{i,h}}}}{\partial[V_{T_j}]}\right)^2\left(B^2_{[V_{T_j}]} + (2S_{[V_{T_j}]})^2\right) + \left(\frac{\partial X_{T_{\mathrm{int}_{i,h}}}}{\partial V_{T_z}}\right)^2\left(B^2_{V_{T_z}} + (2S_{V_{T_z}})^2\right) \\
&+ 2\sum_{j=1}^{N-1}\sum_{k=j+1}^{N}\frac{\partial X_{T_{\mathrm{int}_{i,h}}}}{\partial[V_{T_j}]}\frac{\partial X_{T_{\mathrm{int}_{i,h}}}}{\partial[V_{T_k}]}B_{[V_{T_j}][V_{T_k}]} + 2\sum_{j=1}^{N}\frac{\partial X_{T_{\mathrm{int}_{i,h}}}}{\partial[V_{T_j}]}\frac{\partial X_{T_{\mathrm{int}_{i,h}}}}{\partial V_{T_z}}B_{[V_{T_j}]V_{T_z}} \\
&+ \sum_{j=1}^{6}\sum_{k=1}^{N}\left(\frac{\partial X_{T_{\mathrm{int}_{i,h}}}}{\partial[V_{F_{T_{j,k}}}]}\right)^2\left(B^2_{[V_{F_{T_{j,k}}}]} + (2S_{[V_{F_{T_{j,k}}}]})^2\right) + \sum_{j=1}^{6}\left(\frac{\partial X_{T_{\mathrm{int}_{i,h}}}}{\partial V_{F_{T_{z_j}}}}\right)^2\left(B^2_{V_{F_{T_{z_j}}}} + (2S_{V_{F_{T_{z_j}}}})^2\right) \\
&+ 2\sum_{j=1}^{6}\sum_{k=1}^{N-1}\sum_{m=k+1}^{N}\frac{\partial X_{T_{\mathrm{int}_{i,h}}}}{\partial[V_{F_{T_{j,k}}}]}\frac{\partial X_{T_{\mathrm{int}_{i,h}}}}{\partial[V_{F_{T_{j,m}}}]}B_{[V_{F_{T_{j,k}}}][V_{F_{T_{j,m}}}]} + 2\sum_{j=1}^{6}\sum_{k=1}^{N}\frac{\partial X_{T_{\mathrm{int}_{i,h}}}}{\partial[V_{F_{T_{j,k}}}]}\frac{\partial X_{T_{\mathrm{int}_{i,h}}}}{\partial V_{F_{T_{z_j}}}}B_{[V_{F_{T_{j,k}}}]V_{F_{T_{z_j}}}} \\
&+ \sum_{j=1}^{N}\left(\frac{\partial X_{T_{\mathrm{int}_{i,h}}}}{\partial\alpha_{T_j}}\right)^2\left(B^2_{\alpha_{T_j}} + (2S_{\alpha_{T_j}})^2\right) + 2\sum_{j=1}^{N-1}\sum_{k=j+1}^{N}\frac{\partial X_{T_{\mathrm{int}_{i,h}}}}{\partial\alpha_{T_j}}\frac{\partial X_{T_{\mathrm{int}_{i,h}}}}{\partial\alpha_{T_k}}B_{\alpha_{T_j}\alpha_{T_k}} \\
&+ \left(\frac{\partial X_{T_{\mathrm{int}_{i,h}}}}{\partial\alpha_R}\right)^2\left(B^2_{\alpha_R} + (2S_{\alpha_R})^2\right) + 2\frac{\partial X_{T_{\mathrm{int}_{i,h}}}}{\partial\alpha_R}\sum_{j=1}^{N}\frac{\partial X_{T_{\mathrm{int}_{i,h}}}}{\partial\alpha_{T_j}}B_{\alpha_R\alpha_{T_j}}
\end{aligned}
\tag{6.19}
$$

The uncertainty in the aerodynamic loads can simply be expressed as

$$
U^2_{X_i} = U^2_{X_{R_i}} + U^2_{X_{T_{\mathrm{int}_{i,h}}}} - 2B_{X_{R_i}X_{T_{\mathrm{int}_{i,h}}}} \tag{6.20}
$$

Here the correlated bias, $B_{X_{I_i}X_{T_{\mathrm{int}_{i,h}}}}$ between the run and interpolated tare is

$$
\begin{aligned}
B_{X_{R_i}X_{T_{\mathrm{int}_{i,h}}}} &= \sum_{j=1}^{N}\left(\frac{\partial X_{T_{\mathrm{int}_{i,h}}}}{\partial[X_{T_{i,j}}]}\right)B_{[X_{R_i}][X_{T_{i,j}}]} \\
&+\left(\frac{[m_{i,1\ldots6}]\kappa V_{F_R}}{V^2}\right)\sum_{j=1}^{N}\left(\frac{\partial X_{T_{\mathrm{int}_{i,h}}}}{\partial[V_{T_j}]}\right)B_{V_R[V_{T_j}]}+\left(\frac{[m_{i,1\ldots6}]\kappa V_{F_R}}{V^2}\right)\left(\frac{\partial X_{T_{\mathrm{int}_{i,h}}}}{\partial V_{T_z}}\right)B_{V_R V_{T_z}} \\
&-\left(\frac{[m_{i,1\ldots6}]\kappa V_{F_{R_z}}}{V^2}\right)\sum_{j=1}^{N}\left(\frac{\partial X_{T_{\mathrm{int}_{i,h}}}}{\partial[V_{T_j}]}\right)B_{V_{R_z}[V_{T_j}]}-\left(\frac{[m_{i,1\ldots6}]\kappa V_{F_{R_z}}}{V^2}\right)\left(\frac{\partial X_{T_{\mathrm{int}_{i,h}}}}{\partial V_{T_z}}\right)B_{V_{R_z}V_{T_z}} \\
&+\frac{V_R}{V^2}\sum_{j=1}^{6}\sum_{k=1}^{N}(m_{i,j}k_j)\left(\frac{\partial X_{T_{\mathrm{int}_{i,h}}}}{\partial[V_{F_{T_{j,k}}}]}\right)B_{V_{F_{R_j}}[V_{F_{T_{j,k}}}]}+\frac{V_R}{V^2}\sum_{j=1}^{6}(m_{i,j}k_j)\left(\frac{\partial X_{T_{\mathrm{int}_{i,h}}}}{\partial V_{F_{T_{z_j}}}}\right)B_{V_{F_{R_j}}V_{F_{T_{z_j}}}} \\
&-\frac{V_{R_z}}{V^2}\sum_{j=1}^{6}\sum_{k=1}^{N}(m_{i,j}k_j)\left(\frac{\partial X_{T_{\mathrm{int}_{i,h}}}}{\partial[V_{F_{T_{j,k}}}]}\right)B_{V_{F_{R_{z_j}}}[V_{F_{T_{j,k}}}]}-\frac{V_{R_z}}{V^2}\sum_{j=1}^{6}(m_{i,j}k_j)\left(\frac{\partial X_{T_{\mathrm{int}_{i,h}}}}{\partial V_{F_{T_{z_j}}}}\right)B_{V_{F_{R_{z_j}}}V_{F_{T_{z_j}}}}
\end{aligned}
\tag{6.21}
$$

The calculation of the aerodynamic loads shares no variables, measurements or common data acquisition channels as the dynamic pressure calculation. The uncertainty contribution from any of the constants, K_i is considered negligible as $C_{X_i} << K_i$ and the uncertainty, U_{K_i} is considered small. The uncertainty of the aerodynamic coefficients is thus

$$
\begin{aligned}
U_{C_{X_i}}^2 &= \left(\frac{\partial C_{X_i}}{\partial X_i}\right)^2 U_{X_i}^2+\left(\frac{\partial C_{X_i}}{\partial q}\right)^2 U_q^2 \\
&= \left(\frac{1}{qK_i}\right)^2 U_{X_i}^2+\left(\frac{C_{X_i}}{q}\right)^2 U_q^2
\end{aligned}
\tag{6.22}
$$

The precision limit in the preceding equations was presented as $2S_x$, which implies we are 95% confident the next reading will fall between $\pm U_x$. Static tests are typically interested in averages over time periods that are large relative to the time scales of factors that have significant influence on the data and the random content in the data. If an average is the objective of the test, the uncertainty for the mean $\pm U_{\bar{x}}$ is a better metric, thus $2S/\sqrt{N}$ should be used for the precision limit.

6-4 Static tests results of fighter model

Typically static data is acquired at 10 Hz for a sample period of 8 seconds and filtered with a 1 Hz low-pass 2-pole Butterworth anti-aliasing filter at the wind tunnel facility used for this research. Selected static runs and their appropriate tares throughout the tests were sampled at 200 Hz for a sample period of 20 seconds and filtered at 100 Hz. The higher frequency filter and faster sample rate were chosen to capture a broad spectrum of the observed model dynamics. The longer sample period was selected to observe how the mean and standard deviation vary with time. The sample rate of the run will be indicated for each example. The auto-ranging

function of the data acquisition system was used for all channels. Auto-ranging optimizes the resolution of the data, however it periodically changes gains for no apparent reason when a data sample is recorded. The change in gains is usually one binary step over the sample period. The minimum gain that was used during the sample will be used to calculate the uncertainty in the NEFF ADC for that channel as it gives the most conservative estimate of uncertainty. No significant temperature change was observed in the air conditioned control room, where the data acquisition system is housed, thus no temperature effects will be taken into account. Time histories of static run data are traditionally not saved. All data is normally saved as averages. No time histories for tares, tare zeros or run zeros are available. Estimates of their uncertainties will be considered to be equal to the calculated uncertainties for the zero α condition of the run.

6-4.1 Total uncertainty from propagation

The uncertainty of all balance loads for both models vary with the angle-of-attack. As one would expect, the variance of the forces and moments increase with ±α and peak near stall as the flow transitions from fully attached to fully separated. The flow in this transition region often induces adverse model dynamics as such was the case with the fighter model discussed in Ch. 3. Figures 6.1 through 6.6 are the results of the uncertainty propagation for the body axis aerodynamic coefficients of the fighter model from one run on the FO rig. The uncertainties shown are the 95% confidence limits of the next reading. The 95% confidence limits of the uncertainty of the mean are not shown because they rapidly approach the bias as the number of readings approaches infinity. The 95% confidence limits near stall are nearly 25% of the overall range of the normal force coefficient (figure 6.1). The majority of uncertainty in the normal force coefficient after filtering is due to the systematic error or bias. The majority of the bias is comes from the second term in Eq. (6.22) which is due to the dynamic pressure. Equation (6.22) shows the low dynamic pressure and high normal force coefficient values magnify the uncertainty from the dynamic pressure, which is approximately 97% $U_{c_{prime}-regress}$ over the range of the pressure transducer. The same trend can be seen in all other coefficients but it is not as dramatic as with normal force because the other coefficients are much smaller than 1. Thus the uncertainty contribution from the balance dominates the uncertainty contribution of all other coefficients. Most of the dynamics that occur during a traditional test are lost due to the standard 1 Hz low pass filter. For instance, with unfiltered data, the 95% confidence limits for the yawing moment coefficient near stall, with all control surfaces at zero, are greater than the control power of the aircraft. The yawing moment and side force axes are aligned with the gravity vector on a cantilevered support, which would explain some of the variation in the two coefficients before filtering.

6-4.2 Spectral content

The fighter model in the previous results was bottom mounted as shown in figure 3.3a and the FO rig was set up for yaw oscillations as shown in figure 3.3c. The FO rig was locked from oscillating at zero θ_z for the static test while the data from the run and the tare were each sampled at 200 Hz and used 100 Hz anti-aliasing filters. Notice, in figures 6.1 through 6.6, the large difference between the total uncertainty of the sampled data (filtered as described above) and the total uncertainty of the post-filtered data, which was digitally filtered at 1 Hz with a low-pass Inverse Fast Fourier Transform (IFFT) filter, described in appendix A.

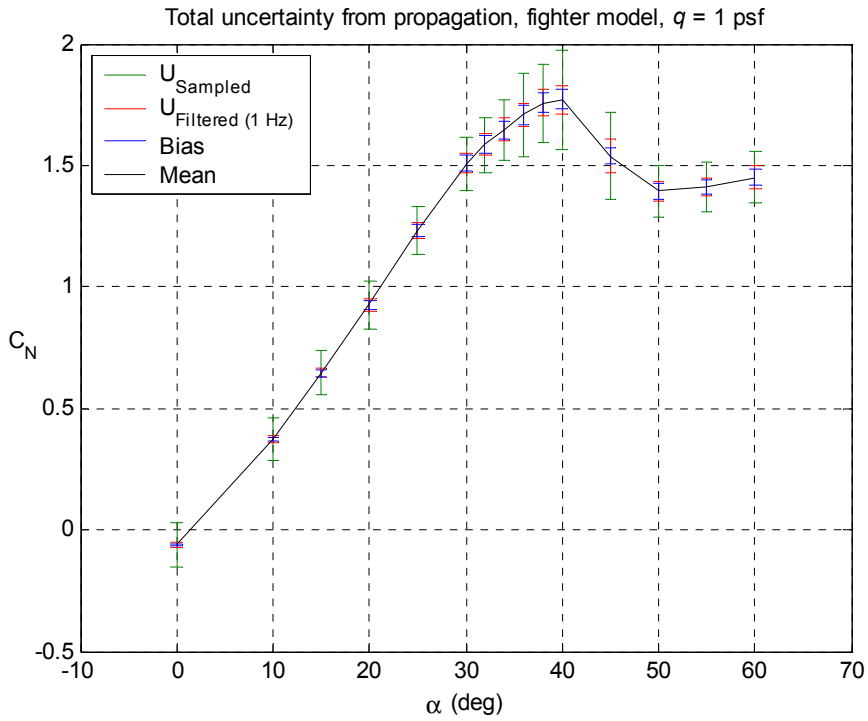

Figure 6.1 Total uncertainty of normal force coefficient from propagation method for sampled and post-filtered data verses the bias contribution.

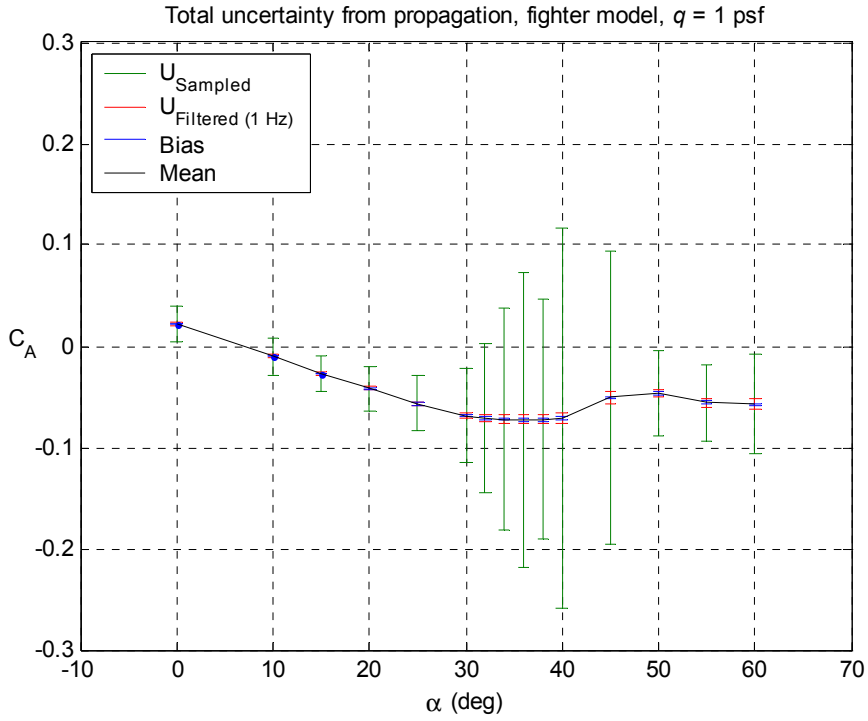

Figure 6.2 Total uncertainty of axial force coefficient from propagation method for sampled and post-filtered data verses the bias contribution.

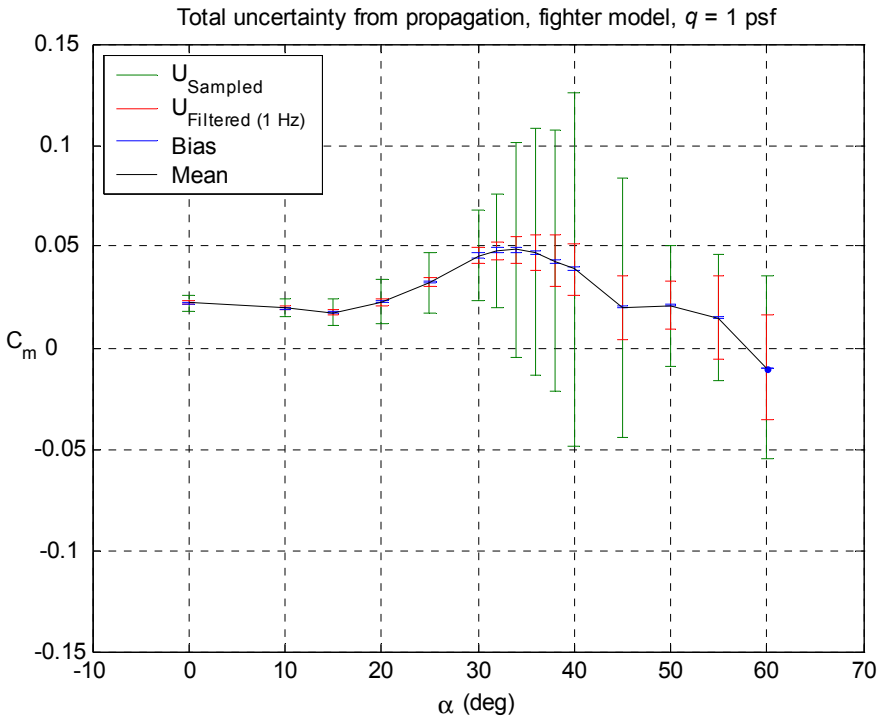

Figure 6.3 Total uncertainty of pitching moment coefficient from propagation method for sampled and post-filtered data verses the bias contribution.

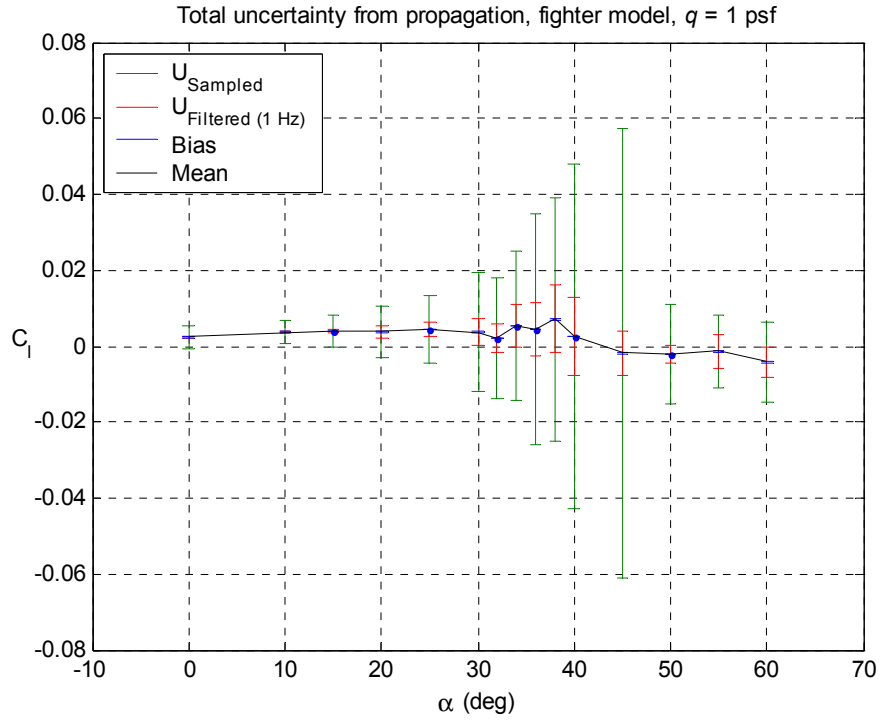

Figure 6.4 Total uncertainty of rolling moment coefficient from propagation method for sampled and post-filtered data verses the bias contribution.

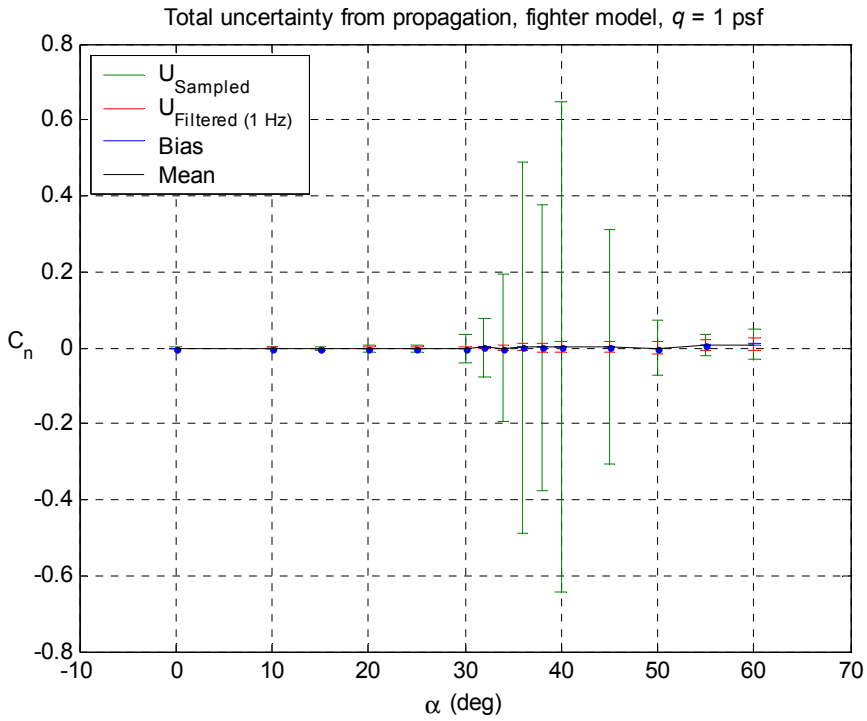

Figure 6.5 Total uncertainty of yawing moment coefficient from propagation method for sampled and post-filtered data verses the bias contribution.

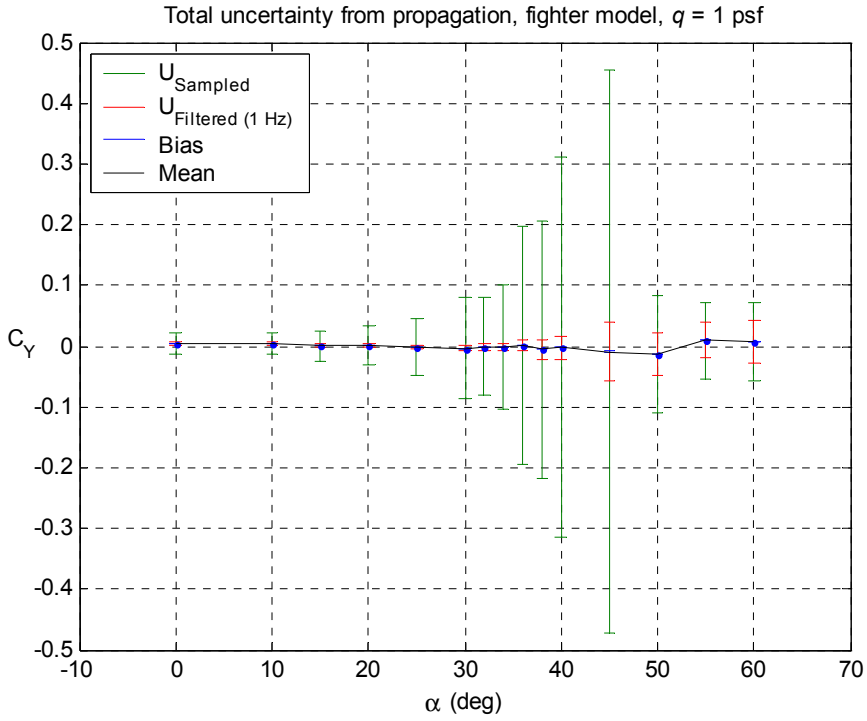

Figure 6.6 Total uncertainty of side force coefficient from propagation method for sampled and post-filtered data verses the bias contribution. Note the magnitude of the uncertainty of the sampled data.

Consider the data used to calculate the coefficients presented in figures 6.1 through 6.6 at 40º angle-of-attack. The power spectral magnitude can be estimated using MATLAB's built-in function, psd, which uses Welch's averaged, modified periodogram method with a Hanning window [16]. This method was employed purely for convenience and intended solely for estimation of spectral content. The data records were 4000 samples each. No overlap or detrending mode was used [17]. A tradeoff exists between spectral resolution and the accuracy of the power spectrum estimate [18]. Longer data records give better frequency resolution as $\Delta f = 1/T$, where Δf is the frequency resolution and T is the period of the data record. However, higher resolution comes at a cost to accuracy of the magnitude estimate. Figures 6.7 through 6.22 show the power spectrums of each signal acquired by the data acquisition system during the run and the spectrums of a Ground Vibration Test or GVT. Two power spectrum estimates are shown on each figure; one with 4000 sample window for frequency resolution and the other with a 250-sample window, along with its 95% confidence intervals, for estimation of the magnitude of each spectral line. The mean of each signal was removed from the spectrum, as it provides no insight to the random component of the signal.

A GVT was done simply by recording time histories of all channels and impacting the model once by hand. Two GVTs where done for each moment axis for each model setup at null conditions i.e. $q = 0$, $\alpha = 0$, etc. The GVTs presented below are the results of one impact in on the side of the nose of the model, which was in the gravity vector and produced a yawing moment.

The balance excitation voltage is 5 VDC. Its spectrum during the run and during GVT, figures 6.7 and 6.8 respectively are just what one would expect for a constant signal with random white noise. Figure 6.7 is the type of spectrum ideal "static" data should have, i.e. flat! However, as discussed in chapter 3, static wind tunnel tests, no matter how good the flow quality, will often contain spectral content other than random white noise. Figures 6.8 through 6.22, for example all contain 60 Hz noise which could possibly be emitted by the lights in the test section and has nothing to due with the aerodynamics. Notice the spectral content in the GVT for the dynamic pressure signal, where the wind is off, is very similar to that in the wind on spectrum (figure 6.22 and 6.21 respectively). The causes of these frequencies are not yet understood. The model has been observed to oscillate during static testing and so the spikes around 5 Hz in all of the balance signals are most likely the first dynamic modes of the support structure or the sting, which the GVTs support. These oscillations affect the static aerodynamics. References [19] and [5] among others, have shown aerodynamics have a "time history effect", that is the aerodynamics of a model at a current state depend on previous states. The amplitudes of dynamic tests in references [19] and [5] are usually large relative to the amplitudes observed from static tests. Nonetheless, the broad range of spectral content in the balance signals leaves no guarantee the means of dynamic time histories would equal to that of a purely static model. However, it will be assumed, as is typically done in practice, the frequencies of the aerodynamics of interest lie below 1 Hz and hence the data will be post-filtered as described above.

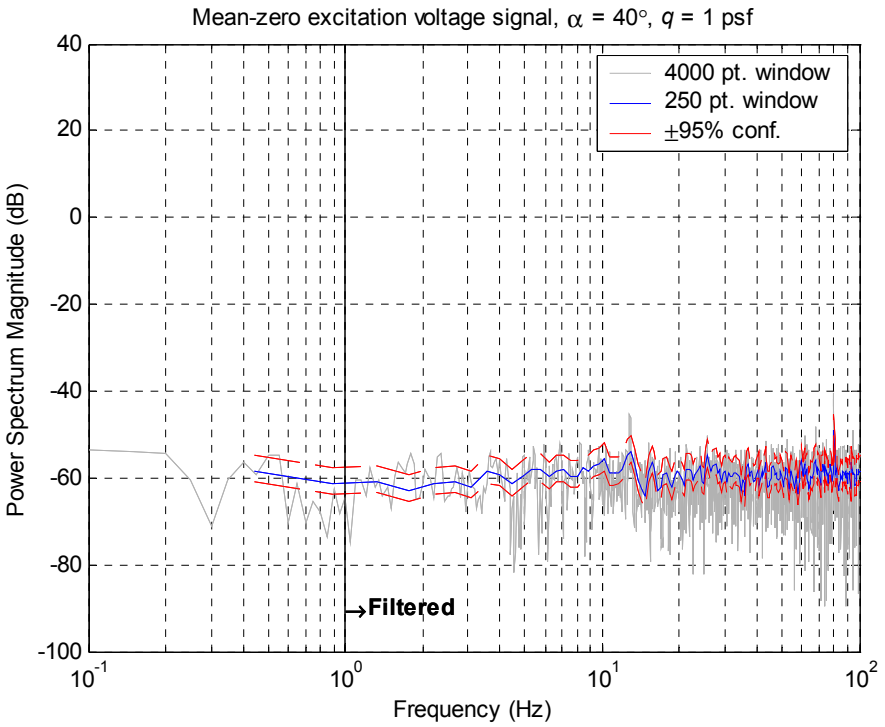

Figure 6.7 Power spectrum of mean zero balance excitation voltage signal from run.

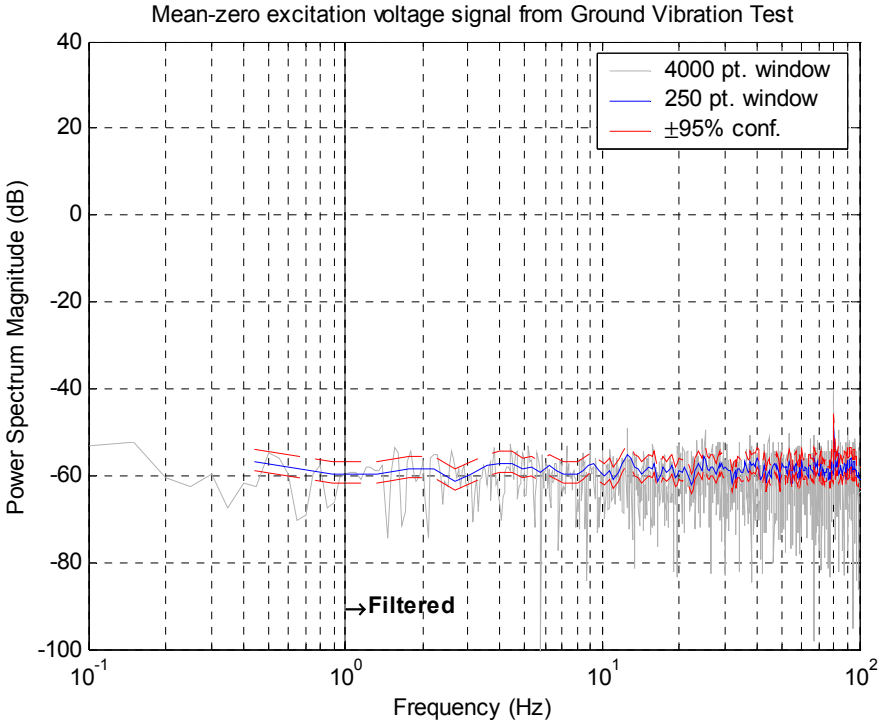

Figure 6.8 Power spectrum of mean zero balance excitation voltage signal from GVT.

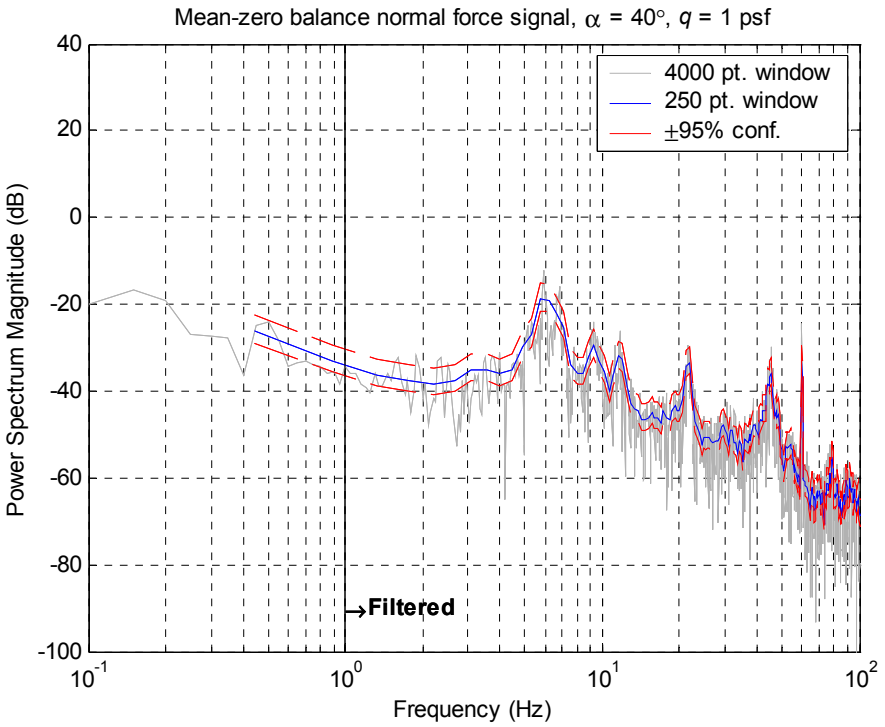

Figure 6.9 Power spectrum of mean zero normal force signal of the balance from run.

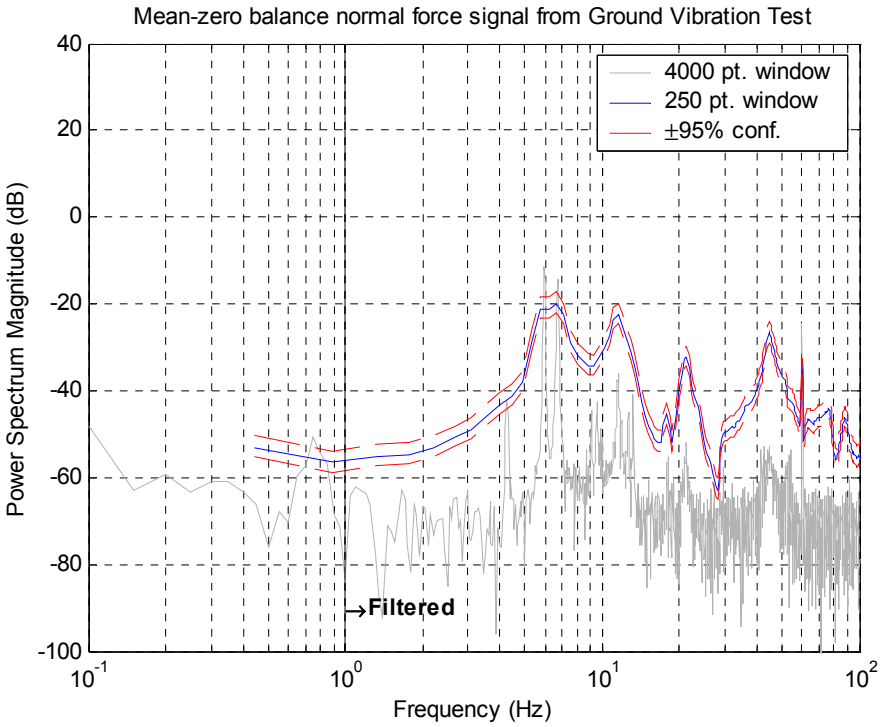

Figure 6.10 Power spectrum of mean zero normal force signal of the balance from GVT.

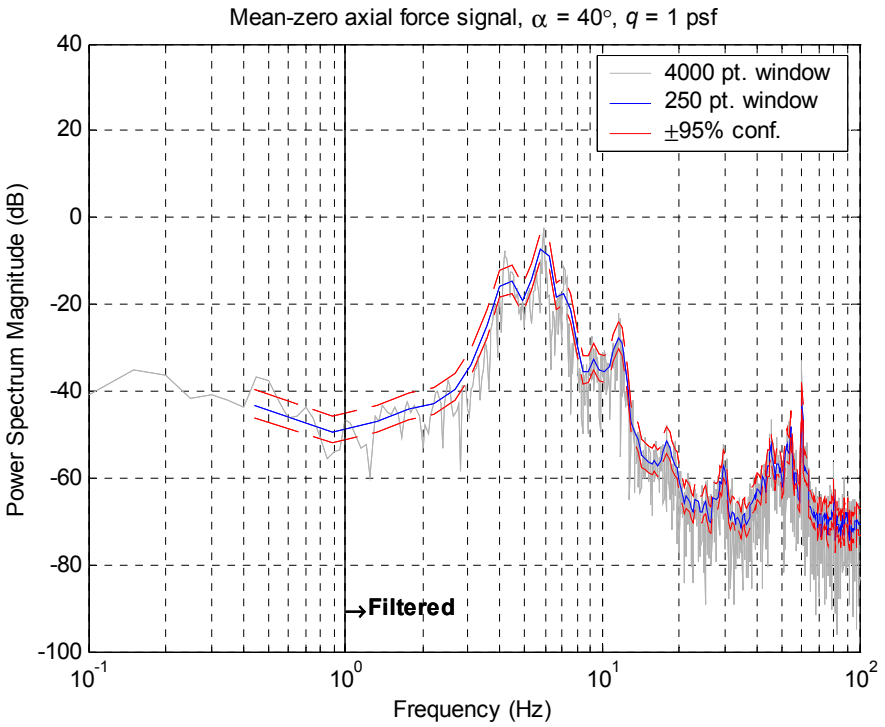

Figure 6.11 Power spectrum of mean zero axial force signal of the balance from run.

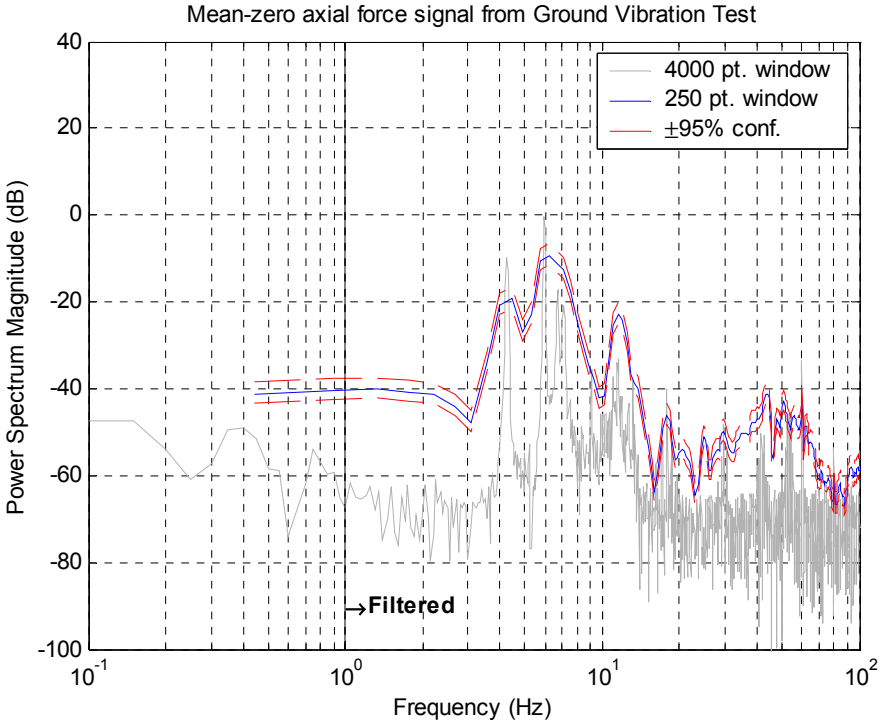

Figure 6.12 Power spectrum of mean zero axial force signal of the balance from GVT.

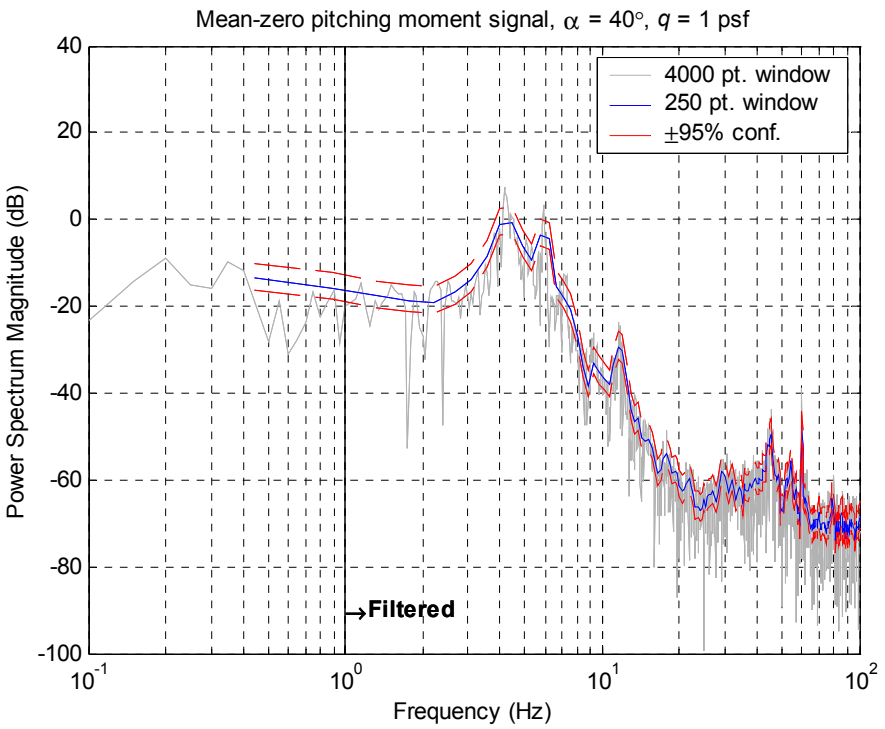

Figure 6.13 Power spectrum of mean zero pitching moment signal of the balance from run.

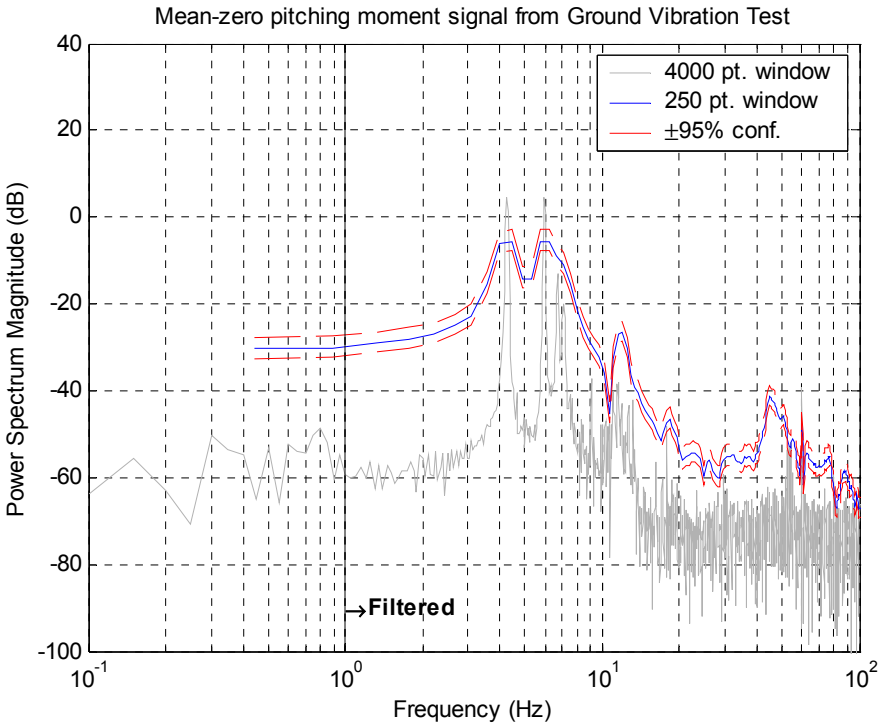

Figure 6.14 Power spectrum of mean zero pitching moment signal of the balance from GVT.

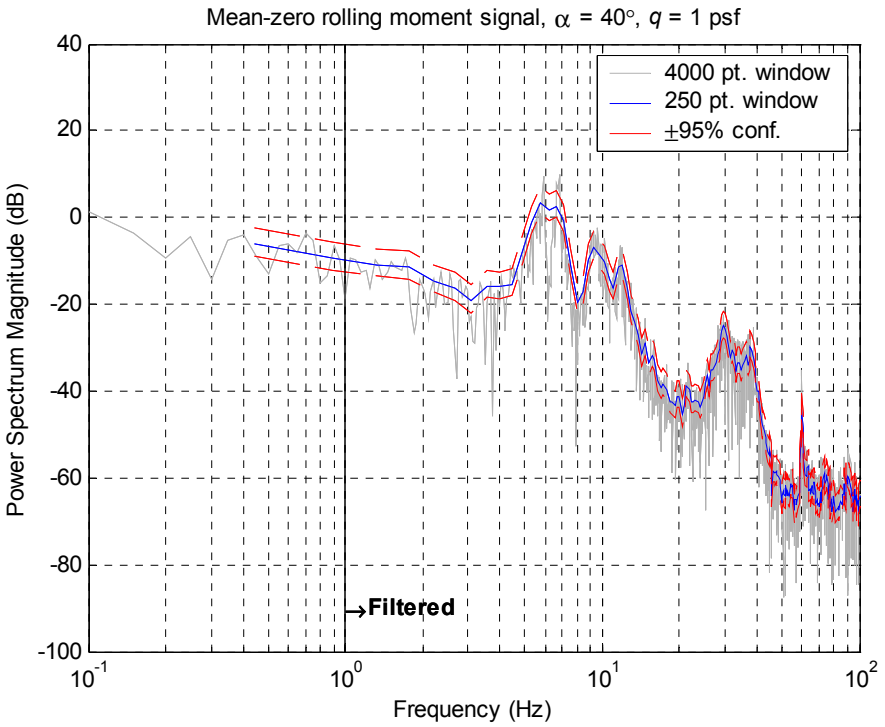

Figure 6.15 Power spectrum of mean zero rolling moment signal of the balance from run.

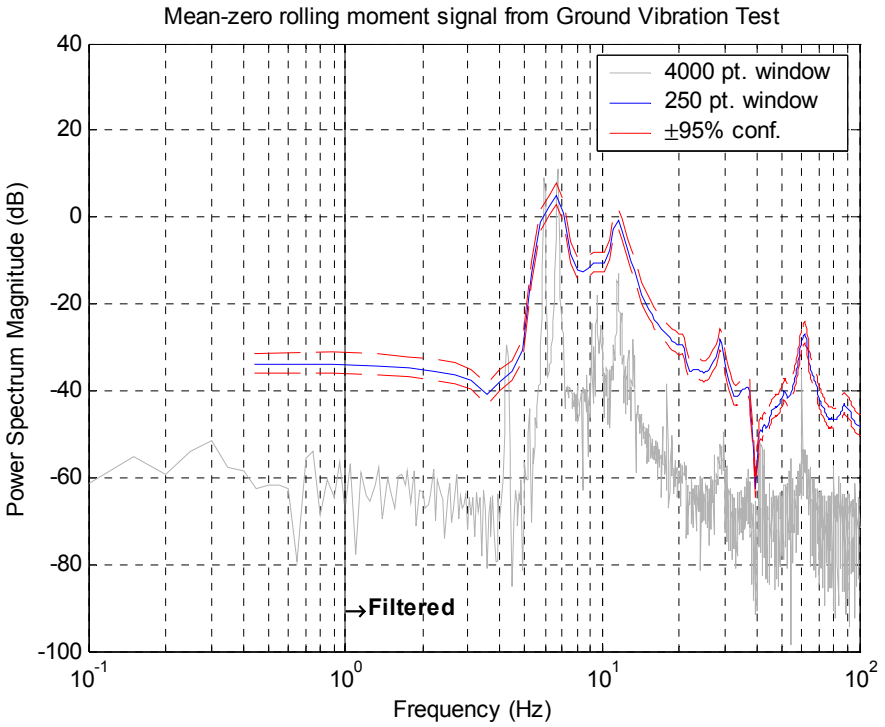

Figure 6.16 Power spectrum of mean zero rolling moment signal of the balance from GVT.

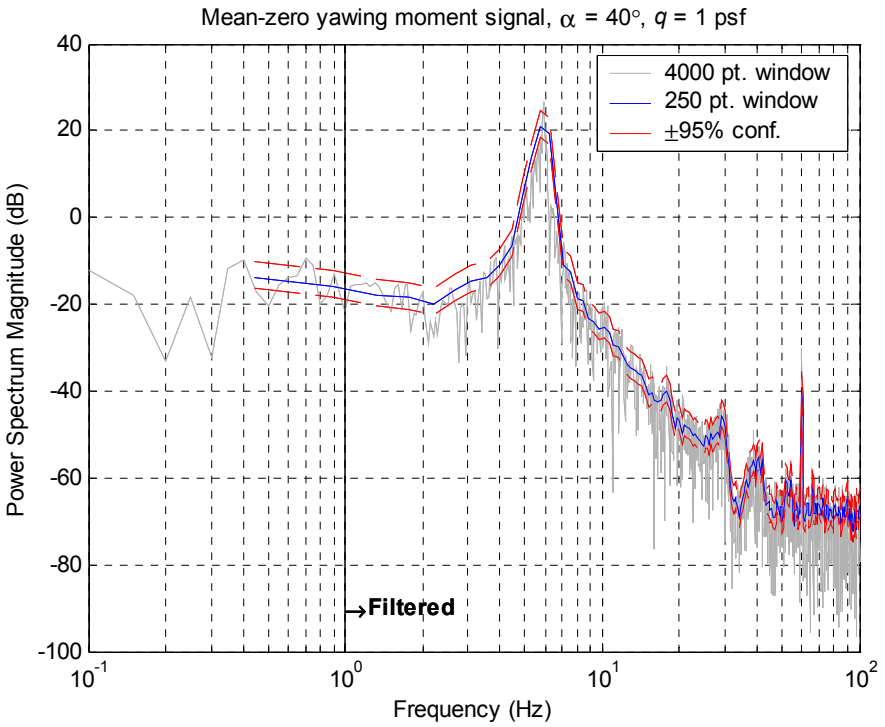

Figure 6.17 Power spectrum of mean zero yawing moment signal of the balance from run.

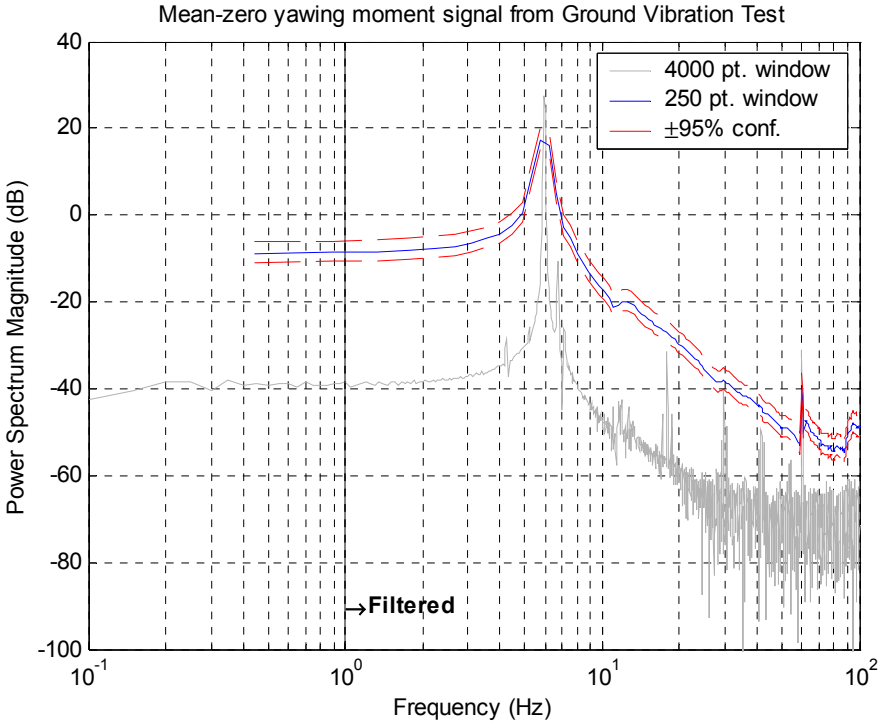

Figure 6.18 Power spectrum of mean zero yawing moment signal of the balance from GVT.

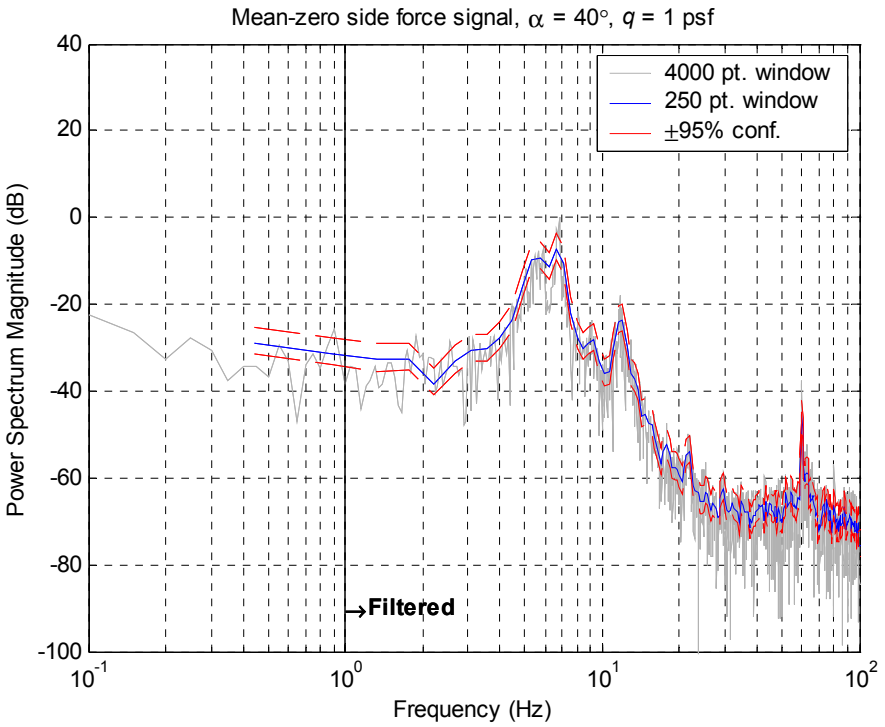

Figure 6.19 Power spectrum of mean zero side force signal of the balance from run.

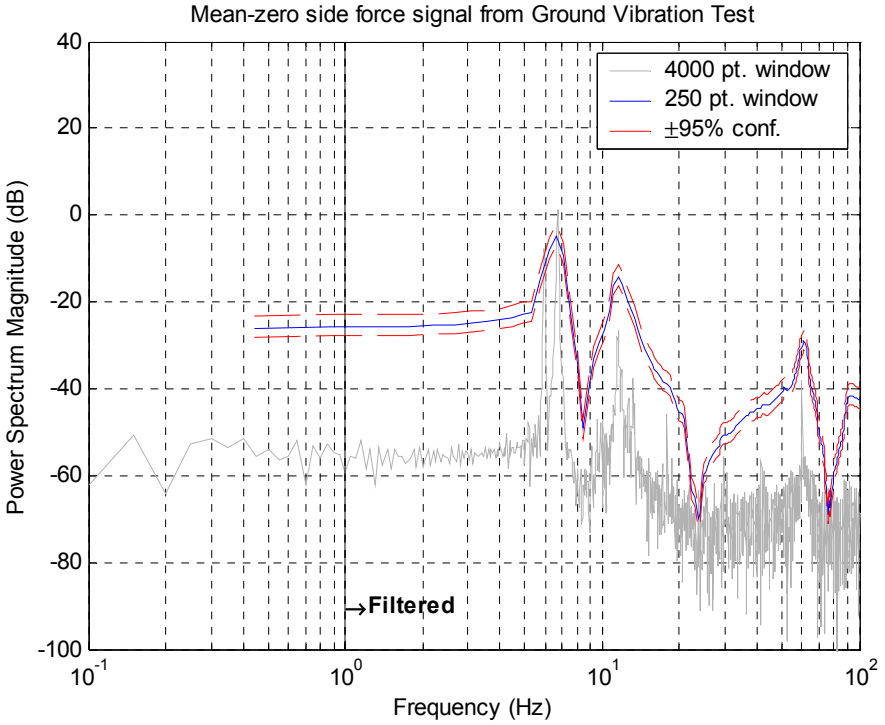

Figure 6.20 Power spectrum of mean zero side force signal of the balance from GVT.

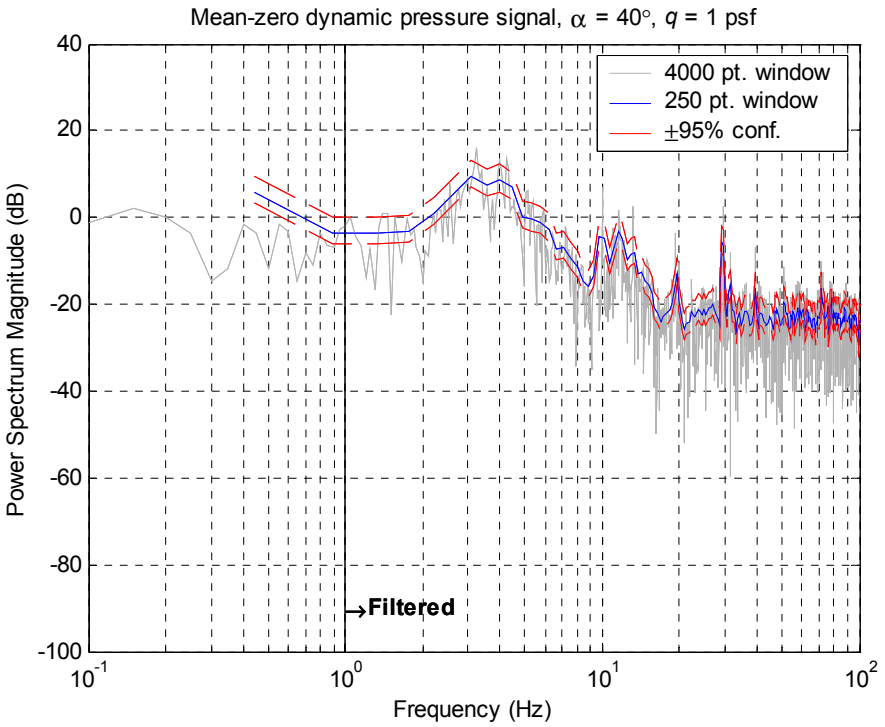

Figure 6.21 Power spectrum of mean zero dynamic pressure signal from run.

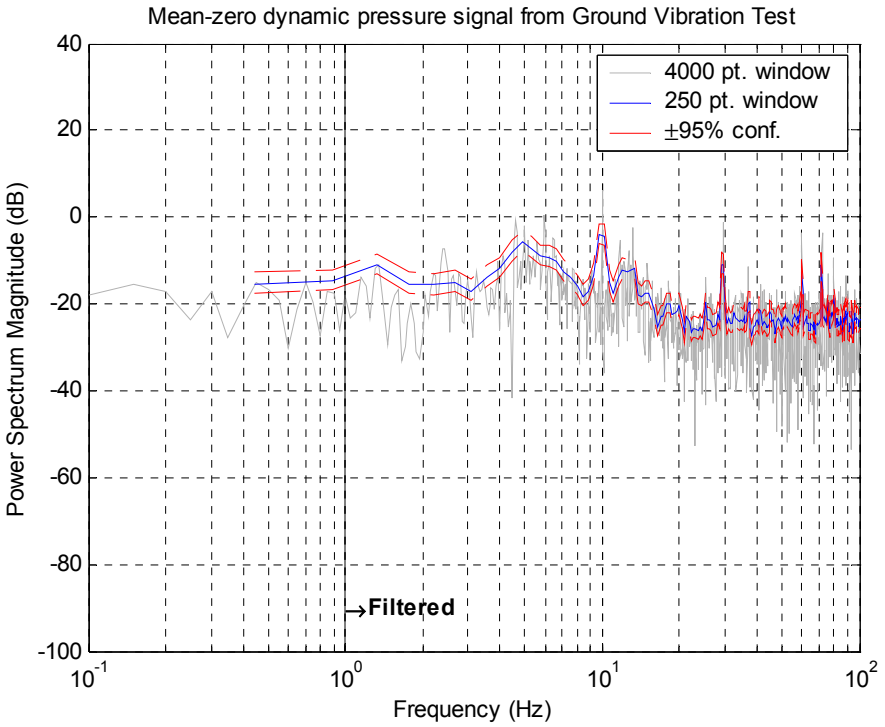

Figure 6.22 Power spectrum of mean zero dynamic pressure signal of the balance from GVT.

6-4.3 Random uncertainty directly from the result

Direct determination of the random uncertainty of the result was discussed in chapter 2. If all time histories were saved during the static tests, direct determination of the random uncertainty of the coefficients would be straightforward. However, one would expect the random uncertainty of the tares, tare zeros and run zeros to be negligible compared to the random uncertainty of the wind-on run. Computing the standard deviation of a time history of coefficients would certainly be computationally simpler than propagating the random uncertainty through to the result however; the systematic uncertainty must still be propagated. Figures 6.23 through 6.28 show the coefficient results after filtering and compare the total uncertainty from propagation, $U_{propagation}$ and total uncertainty from combining the propagated bias with the random uncertainty directly from the result, U_{Direct}. Note the scales are different than those before. Again, the 95% confidence limits of the uncertainty of the mean are not shown. In most cases the uncertainty direct from the result is the same as the uncertainty found from propagation. This is important because it implies there are little to no correlated random uncertainties and it indicates the propagation was done correctly. The only component with any consistent difference between $U_{propagation}$ and U_{Direct} is side force (figure 6.28). Yawing moment has the largest interaction with side force. There could be a correlation between the random uncertainty with the yawing moment signal and the random uncertainty of the side force signal. However the difference between the two methods is considered negligible. The direct method will be used to estimate the random uncertainty contribution from this point forward.

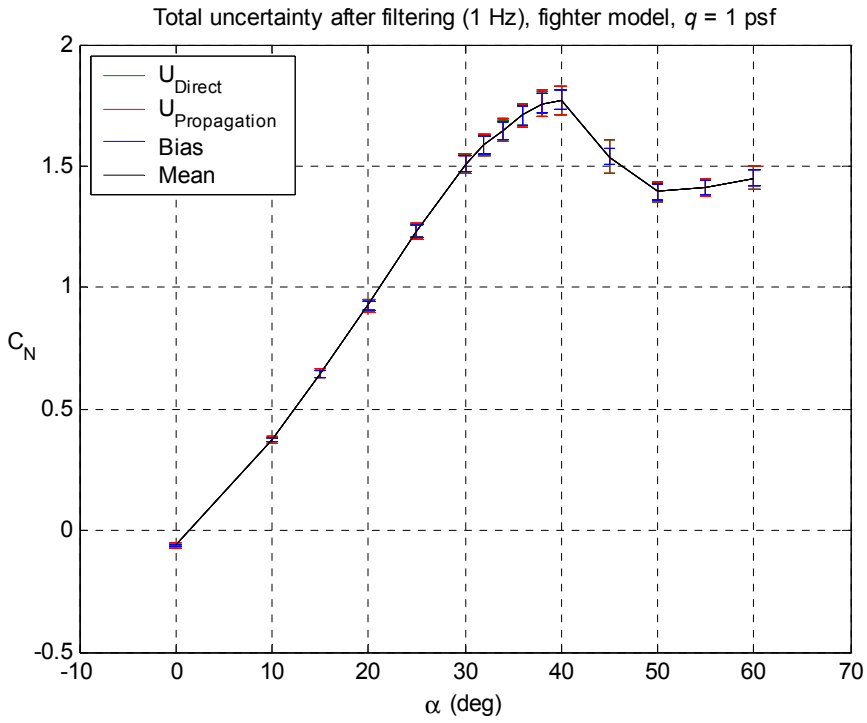

Figure 6.23 Total uncertainty of normal force coefficient from propagation and direct determination of random uncertainty after low-pass filtering at 1 Hz.

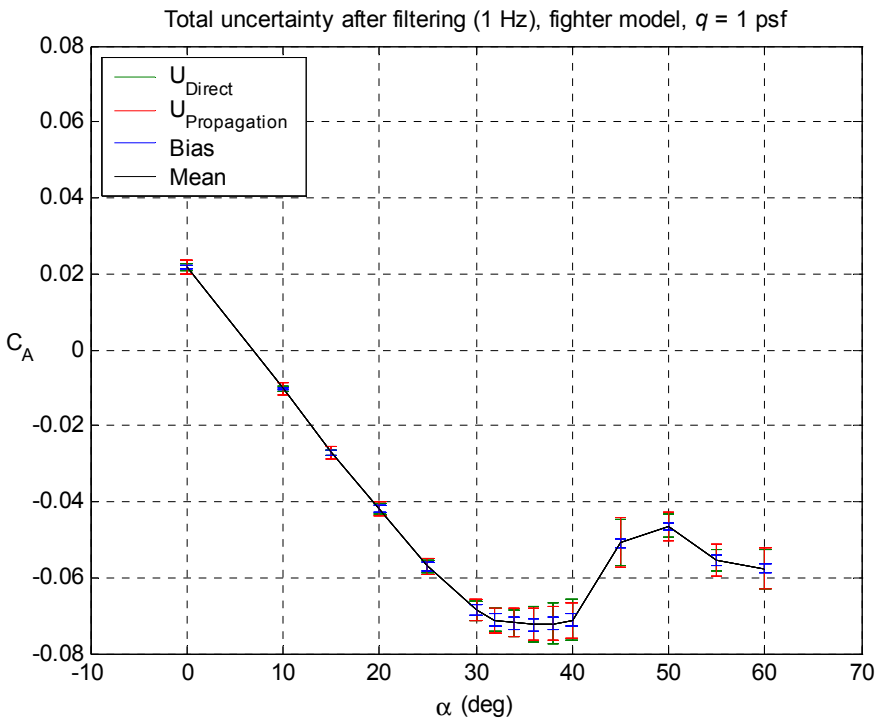

Figure 6.24 Total uncertainty of axial force coefficient from propagation and direct determination of random uncertainty after low-pass filtering at 1 Hz.

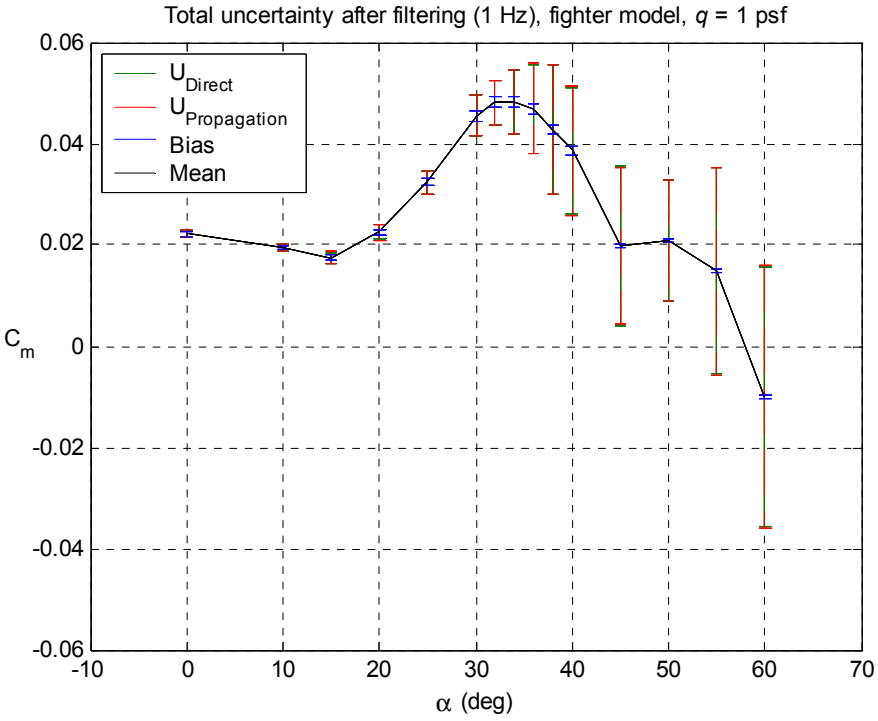

Figure 6.25 Total uncertainty of pitching moment coefficient from propagation and direct determination of random uncertainty after low-pass filtering at 1 Hz.

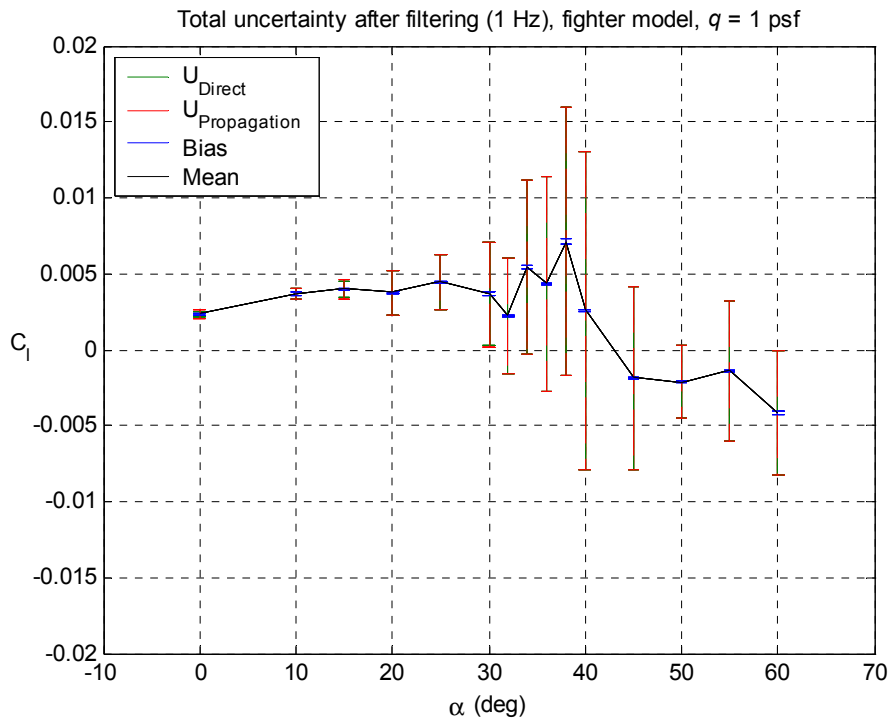

Figure 6.26 Total uncertainty of rolling moment coefficient from propagation and direct determination of random uncertainty after low-pass filtering at 1 Hz.

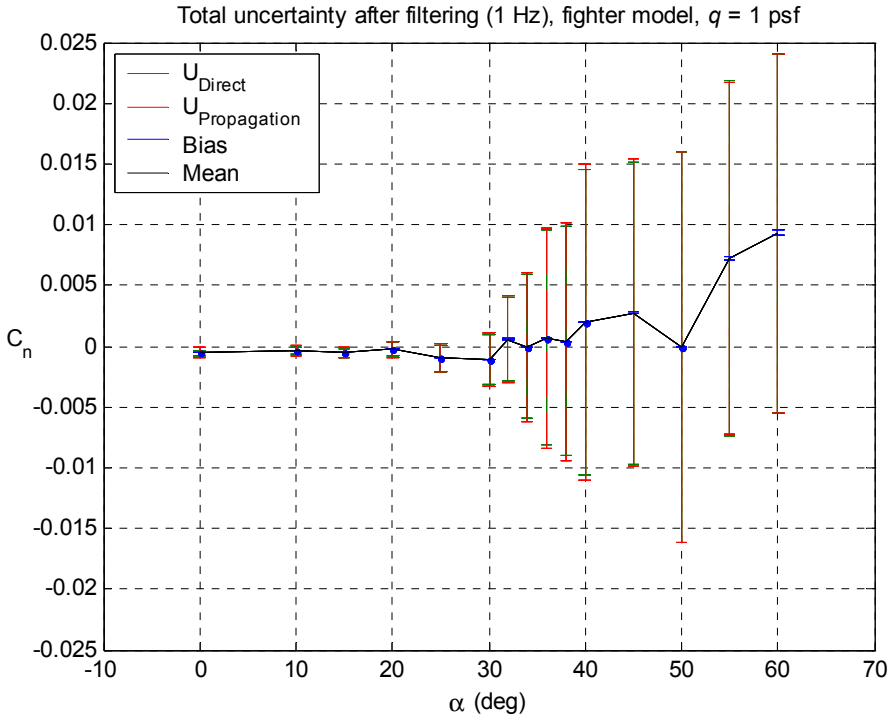

Figure 6.27 Total uncertainty of yawing moment coefficient from propagation and direct determination of random uncertainty after low-pass filtering at 1 Hz.

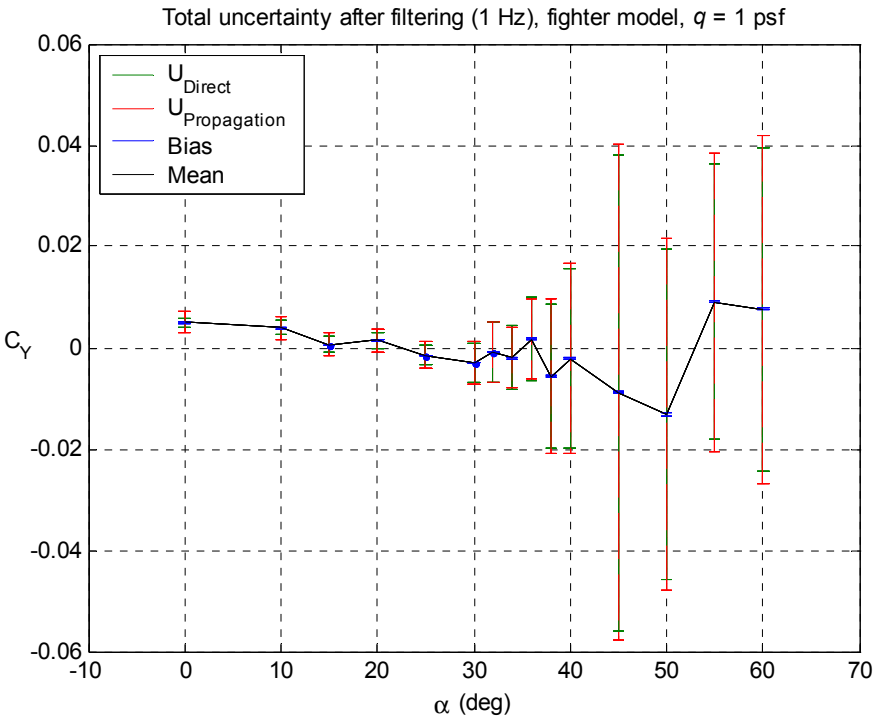

Figure 6.28 Total uncertainty of side force coefficient from propagation and direct determination of random uncertainty after low-pass filtering at 1 Hz.

7 Uncertainty in Forced Oscillation

7-1 Introduction

Forced oscillation tests use the same internal strain-gauge balance as used in static testing to measure the forces and moments of the model. The major difference between static testing and forced oscillation for determining aerodynamic loads is the addition of inertial loads created by the oscillations, which need to be removed in addition to gravity tares. Models oscillate and vibrate during static tests, however models are routinely forced to oscillate at amplitudes up to 30º at frequencies greater than 1 Hz in dynamic tests. Strain-gauge balances can be thought of as a coupled multi-axis mass-spring-damper system with several natural frequencies ranging anywhere from around 30 Hz up to the neighborhood of 120 Hz, however coupling of balance models can give substantially lower natural frequencies. These frequencies could easily be excited by perturbations from mechanical imperfections of the FO rig. Several open issues remain regarding the current measurement of dynamic testing – including what happens to the nonlinear interactions under dynamic conditions and what implications do multi-axis oscillatory motions have on the accuracy of the balance over its range? These issues will not be addressed here.

7-2 Forced oscillation force and moment measurement process

The data reduction process for forced oscillation testing is somewhat similar to that of static testing. The first difference arises from a purely operational inconvenience. The FO rig allows no direct control of the position of the model about the oscillation axis. Oscillations can only be turned on or off. The model must be manually set to a reference position if so desired. This process is cumbersome and time-consuming. As a result no electrical zeros are removed from the balance signals before each the run and the tare. The measured balance loads are thus

$$X_{I_{U_i}} = \frac{k_i}{V} V_{F_I} \frac{V_I}{V} = \frac{k_i V_{F_I} V_I}{V^2} \tag{7.1}$$

A consequence of not removing electrical offsets is that tares and runs are recorded back to back with the assumption the electrical offsets do not change. Interactions are then applied using Eq. (6.10). Forced oscillation tares are oscillated at the same amplitude and frequency as the run, however; tares are only recorded at one attitude, typically at zero α, as the gravity vector with respect to the model is assumed not to change as the turntable is positioned. These tares are not only weight tares but serve as inertial tares as well.

Traditionally data is sampled at 200 Hz for 40 sinusoidal periods or 40 cycles. The ADT is also sampled to record the time history of the cycle position, θ. Variable frequencies and amplitudes with a fixed sample rate give rise to variable position samples, meaning samples are not recorded at the same cycle position for each cycle. For this reason each cycle must be interpolated from the data acquisition time-stamp time-history. Cycle endpoints are found by

interpolating the time, t where $\theta = 0$ and the angular rate, $\dot{\theta} > 0$, where $\dot{\theta}$ can be approximated by a forward difference. The slope of the position at $\theta = 0$ is approximately linear with time so a linear interpolation can be used to find $t_{\theta=0}$ such that

$$t_{I_{\theta=0_k}} = t_{I_j} + (t_{I_{j+1}} - t_{I_j}) \frac{(\theta - \theta_{I_j})}{(\theta_{I_{j+1}} - \theta_{I_j})} \tag{7.2}$$

Here the subscripts k and j represent the k^{th} endpoint and j^{th} point in the sample record respectively. The next step is to interpolate n points within the period of each cycle so that θ_T aligns with θ_R when the tare loads are removed from the run loads and then reduced by the dynamic pressure. The sample rate is high enough such that the spacing between samples at the peaks of the cycles are small. Experience has shown a cubic spline often produces unrealistic interpolations at closely spaced peaks. For this reason a linear interpolation of the form

$$y = y_j + (y_{j+1} - y_j) \frac{(x - x_j)}{(x_{j+1} - x_j)} \tag{7.3}$$

was used to interpolate the tare and run loads and angular position such that

$$X_{I_{Int_{k,h}}} = X_{I_{i,j}} + (X_{I_{i,j+1}} - X_{I_{i,j}}) \frac{(t_{I_{k,h}} - t_{I_j})}{(t_{I_{j+1}} - t_{I_j})} \tag{7.4}$$

$$\theta_{I_{Int_{k,h}}} = \theta_{I_j} + (\theta_{I_{j+1}} - \theta_{I_j}) \frac{(t_{I_{k,h}} - t_{I_j})}{(t_{I_{j+1}} - t_{I_j})} \tag{7.5}$$

where

$$t_{I_{k,h}} = t_{I_{\theta=0_k}} + \frac{(t_{I_{\theta=0_{k+1}}} - t_{I_{\theta=0_k}})}{n-1} (h-1) \tag{7.6}$$

and

$$h = 1,2,...n$$

Here $t_{k,h}$ is the interpolated time of the k^{th} cycle. The subscript h is the h^{th} element in the n length time vector. The FO rig uses a DC motor, which is not able to hold a constant angular-rate under the varying aerodynamic and inertial loads through the oscillations. The varying angular-rate results in a slightly varying frequency throughout the sample record. These variations can be observed during the test on a frequency counter in the control room, typically around ±0.01 Hz. Unfortunately, neither the angular-rate of the motor nor the frequency was recorded. The interpolated cycles for each run and tare respectively are then averaged to one cycle as

$$\overline{X}_{I_{Int_{i_h}}} = \frac{1}{N}\sum_{k=1}^{N} X_{I_{Int_{k,h}}} \tag{7.7}$$

$$\overline{\theta}_{I_{Int_h}} = \frac{1}{N}\sum_{k=1}^{N} \theta_{I_{Int_{k,h}}} \tag{7.8}$$

Next the averaged interpolated tare is subtracted from the averaged interpolated run to get the final aerodynamic loads, *X* such that

$$X_{i_h} = \overline{X}_{R_{\text{int}_{i_h}}} - \overline{X}_{T_{\text{int}_{i_h}}} \tag{7.9}$$

Finally, the aerodynamic coefficients are found from

$$C_{X_{i_h}} = \frac{X_{i_h}}{\overline{q}K_i} \tag{7.10}$$

where, $\overline{q}$ is the time average of the dynamic pressure over the run, such that

$$\overline{q} = \frac{1}{N}\sum_{j=1}^{N} q_j \tag{7.11}$$

7-3 Uncertainty of forced oscillation aerodynamic coefficients

The systematic uncertainty of the uncorrected loads and the corrected loads is essentially the same as with the static test, with the exception of the zeros such that

$$B^2_{X_{I_{U_i}}} = U^2_{k_i-regress} + \frac{k_i^2}{V^4} V_I^2 B^2_{V_{F_{I_i}}} + \frac{k_i^2}{V^4} V^2_{F_{I_i}} B^2_{V_I} \tag{7.12}$$

$$B^2_{X_{I_i}} = B^2_{[X_{I_i}]} + \left(\frac{\left[m_{i,1\ldots6}\right] \kappa V_{F_I}}{V^2} \right)^2 B^2_{V_I} + \frac{V_I^2}{V^4} \sum_{j=1}^{6} \left(m_{i,j} k_j\right)^2 B^2_{V_{F_{I_j}}} \tag{7.13}$$

The auto-range function is not used for forced oscillation tests, so the systematic error for each balance channel is constant. The voltage ratio was applied before the data was stored and no time history of the excitation voltage is available so it and its systematic error is constant as well. The only variables in Eq. (7.13) that are not constant are the balance voltages and the random uncertainties. Random uncertainties will be estimated directly from the result of the average cycle, i.e

$$S_{\overline{X}_{I_{Int_{i_h}}}} = \sqrt{\frac{1}{N-1}\sum_{k=1}^{N} (X_{I_{Int_{k,h}}} - \overline{X}_{I_{Int_{i_h}}})^2} \tag{7.14}$$

$$S_{\bar{\theta}_{I_{Int_h}}} = \sqrt{\frac{1}{N-1}\sum_{k=1}^{N}(\theta_{I_{Int_{k,h}}} - \bar{\theta}_{I_{Int_h}})^2} \tag{7.15}$$

and the random uncertainty of the dynamic pressure is found from its standard deviation,

$$S_q = \sqrt{\frac{1}{N-1}\sum_{j=1}^{N}(q_j - \bar{q})^2} \tag{7.16}$$

The standard deviations above are then propagated into the aerodynamic loads with a coverage factor for 95% confidence, ie 2. The systematic errors will still have to be propagated. Recall the "random" uncertainties are all non-repeatable measurements at the same values of $\bar{\theta}_{I_{Int_h}}$.

The next step in propagating the systematic errors comes with interpolating the time of where a cycle starts, Eq. (7.2). First consider the general form of the uncertainty of a linear interpolation,

$$\begin{aligned} U_y^2 = &\left(\frac{\partial y}{\partial x}\right)^2 U_x^2 + \left(\frac{\partial y}{\partial x_j}\right)^2 U_{x_j}^2 + \left(\frac{\partial y}{\partial x_{j+1}}\right)^2 U_{x_{j+1}}^2 + 2\left(\frac{\partial y}{\partial x}\right)\left(\frac{\partial y}{\partial x_j}\right) U_x U_{x_j} \\ &+ 2\left(\frac{\partial y}{\partial x}\right)\left(\frac{\partial y}{\partial x_{j+1}}\right) U_x U_{x_{j+1}} + 2\left(\frac{\partial y}{\partial x_{j+1}}\right)\left(\frac{\partial y}{\partial x_j}\right) U_{x_{j+1}} U_{x_j} \\ &+ \left(\frac{\partial y}{\partial y_j}\right)^2 U_{y_j}^2 + \left(\frac{\partial y}{\partial y_{j+1}}\right)^2 U_{y_{j+1}}^2 + 2\left(\frac{\partial y}{\partial y_j}\right)\left(\frac{\partial y}{\partial y_{j+1}}\right) U_{y_j} U_{y_{j+1}} \end{aligned} \tag{7.17}$$

It can be shown if the uncertainty associated with x, x_j, x_{j+1}, y, y_j and y_{j+1} is correlated and equal, such that Eq. (7.17) can be simplified as

$$\begin{aligned} U_y^2 = &\left[\left(\frac{\partial y}{\partial x}\right)^2 + \left(\frac{\partial y}{\partial x_j}\right)^2 + \left(\frac{\partial y}{\partial x_{j+1}}\right)^2 + 2\left(\frac{\partial y}{\partial x}\right)\left(\frac{\partial y}{\partial x_j}\right) + 2\left(\frac{\partial y}{\partial x}\right)\left(\frac{\partial y}{\partial x_{j+1}}\right) + 2\left(\frac{\partial y}{\partial x_{j+1}}\right)\left(\frac{\partial y}{\partial x_j}\right)\right] U_{x_j}^2 \\ &+ \left[\left(\frac{\partial y}{\partial y_j}\right)^2 + \left(\frac{\partial y}{\partial y_{j+1}}\right)^2 + 2\left(\frac{\partial y}{\partial y_j}\right)\left(\frac{\partial y}{\partial y_{j+1}}\right)\right] U_{y_j}^2 \end{aligned} \tag{7.18}$$

then Eq. (7.17) simplifies to

$$U_y^2 = [0]U_{x_j}^2 + [1]U_{y_j}^2 = U_{y_j}^2 \tag{7.19}$$

This situation is true for Eq. (7.5) above, if θ in Eq. (7.2) is assumed to be perfectly correlated and has equal uncertainty with the measured positions, θ_{I_j} and $\theta_{I_{j+1}}$. Technically this is not true as θ is chosen, with no uncertainty, to be zero. However, the accuracy of the ADT, uncertainty

contribution on the position from the DAC and the tolerance of the DAC time stamp are small with respect to the accuracy of the balance and the random uncertainty in the data. If the balance excitation voltage and the voltages from each balance channel were constant over the time period between t_j and t_{j+1}, then the systematic uncertainty of $X_{I_{Int_{i_{k,h}}}}$ would simply be an interpolation of the systematic uncertainties of $X_{I_{i,j}}$ and $X_{I_{i,j+1}}$. This is a reasonable assumption considering the time period between t_j and t_{j+1} is 0.05 seconds for the 200 Hz sampling rate.

Equation (2.33) has shown, if the gradients are equal and the uncertainty for each term is equal and perfectly correlated, the uncertainty of the average is equal to that of each term used in the average. The gradients of Eq. (7.8) are constant and so is the uncertainty estimation for each term; therefore the systematic error of $\overline{\theta}_{I_{Int_h}}$ is equal to the accuracy of the ADT. Chapter 5 has shown the systematic error of the dynamic pressure and the gradients of the uncertainty are functions of V_q. Considering the range of variation of the systematic error in q is less than 0.002% of q over the run its systematic error can reasonably be assumed to be constant and thus an average of the systematic uncertainty of each q_j will suffice. Neither the gradients nor the systematic uncertainties of Eq. (7.7) are constant or equal. The same assumptions as with the interpolations could be proposed except, as will be seen later, the loads vary significantly from cycle to cycle at the same cycle position. Nevertheless, the dominating term in Eq. (7.13), the balance accuracy, has a constant gradient and is equal for all readings. The balance accuracy is at least 4 orders of magnitude larger than the root-sum-square of all other bias contributions for each load. Thus, all contributions from averaging can be considered negligible.

The uncertainty of the aerodynamic loads can then be determined from

$$U_{X_{i_h}}^2 = U_{\overline{X}_{R_{\text{int}_{i_h}}}}^2 + U_{\overline{X}_{T_{\text{int}_{i_h}}}}^2 - 2B_{\overline{X}_{R_{\text{int}_{i_h}}}\overline{X}_{T_{\text{int}_{i_h}}}} \tag{7.20}$$

where

$$U_{\overline{X}_{R_{\text{int}_{i_h}}}}^2 \cong B_{[X_{R_i}]}^2 + (2S_{\overline{X}_{R_{\text{int}_{i_h}}}})^2 \tag{7.21}$$

$$U_{\overline{X}_{T_{\text{int}_{i_h}}}}^2 \cong B_{[X_{T_i}]}^2 + (2S_{\overline{X}_{T_{\text{int}_{i_h}}}})^2 \tag{7.22}$$

$$B_{\overline{X}_{R_{\text{int}_{i_h}}}\overline{X}_{R_{\text{int}_{i_h}}}} \cong B_{[X_{R_i}][X_{T_i}]} = B_{[X_{R_i}]}B_{[X_{T_i}]} \tag{7.23}$$

Equation (7.20) simplifies to

$$U_{X_{i_h}}^2 \cong (2S_{\overline{X}_{R_{\text{int}_{i_h}}}})^2 + (2S_{\overline{X}_{T_{\text{int}_{i_h}}}})^2 \tag{7.24}$$

as $B_{[X_{R_i}]} = B_{[X_{T_i}]}$. It is important to note the systematic uncertainty of the aerodynamic loads cancels out, in part due to the assumptions that were made for interpolation and averaging of the cycles, but by in large the cancellation occurs because the estimates of the balance accuracy are constant for both the run and the tare. Had a variable estimate of the balance accuracy, based on

load, been available the same assumptions for interpolation and averaging would apply and there would be a systematic contribution to the uncertainty estimate.

The uncertainty of the body-axis aerodynamic coefficients for the averaged interpolated cycle is similar to Eq. (6.22) in that

$$U^2_{C_{X_{i_h}}} = \left(\frac{1}{\bar{q}K_i}\right)^2 U^2_{X_{i_h}} + \left(\frac{C_{X_{i_h}}}{\bar{q}}\right)^2 U^2_{\bar{q}} \tag{7.25}$$

where

$$U^2_{\bar{q}} = B^2_{\bar{q}} + (2S_{\bar{q}})^2 \tag{7.26}$$

7-4 Dynamic test results of fighter model

Forced oscillation tests typically sample data at 200 Hz for 40 consecutive sinusoidal cycles for a given angle-of-attack as discussed earlier. The same 100 Hz anti-aliasing filters, as with the static tests, are used for all forced oscillation tests where time-histories are recorded. Typically the position and corrected balance loads are then digitally low-pass filtered at 4 Hz before the cycles are interpolated and averaged.

A few runs and tares were made that sampled data for 120 continuous cycles at selected α's. α refers to the angle-of-attack where the cycle position for a yaw oscillation about the *z*-axis, $\theta_z = 0$. The actual angle-of-attack and sideslip angles can be found from

$$\tan(\alpha) = \sec(\theta_z)\tan(\theta_y) \tag{7.27}$$

$$\sin(\beta) = -\sin(\theta_z)\cos(\theta_y) \tag{7.28}$$

where θ_y is equivalent the turntable angle. The extended cycle count was selected to observe how the variation of the cycles changed over time. Each α was selected based on the variation in the aerodynamic loads over the angle-of-attack range of previous forced oscillation runs. The α's chosen for the fighter model were 10, 38, 40, 50 and 60 degrees. The amplitude of the oscillations was ±5 degrees.

The information removed by the 4 Hz filter for a top-mounted yaw oscillation configuration (figure 3.3c) at 40º angle-of-attack can be seen in figures 7.1 through 7.6. The spectrums are again mean-zero and generated as described in section 6-4.2 . The frequency of oscillation for the data shown is 0.5 Hz and is denoted with a green circle. Note the relative magnitude of frequencies filtered out to that of the oscillation frequency particularly in normal force, pitching moment, yawing moment and side force (figures 7.1, 7.3, 7.5 and 7.6 respectively) where the magnitude of the structural vibration around 5 Hz is greater than that of the response at the oscillation frequency. The rolling moment response is slightly higher than the structural noise (figure 7.4). Axial force has a 20 dB higher response than all other frequencies in that channel for this condition. Also, note the second harmonic in side force that is not filtered out (figure 6.6).

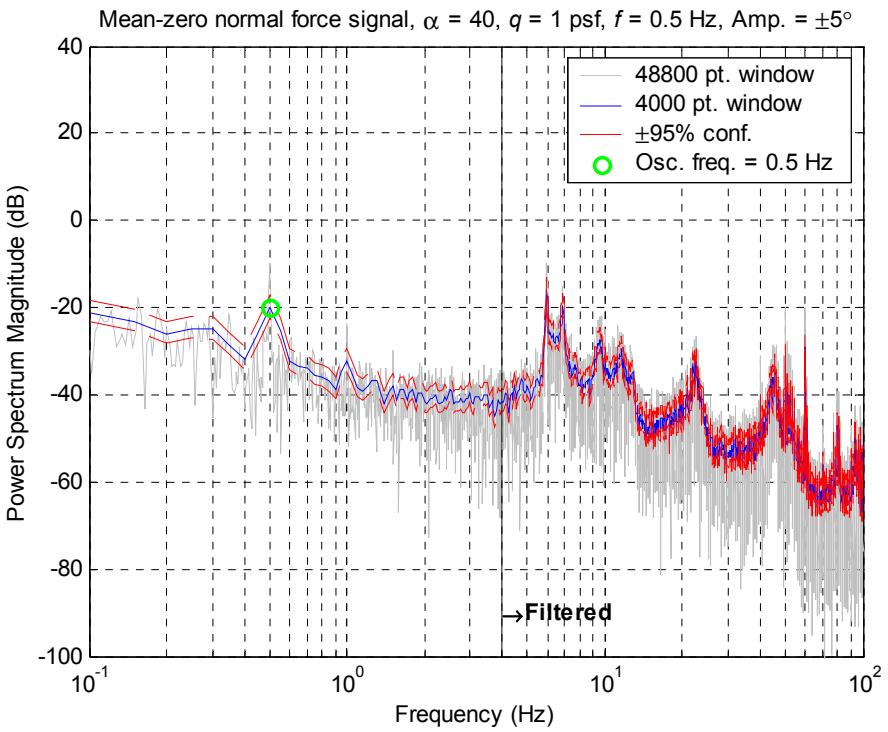

Figure 7.1 Power spectrum of mean zero corrected normal force.

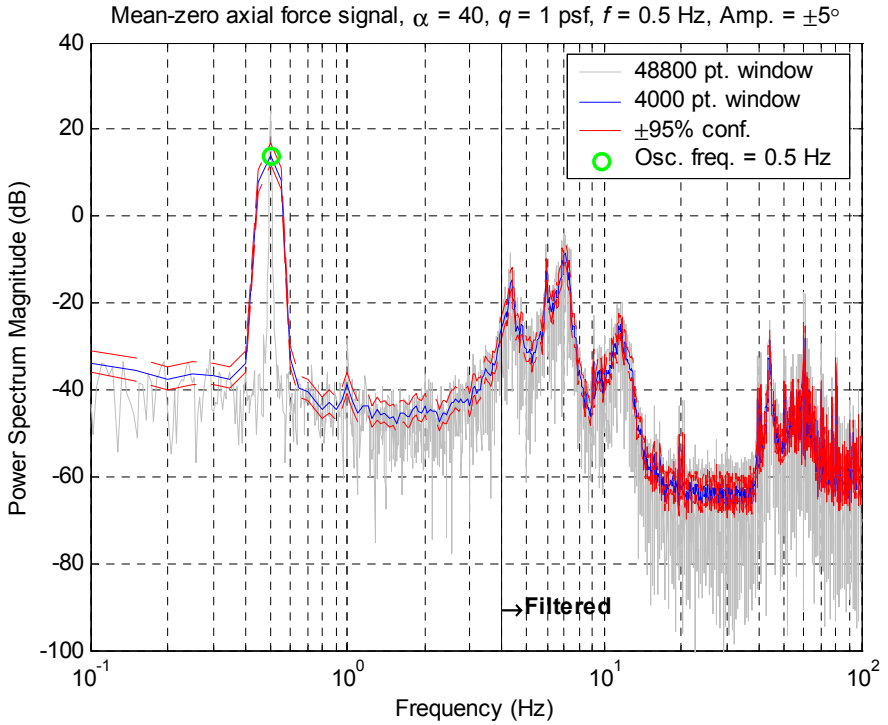

Figure 7.2 Power spectrum of mean zero corrected axial force.

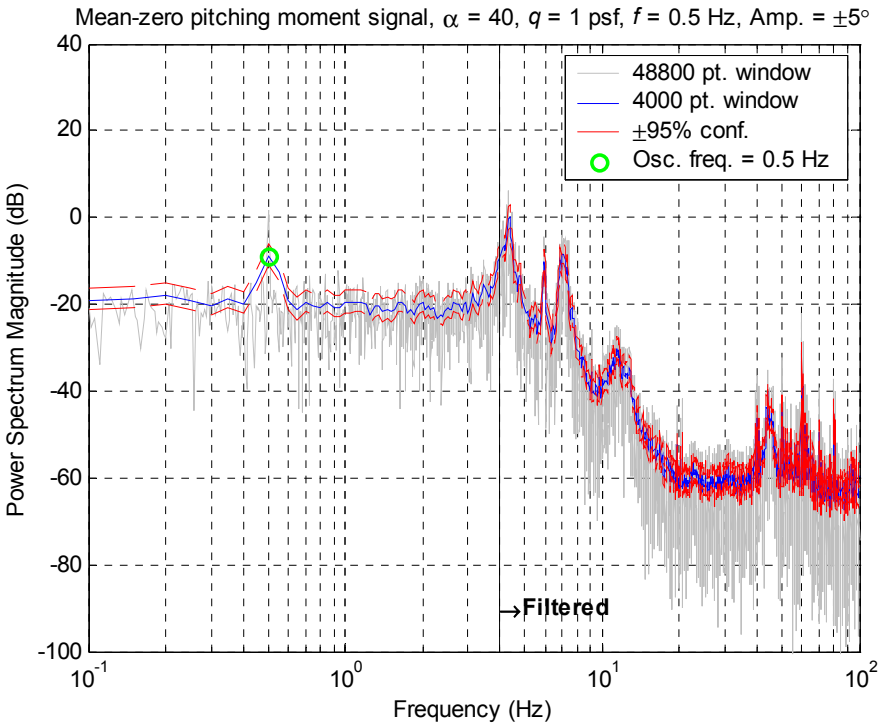

Figure 7.3 Power spectrum of mean zero corrected pitching moment.

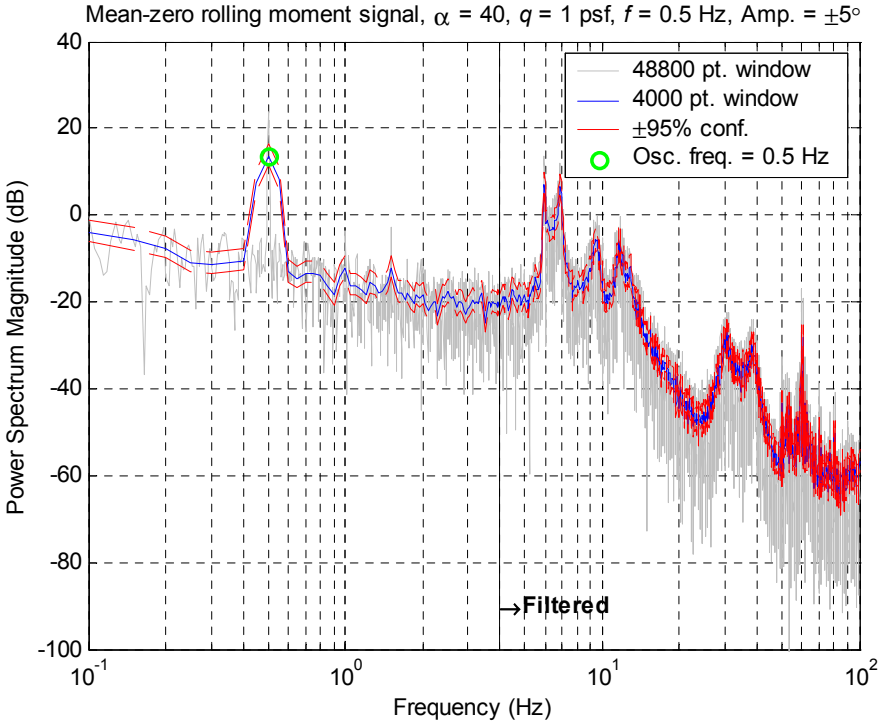

Figure 7.4 Power spectrum of mean zero corrected rolling moment.

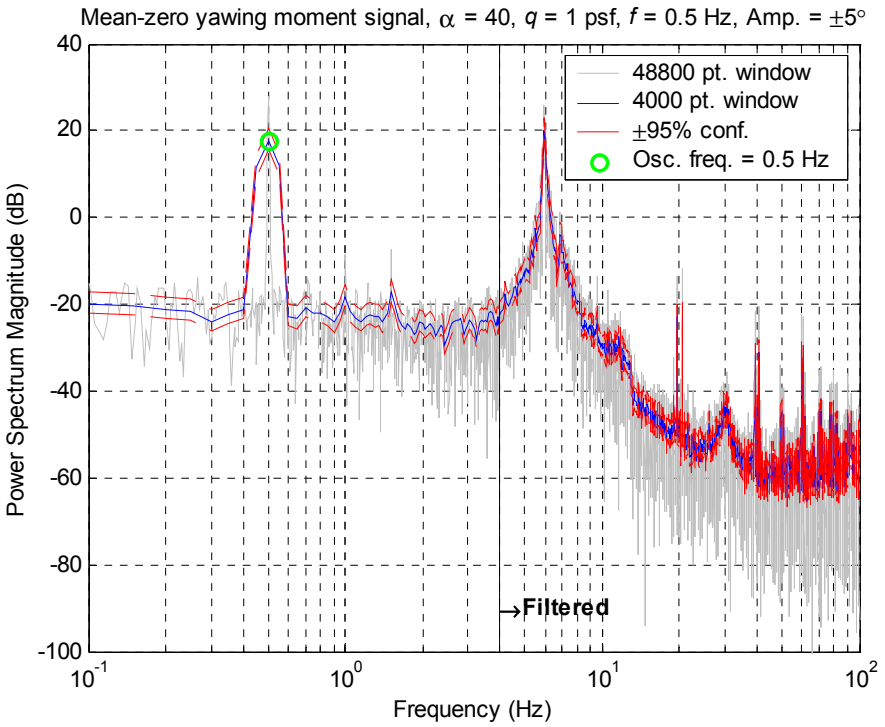

Figure 7.5 Power spectrum of mean zero corrected yawing moment.

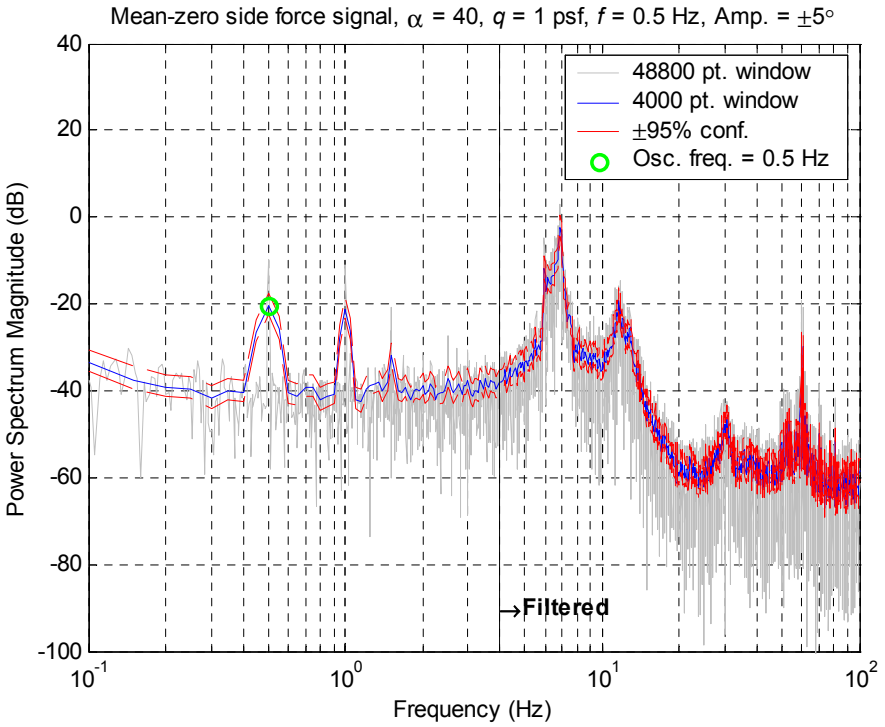

Figure 7.6 Power spectrum of mean zero corrected side force. Note the magnitude of the first harmonic

As with the static test, low α's typically have low uncertainties. The unsteady aerodynamics usually then increase to a maximum around stall and then decrease post-stall. The total uncertainty after 120 oscillations is shown in figures 7.7 through 7.36. Coefficient data for all 120 interpolated continuous cycles, their mean and their bias are shown. Note the largest contribution to the total uncertainty for each balance component, except normal force, is due to the inherent unsteady aerodynamics and structural vibrations that were not filtered out. To understand the large bias in normal force let us return to Eq. (7.25). The dynamic pressure for the run shown was 0.95 psf. Recall the bias from interpolation and averaging the forces was considered negligible and was neglected. Thus only the bias from the dynamic pressure is included in the uncertainty estimates. Equation (7.25) shows that when $q < 1$ and $C_x > 1$ the uncertainty from the dynamic pressure is magnified into C_x.

Equations (7.27) and (7.28) show the angle-of-attack and the sideslip angle increase with $|\theta_z|$ for a yaw oscillation. The maximum change in α for a ±5º amplitude oscillation is less than 0.11º (occurs at $\theta_y = 45°$ and $\theta_z = \pm 5°$). The maximum change in sideslip is always the amplitude, which occurs at $\theta_y = 0°$. The changes in states for this run are small. This is evident in the longitudinal coefficients as neither normal force, axial force nor pitching moment exhibit much change over the cycles or hysteresis loops. The angle-of-attack is nearly constant over the cycle so any slope in the hysteresis loops indicates a relationship with sideslip. Figure 7.21 has a peculiar asymmetry. Post-test inspection revealed that one leading edge of the fighter model wing was sharper than the other – apparently due to some previous model repair. This may be a factor in the asymmetries seen in the hysteresis loops.

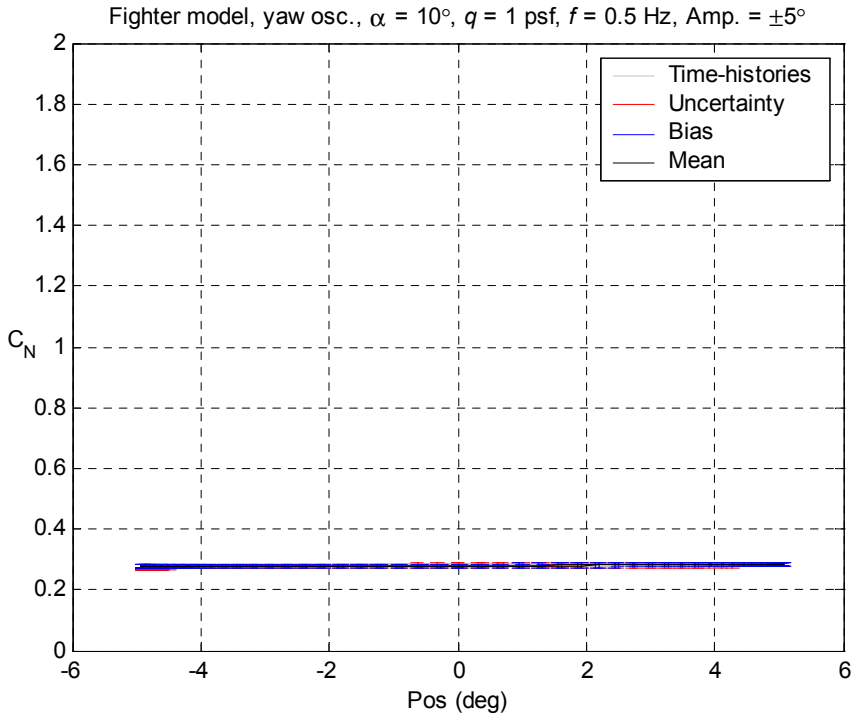

Figure 7.7 Time-history of 120 cycles oscillated at 0.5 Hz and uncertainty of 100 interpolated points around the mean cycle for normal force coefficient.

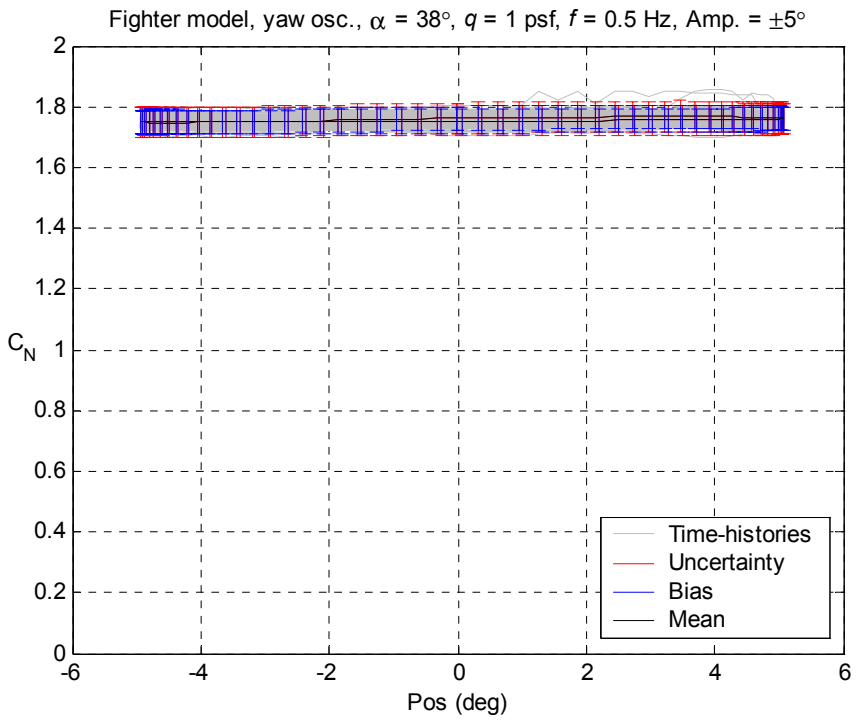

Figure 7.8 Time-history of 120 cycles oscillated at 0.5 Hz and uncertainty of 100 interpolated points around the mean cycle for normal force coefficient.

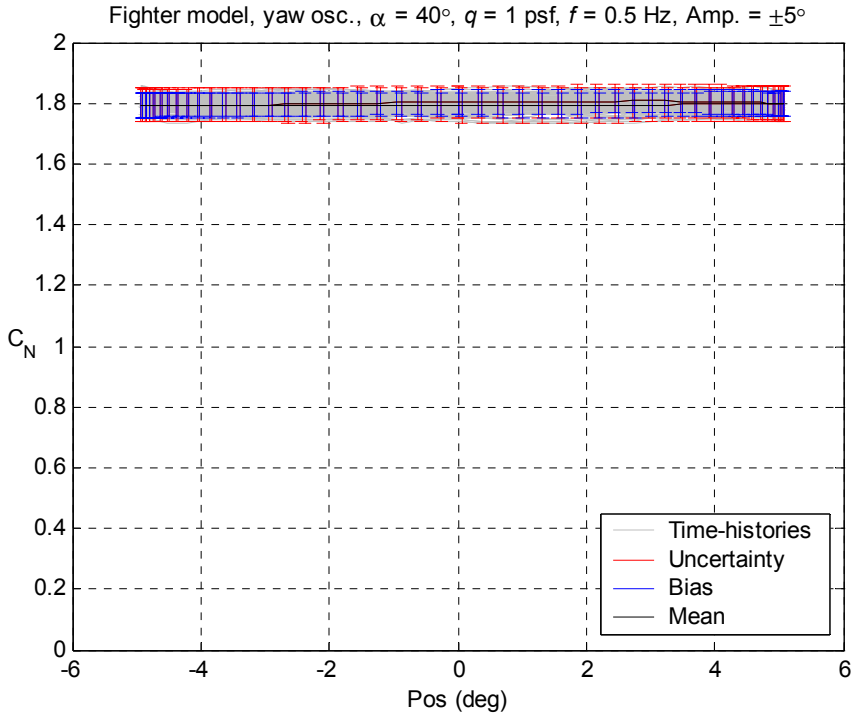

Figure 7.9 Time-history of 120 cycles oscillated at 0.5 Hz and uncertainty of 100 interpolated points around the mean cycle for normal force coefficient.

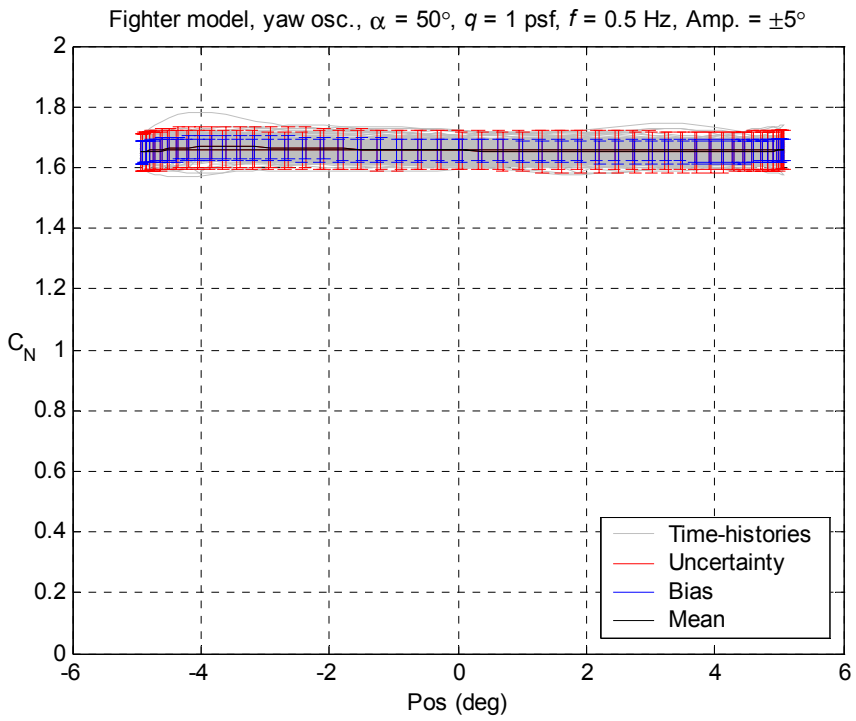

Figure 7.10 Time-history of 120 cycles oscillated at 0.5 Hz and uncertainty of 100 interpolated points around the mean cycle for normal force coefficient.

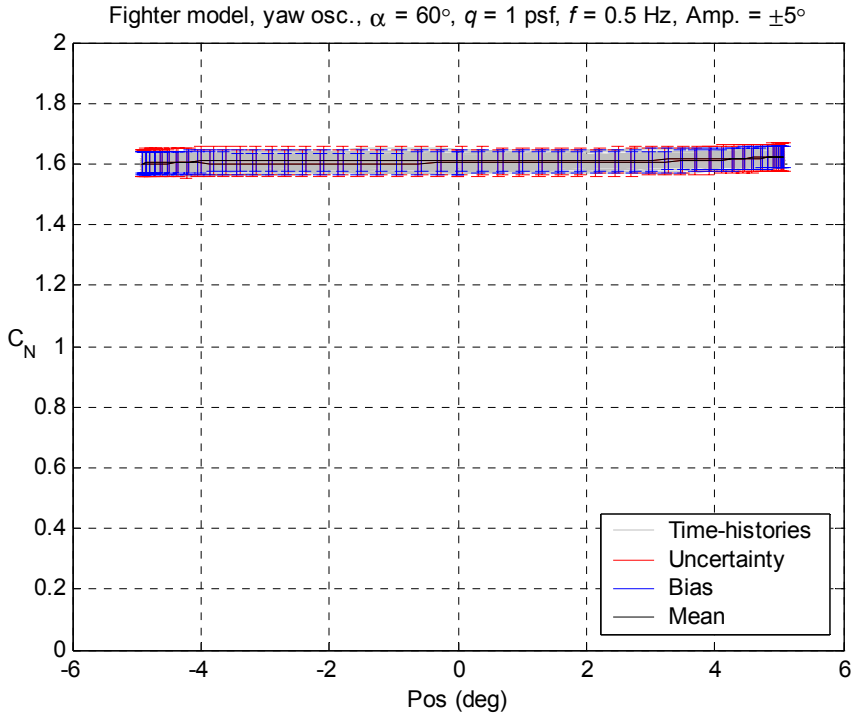

Figure 7.11 Time-history of 120 cycles oscillated at 0.5 Hz and uncertainty of 100 interpolated points around the mean cycle for normal force coefficient.

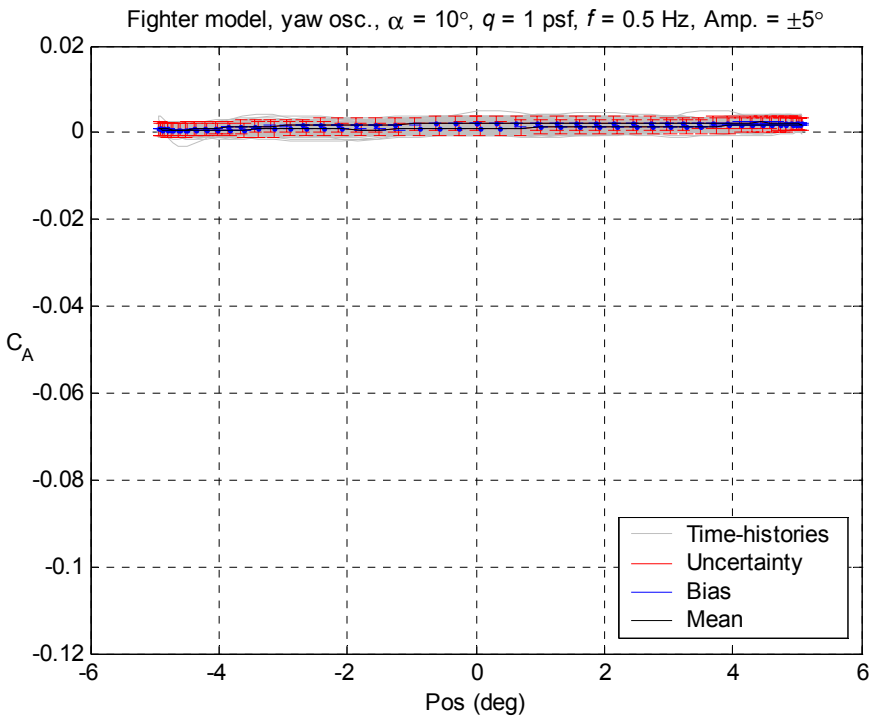

Figure 7.12 Time-history of 120 cycles oscillated at 0.5 Hz and uncertainty of 100 interpolated points around the mean cycle for axial force coefficient.

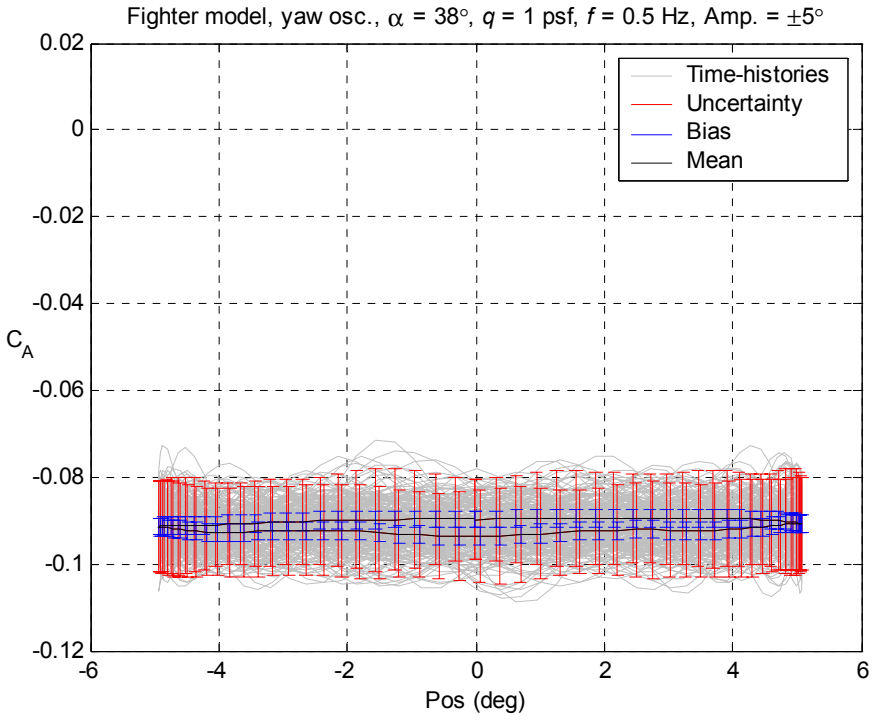

Figure 7.13 Time-history of 120 cycles oscillated at 0.5 Hz and uncertainty of 100 interpolated points around the mean cycle for axial force coefficient.

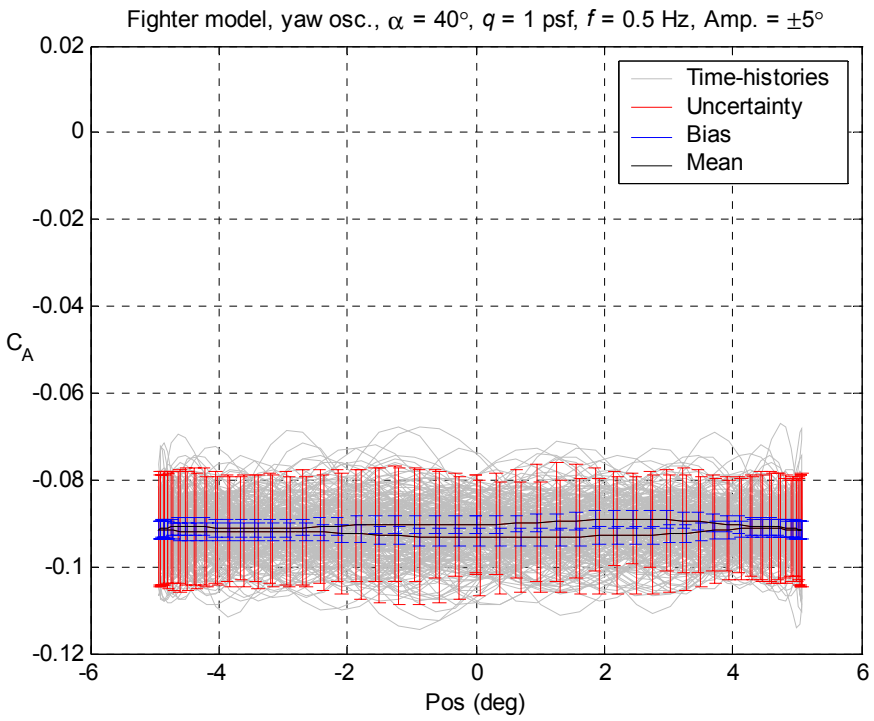

Figure 7.14 Time-history of 120 cycles oscillated at 0.5 Hz and uncertainty of 100 interpolated points around the mean cycle for axial force coefficient.

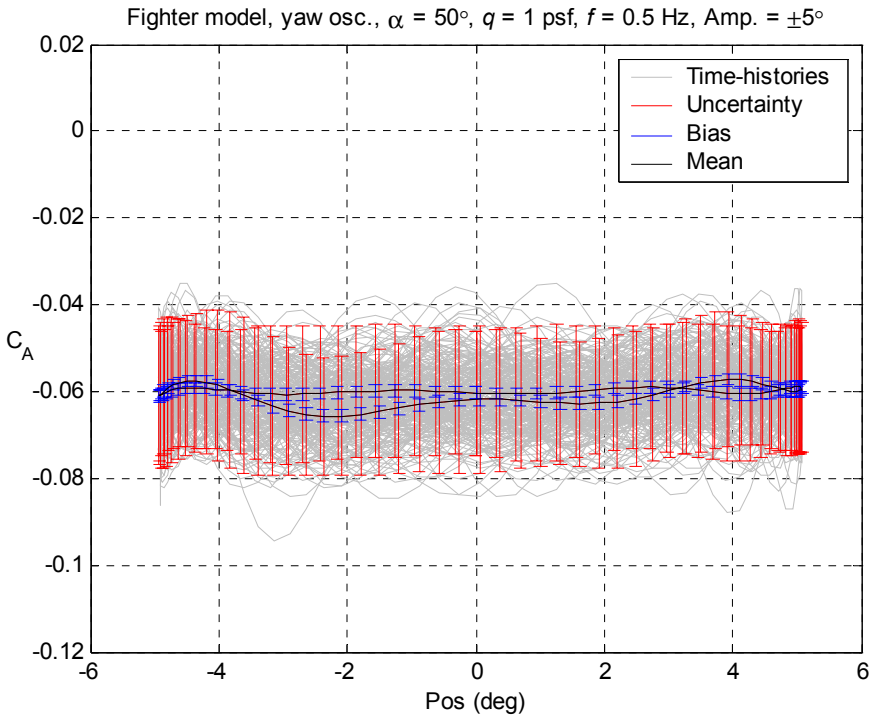

Figure 7.15 Time-history of 120 cycles oscillated at 0.5 Hz and uncertainty of 100 interpolated points around the mean cycle for axial force coefficient.

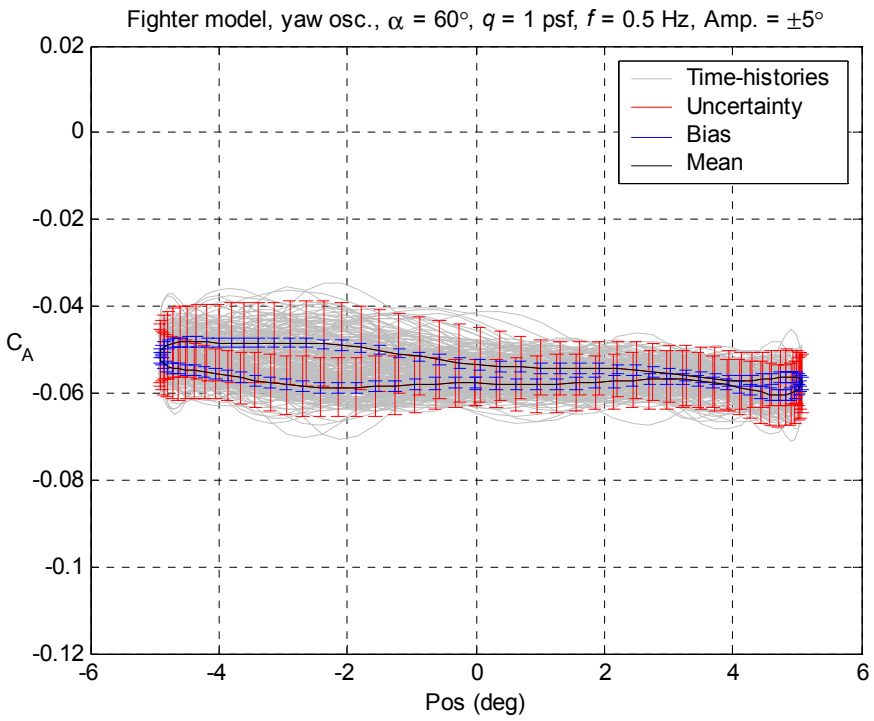

Figure 7.16 Time-history of 120 cycles oscillated at 0.5 Hz and uncertainty of 100 interpolated points around the mean cycle for axial force coefficient.

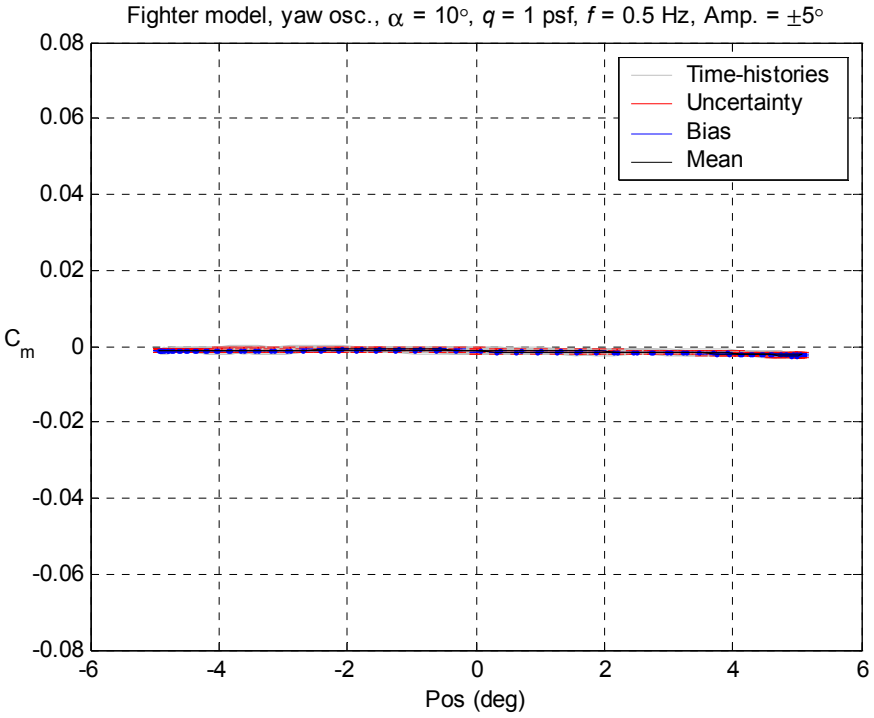

Figure 7.17 Time-history of 120 cycles oscillated at 0.5 Hz and uncertainty of 100 interpolated points around the mean cycle for pitching moment coefficient.

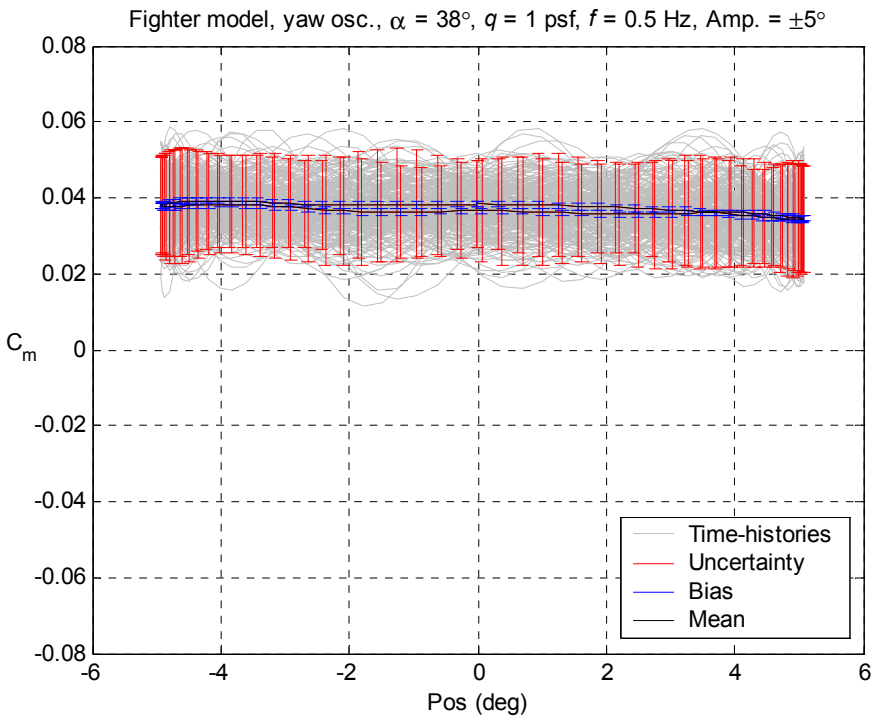

Figure 7.18 Time-history of 120 cycles oscillated at 0.5 Hz and uncertainty of 100 interpolated points around the mean cycle for pitching moment coefficient.

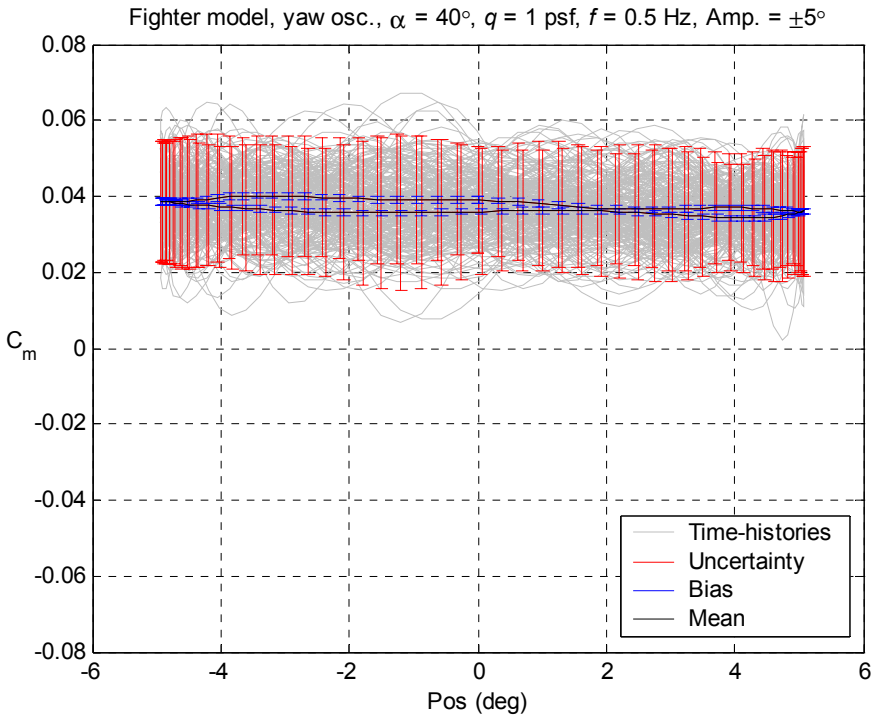

Figure 7.19 Time-history of 120 cycles oscillated at 0.5 Hz and uncertainty of 100 interpolated points around the mean cycle for pitching moment coefficient.

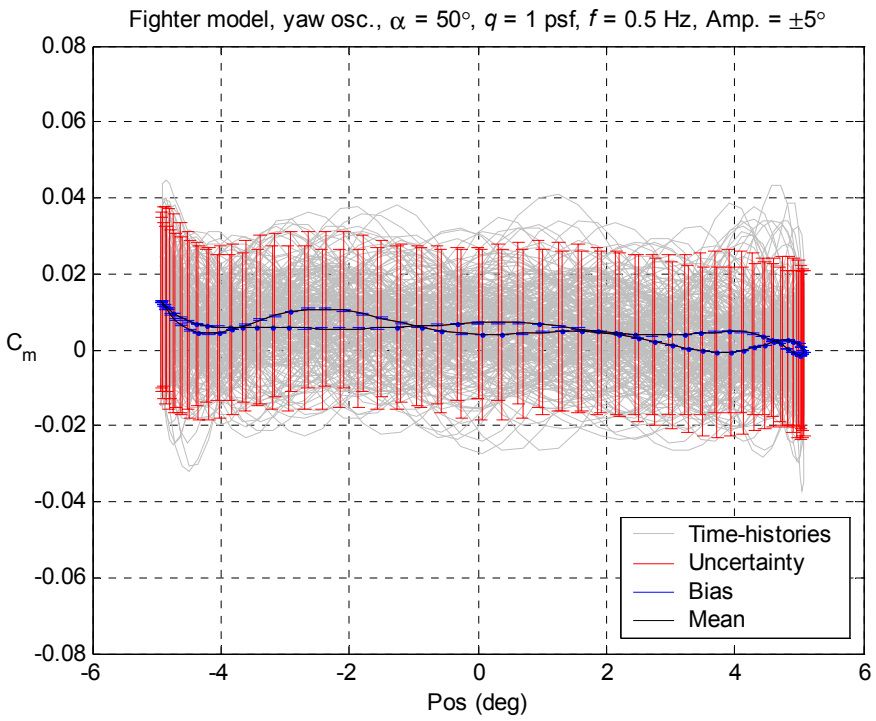

Figure 7.20 Time-history of 120 cycles oscillated at 0.5 Hz and uncertainty of 100 interpolated points around the mean cycle for pitching moment coefficient.

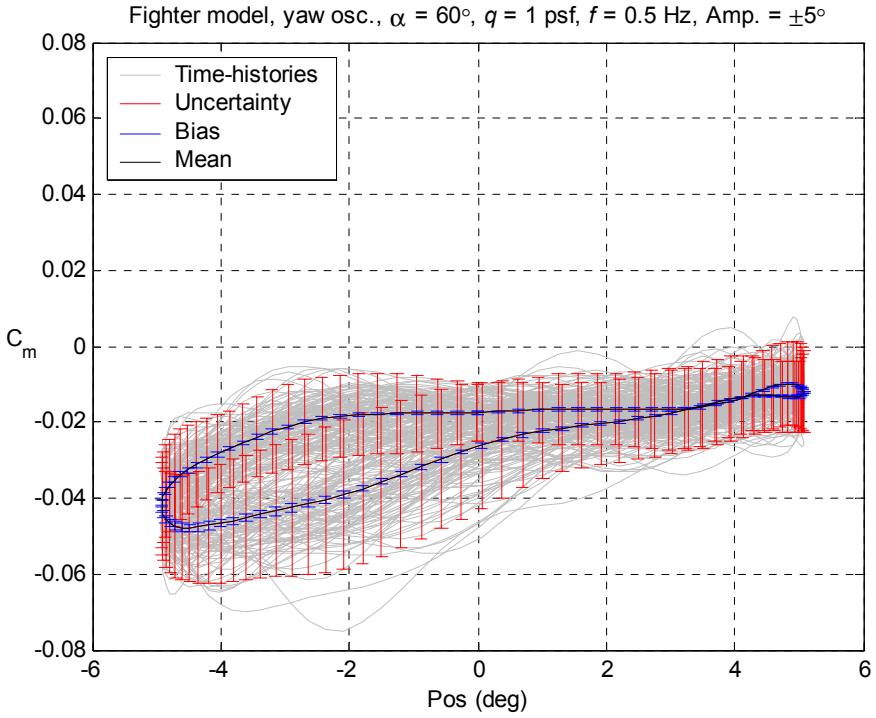

Figure 7.21 Time-history of 120 cycles oscillated at 0.5 Hz and uncertainty of 100 interpolated points around the mean cycle for pitching moment coefficient.

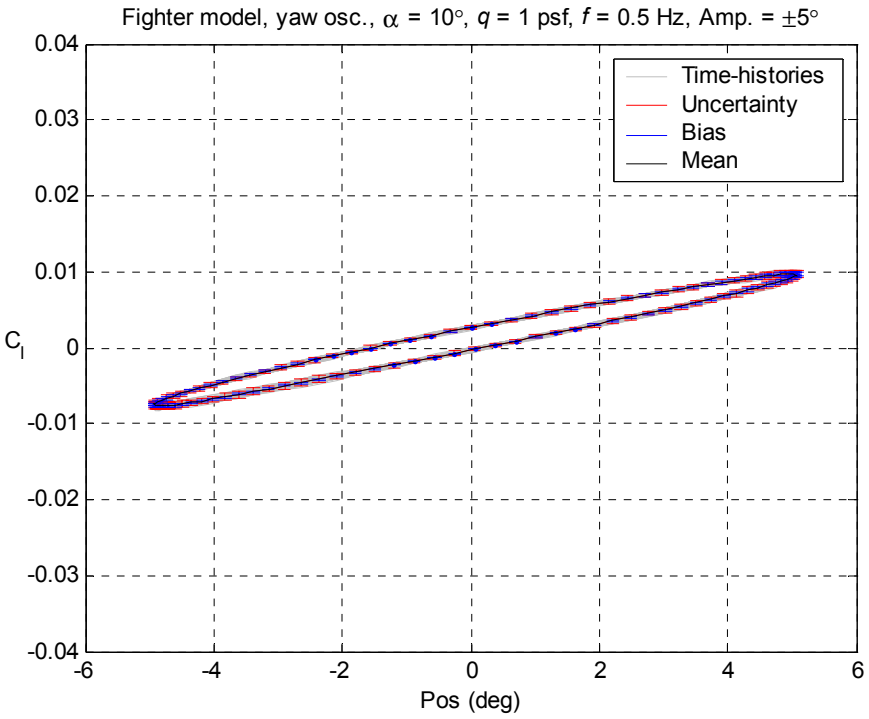

Figure 7.22 Time-history of 120 cycles oscillated at 0.5 Hz and uncertainty of 100 interpolated points around the mean cycle for rolling moment coefficient.

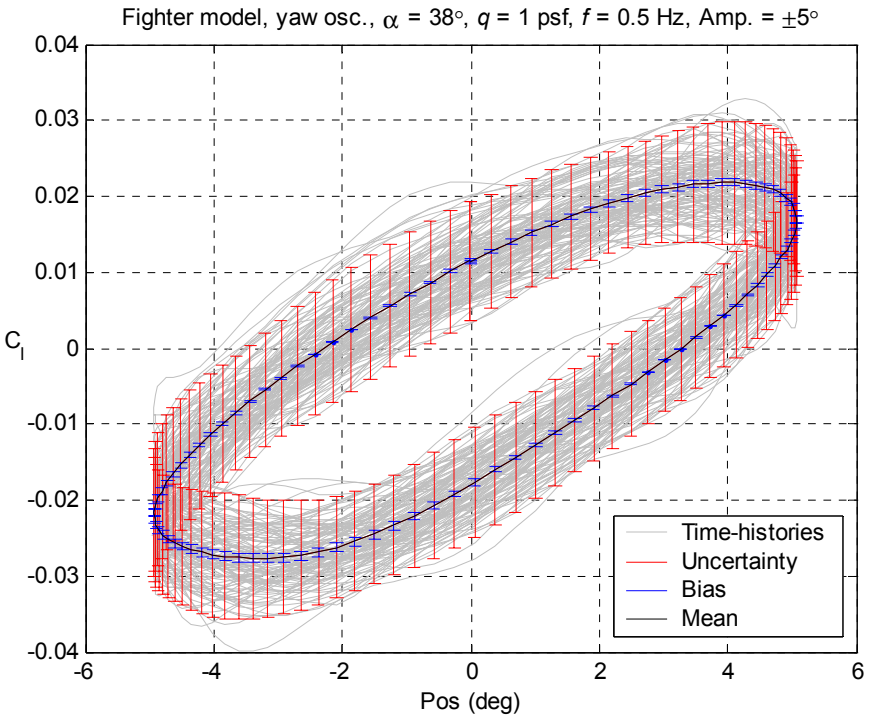

Figure 7.23 Time-history of 120 cycles oscillated at 0.5 Hz and uncertainty of 100 interpolated points around the mean cycle for rolling moment coefficient.

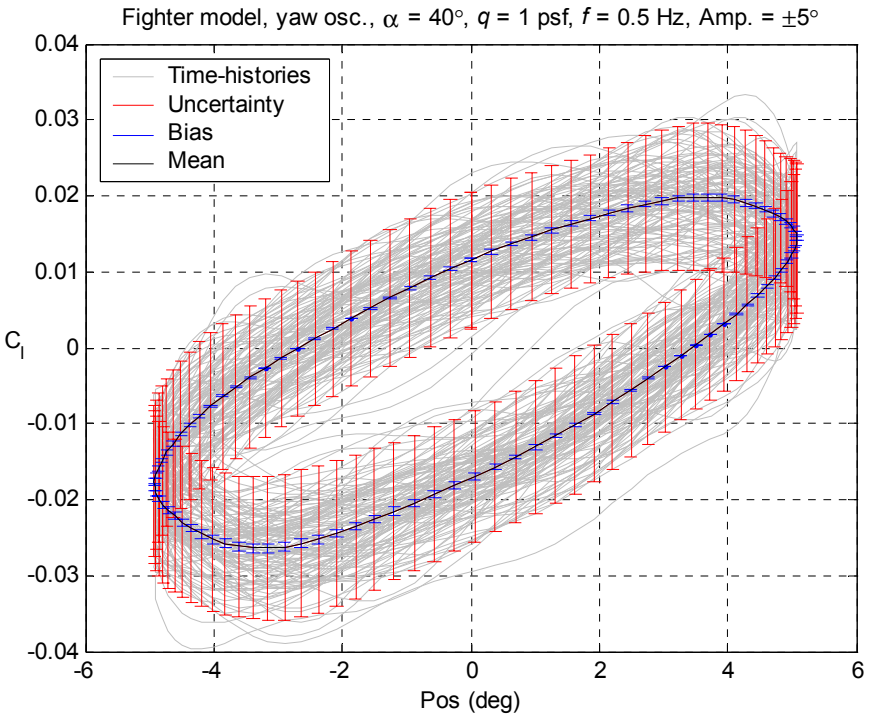

Figure 7.24 Time-history of 120 cycles oscillated at 0.5 Hz and uncertainty of 100 interpolated points around the mean cycle for rolling moment coefficient.

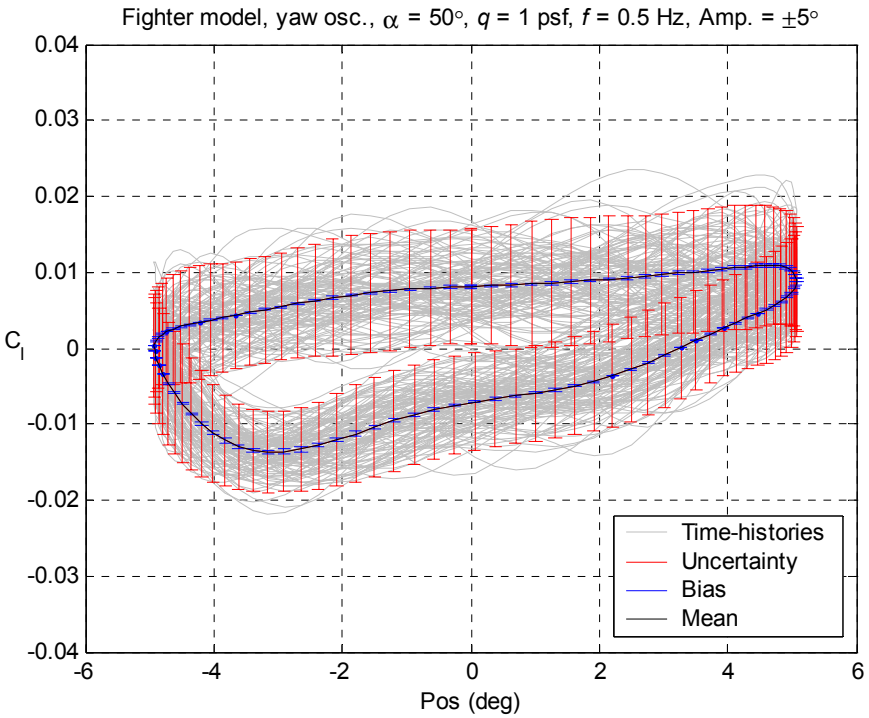

Figure 7.25 Time-history of 120 cycles oscillated at 0.5 Hz and uncertainty of 100 interpolated points around the mean cycle for rolling moment coefficient.

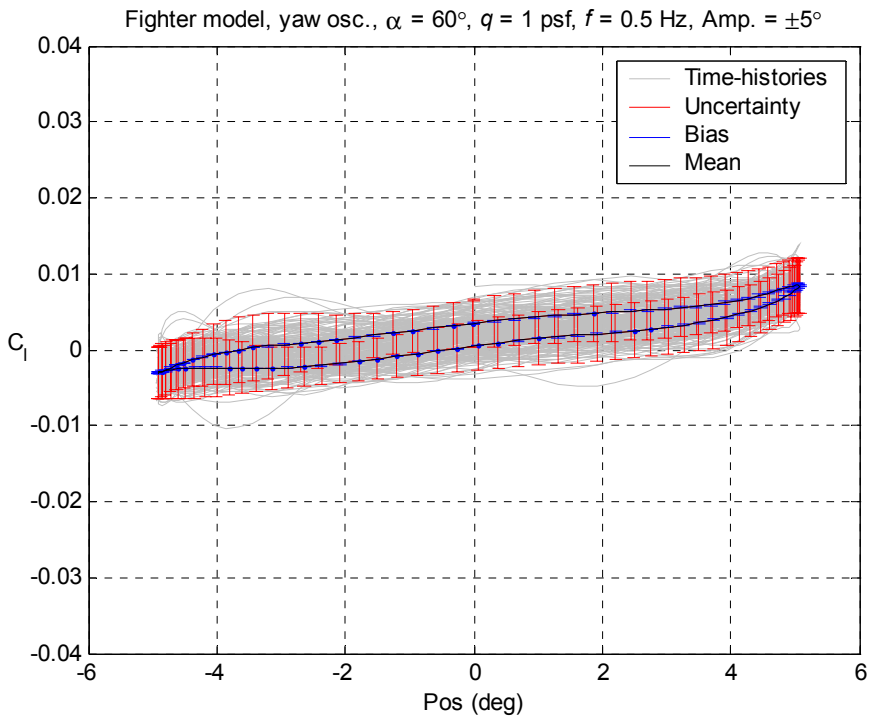

Figure 7.26 Time-history of 120 cycles oscillated at 0.5 Hz and uncertainty of 100 interpolated points around the mean cycle for rolling moment coefficient.

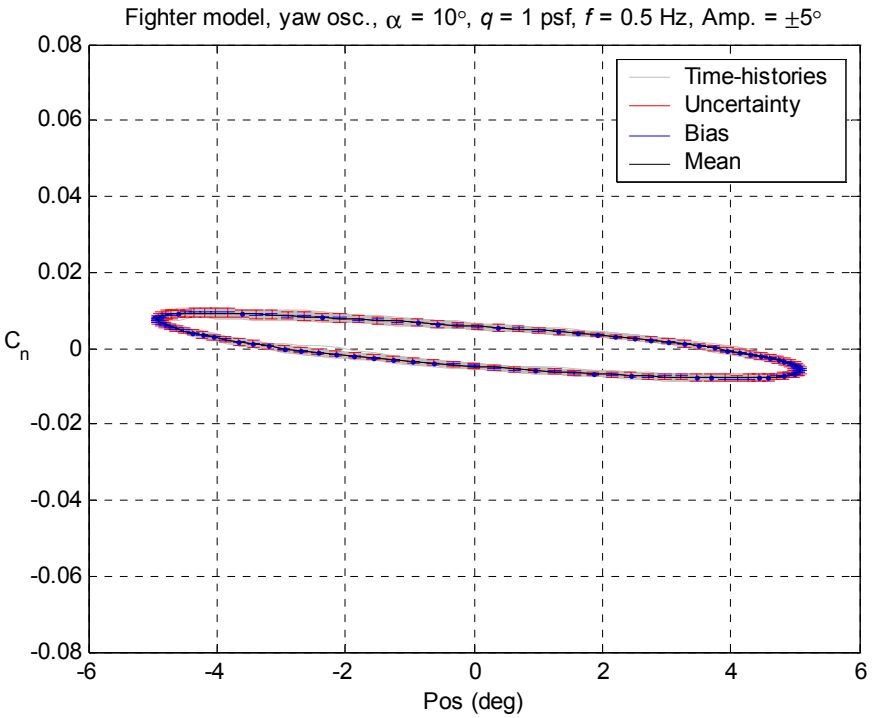

Figure 7.27 Time-history of 120 cycles oscillated at 0.5 Hz and uncertainty of 100 interpolated points around the mean cycle for yawing moment coefficient.

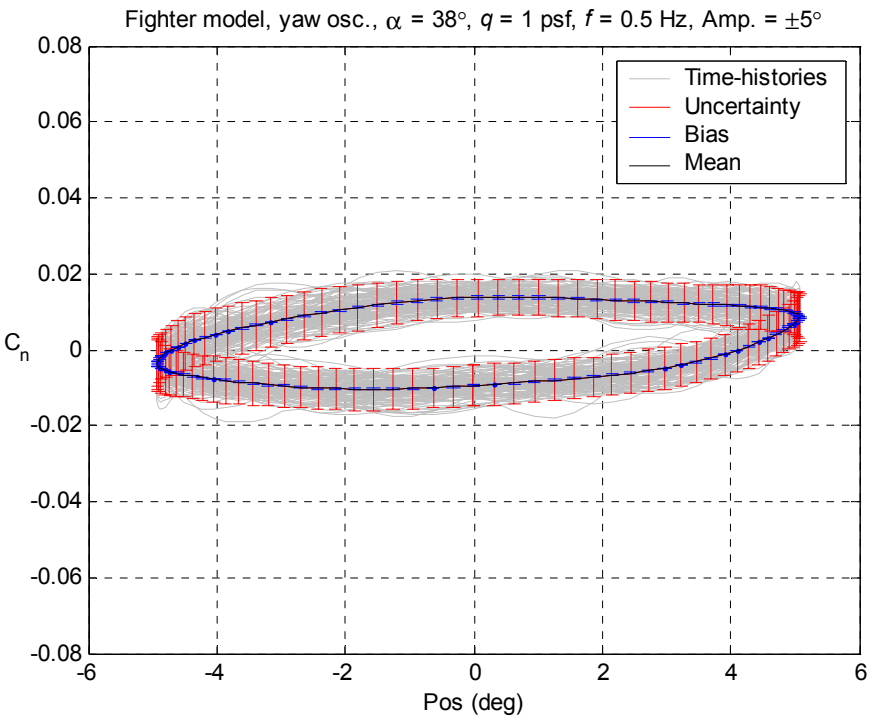

Figure 7.28 Time-history of 120 cycles oscillated at 0.5 Hz and uncertainty of 100 interpolated points around the mean cycle for yawing moment coefficient.

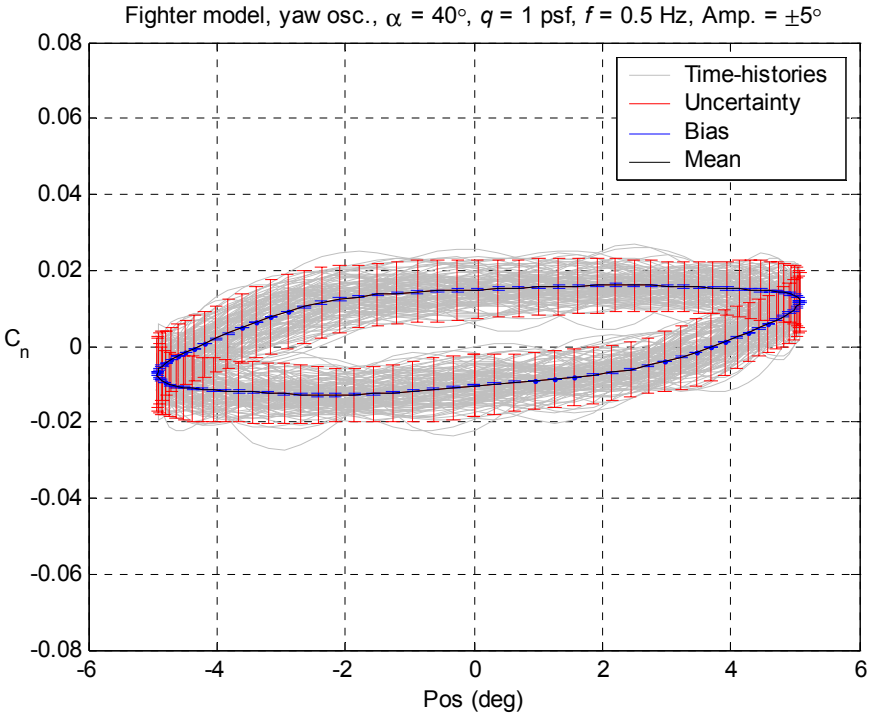

Figure 7.29 Time-history of 120 cycles oscillated at 0.5 Hz and uncertainty of 100 interpolated points around the mean cycle for yawing moment coefficient.

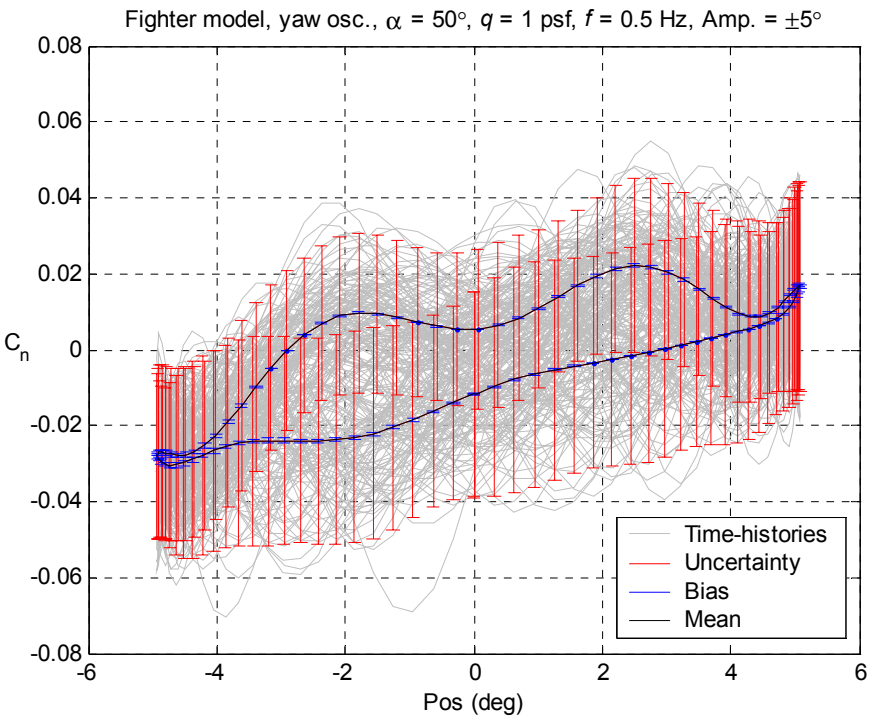

Figure 7.30 Time-history of 120 cycles oscillated at 0.5 Hz and uncertainty of 100 interpolated points around the mean cycle for yawing moment coefficient.

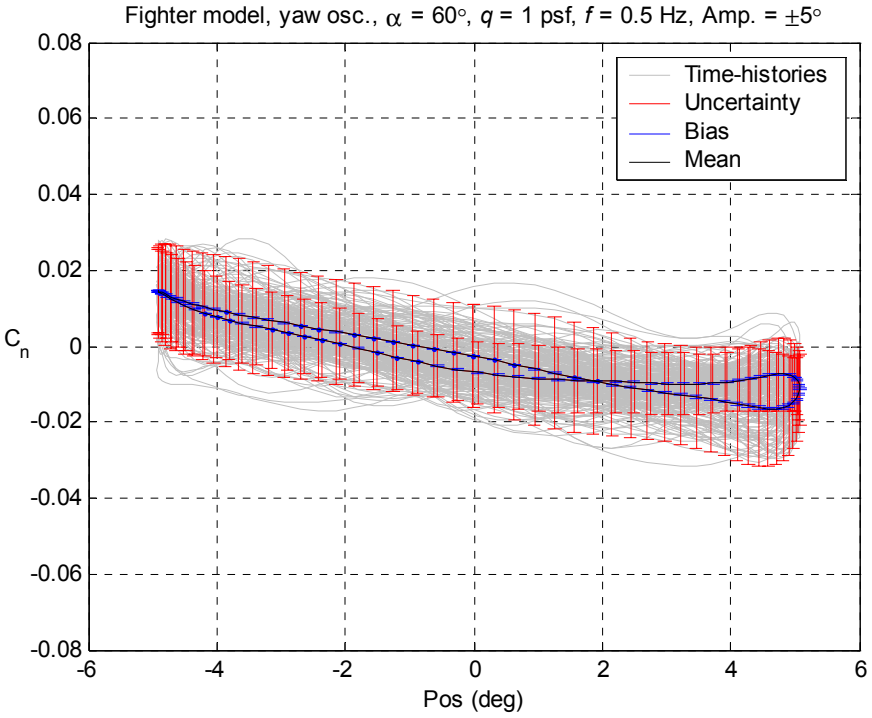

Figure 7.31 Time-history of 120 cycles oscillated at 0.5 Hz and uncertainty of 100 interpolated points around the mean cycle for yawing moment coefficient.

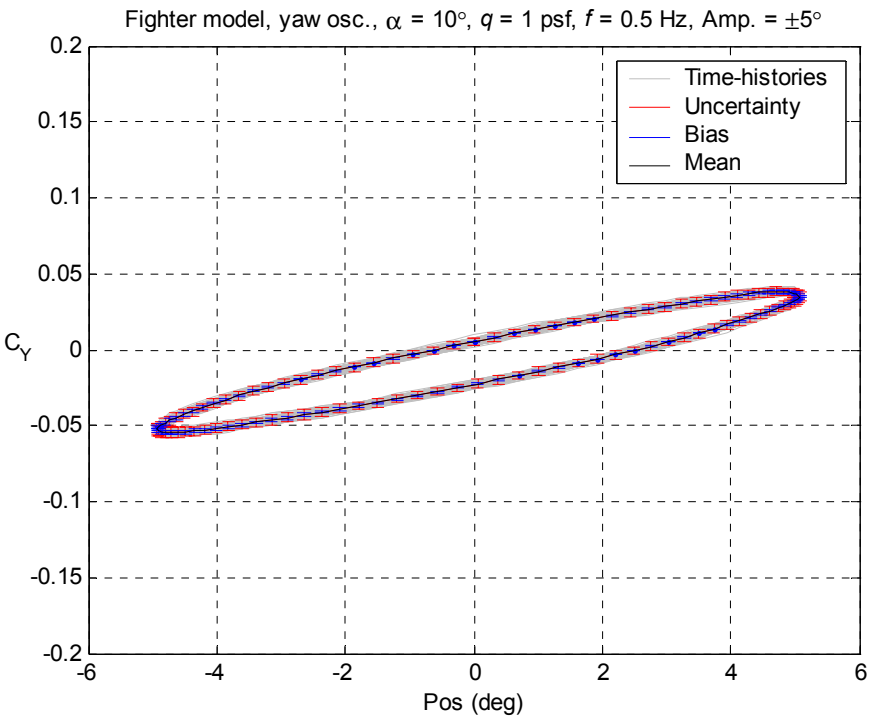

Figure 7.32 Time-history of 120 cycles oscillated at 0.5 Hz and uncertainty of 100 interpolated points around the mean cycle for side force coefficient.

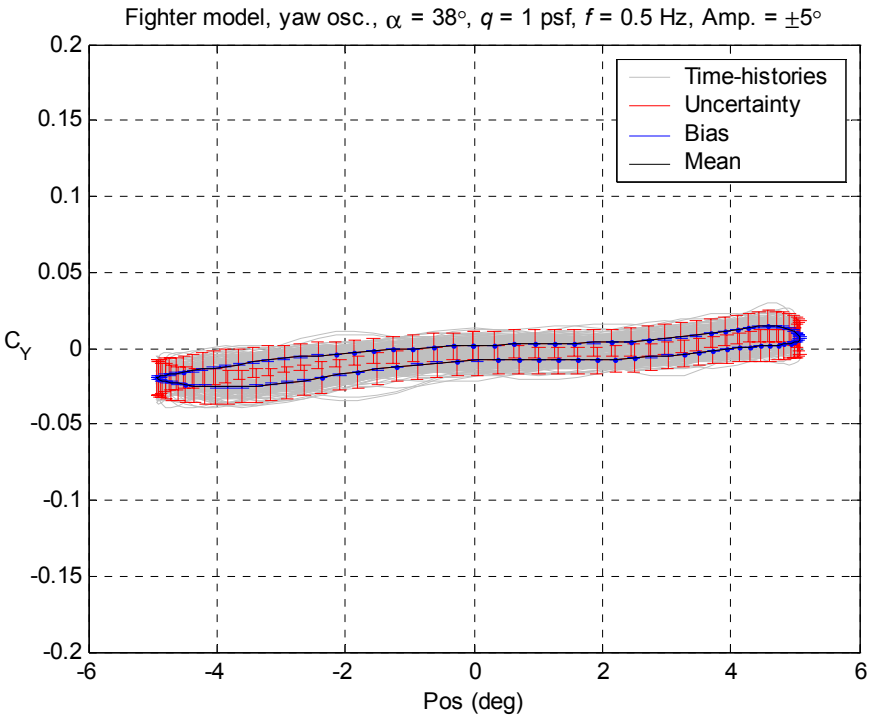

Figure 7.33 Time-history of 120 cycles oscillated at 0.5 Hz and uncertainty of 100 interpolated points around the mean cycle for side force coefficient.

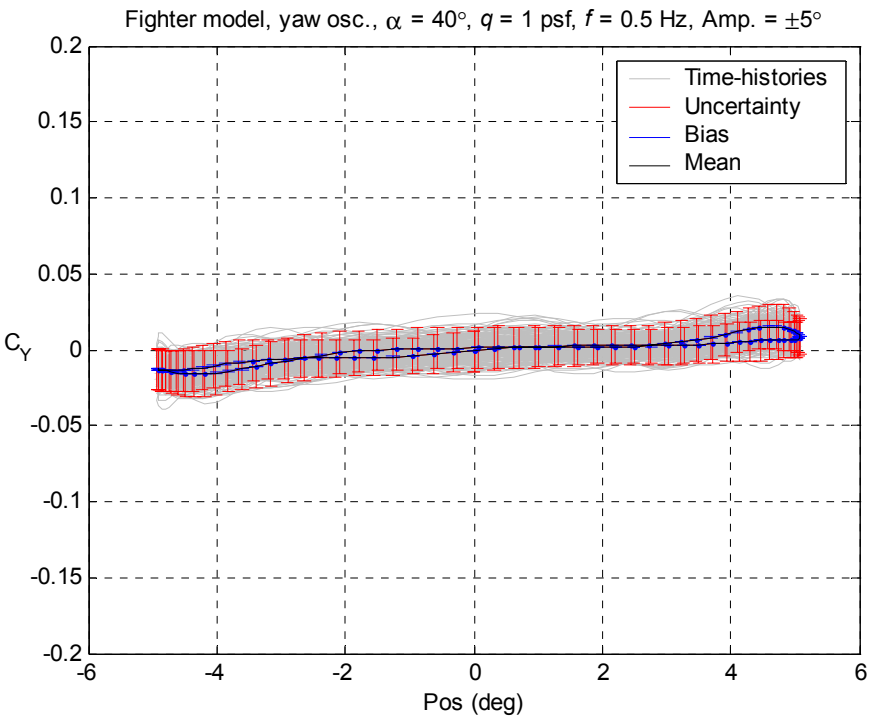

Figure 7.34 Time-history of 120 cycles oscillated at 0.5 Hz and uncertainty of 100 interpolated points around the mean cycle for side force coefficient.

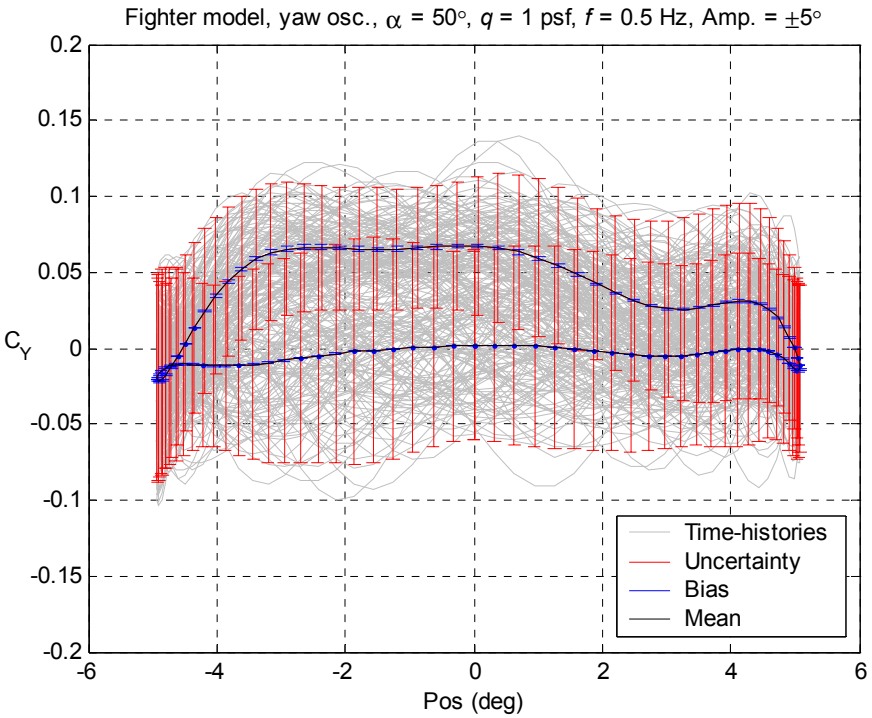

Figure 7.35 Time-history of 120 cycles oscillated at 0.5 Hz and uncertainty of 100 interpolated points around the mean cycle for side force coefficient.

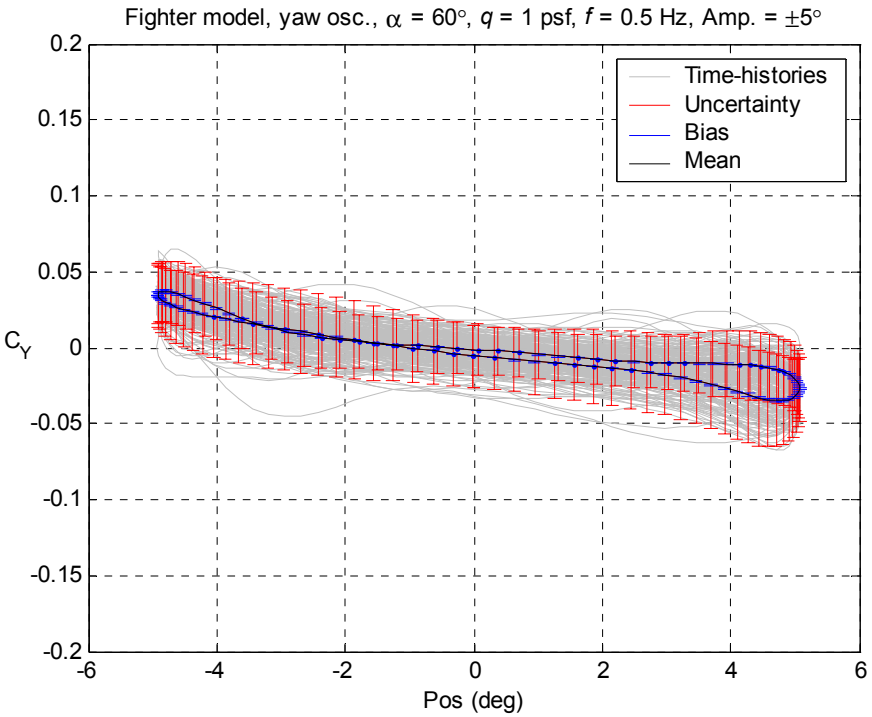

Figure 7.36 Time-history of 120 cycles oscillated at 0.5 Hz and uncertainty of 100 interpolated points around the mean cycle for side force coefficient.

The difference between the values of the yawing moment at positive and negative yaw rates at $\theta_z = 0°$ indicate the magnitude of yaw damping, and the direction of the loops - while not shown on the figures - indicate the sign of the yaw rate damping. The sign of the yaw rate damping can often change with sideslip as shown by the twist in figure 7.31. Side force has a similar trend. The slope of the hysteresis loops can change often change with α. Figure 7.27 shows a stable positive C_{l_β} at α = 10º, a negative unstable C_{l_β} at 38º, 40º and 50º and finally a stable positive C_{l_β} at α = 60º. The uncertainty estimates show how much variation there is in the data from cycle to cycle. They provide valuable insight to the shapes of strange average cycles such as in figures 7.30 and 7.35 that would otherwise not be available.

7-5 Dynamic test results of Generic Civil Transport model

Forced oscillation tests were conducted on the Generic Civil Transport. Due to proprietary concerns the magnitude of the results cannot be shown. However the scales for each individual coefficient are constant. One roll oscillation run (similar to figure 3.3b) was sampled for 120 cycles at selected α's just as with the fighter model. Again, α in this context is the angle-of-attack at $\theta = 0$ or in this case $\theta_x = 0$. The angle-of-attack actually changes throughout the oscillation. The α's chosen were 4, 16, 26, and 50 degrees. The model was oscillated at 0.92 Hz with an amplitude of ±20 degrees. The total uncertainty after 120 oscillations is shown in figures 7.37 through 7.60. All 120 interpolated continuous cycles, the mean cycle and the bias are also shown in gray. The actual angle-of-attack and sideslip angles, which occur during the cycles, can be found from

$$\tan(\alpha) = \cos(\theta_x)\tan(\theta_y) \tag{7.29}$$

$$\sin(\beta) = \sin(\theta_x)\sin(\theta_y) \tag{7.30}$$

The bias is far less for the GCT than with the fighter because of the larger dynamic pressure of 10 psf. Equation (7.25) shows the uncertainty is inversely proportional to q. It would thus seem testing at a higher dynamic pressure would solve all uncertainty woes. Recall the uncertainty is a combination of unsteady aerodynamics, structural dynamics, unsteady free stream, electrical noise, etc. There are no guarantees testing at a higher dynamic pressure would not induce larger structural noise in the data. Recall, this was in fact the case with the fighter model discussed in chapter 3.

The higher amplitude of this run results in larger variations of states across the cycle, which contributes to data showing cleaner trends than seen with the small amplitude fighter data. The angle-of-attack, as seen from Eq. (7.29) has a period twice that if the oscillation frequency. This produces a "bend" in the hysteresis loops of longitudinal coefficients as seen in figures 7.37 through 7.48. The "twists" in longitudinal coefficients such as in figure 7.39 are caused by the time lag of the flow [7] as the model roll rate changes directions. The slopes of the hysteresis loops indicate the aerodynamic response with a change in sideslip. The direction of the loops and the delta in the loops between positive and negative roll rates at Pos = 0º indicates the sign and magnitude of the roll rate damping. Twists such as in figure 7.56 indicate a change in sign of roll rate damping.

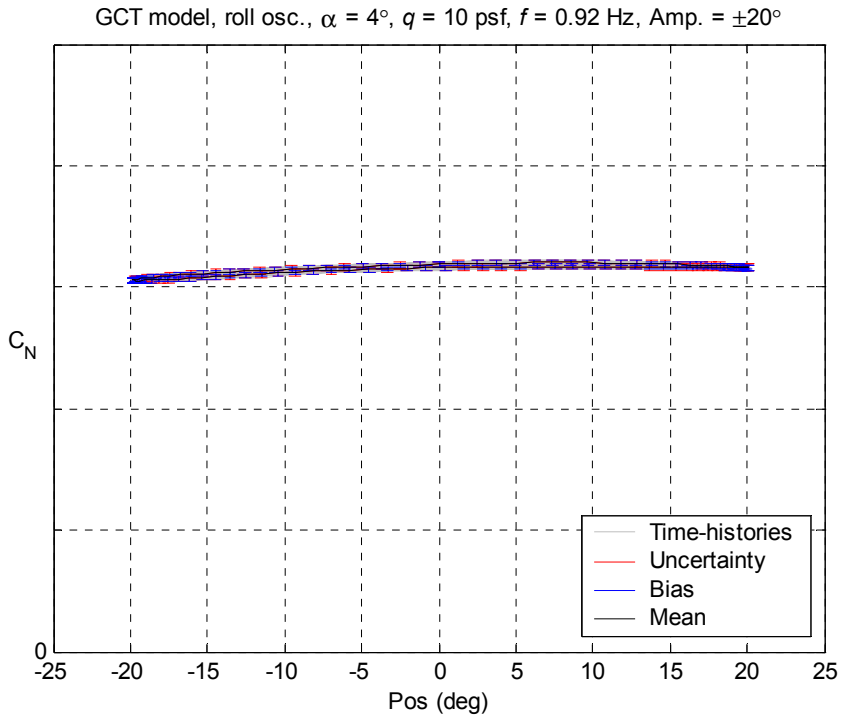

Figure 7.37 Time-history of 120 cycles for GCT oscillated at 0.92 Hz and uncertainty of 100 interpolated points around the mean cycle for normal force coefficient at α = 4º.

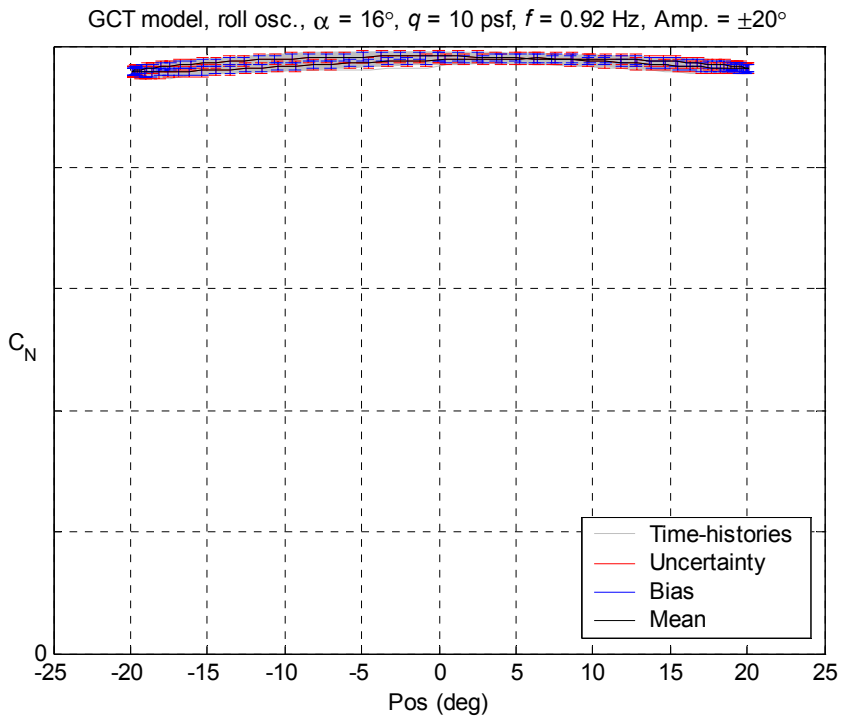

Figure 7.38 Time-history of 120 cycles for GCT oscillated at 0.92 Hz and uncertainty of 100 interpolated points around the mean cycle for normal force coefficient at α = 16º.

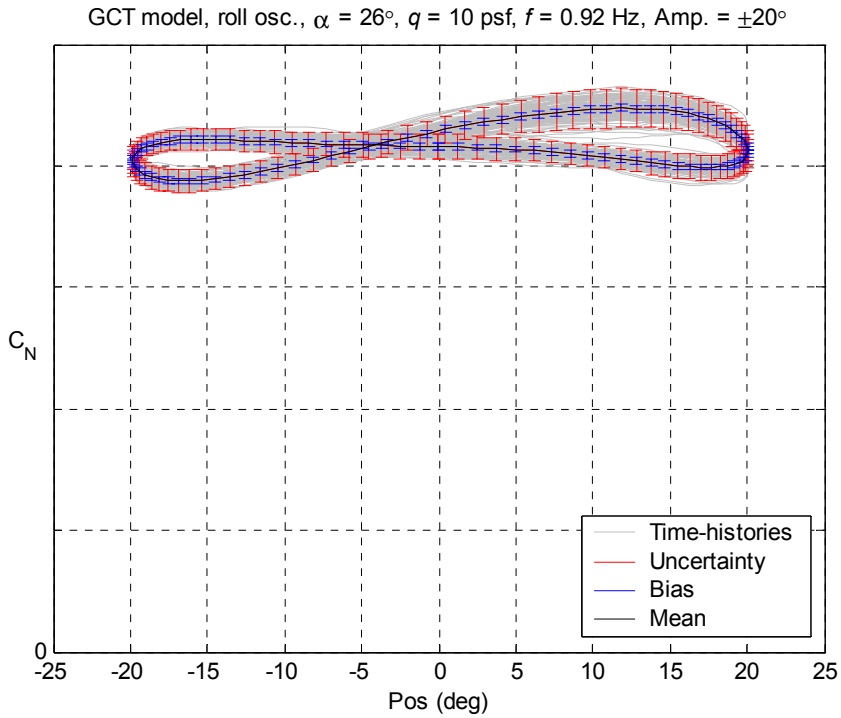

Figure 7.39 Time-history of 120 cycles for GCT oscillated at 0.92 Hz and uncertainty of 100 interpolated points around the mean cycle for normal force coefficient at α = 26º.

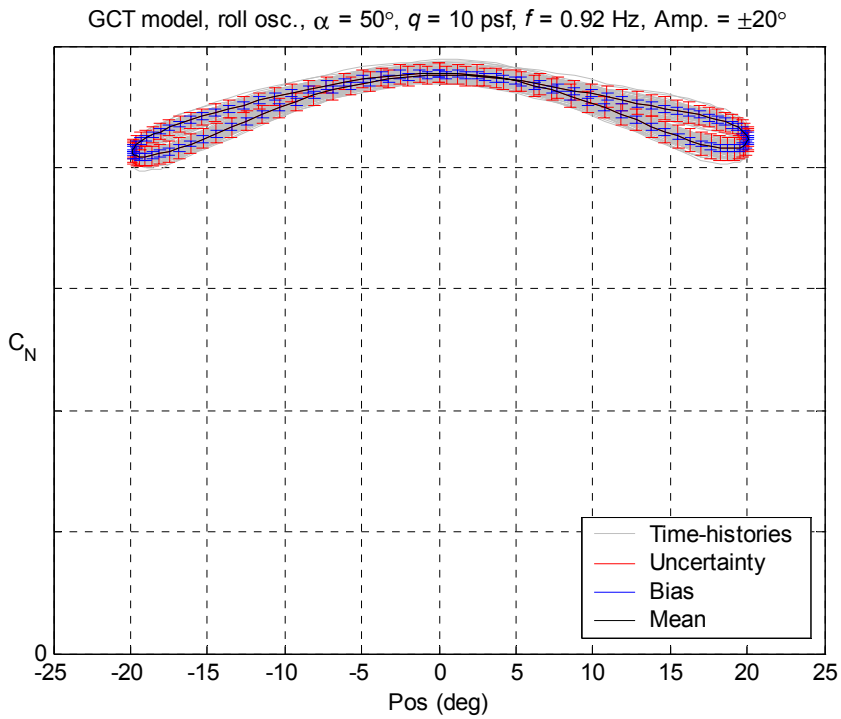

Figure 7.40 Time-history of 120 cycles for GCT oscillated at 0.92 Hz and uncertainty of 100 interpolated points around the mean cycle for normal force coefficient at α = 50º.

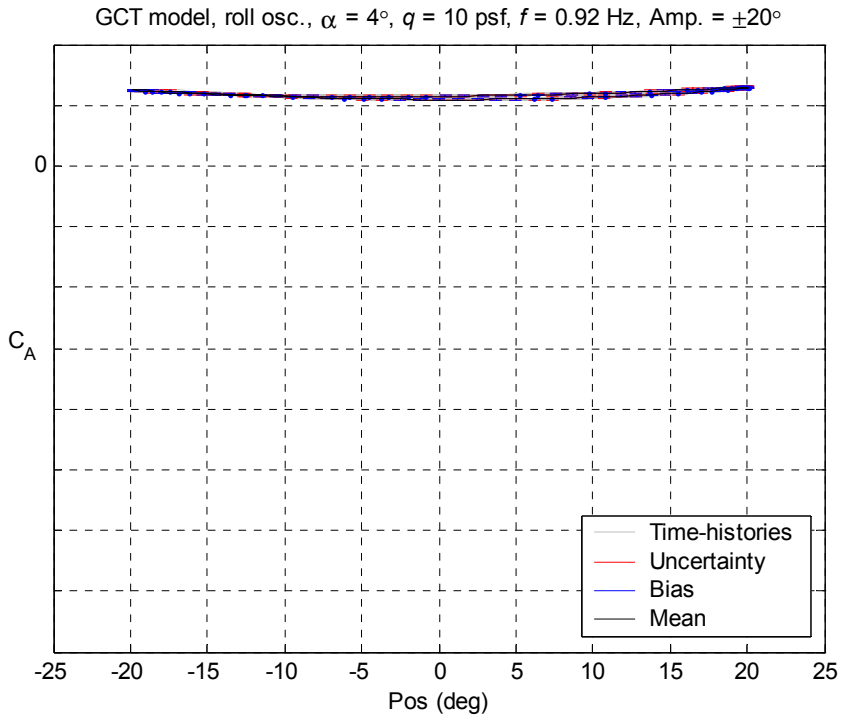

Figure 7.41 Time-history of 120 cycles for GCT oscillated at 0.92 Hz and uncertainty of 100 interpolated points around the mean cycle for axial force coefficient at α = 4º.

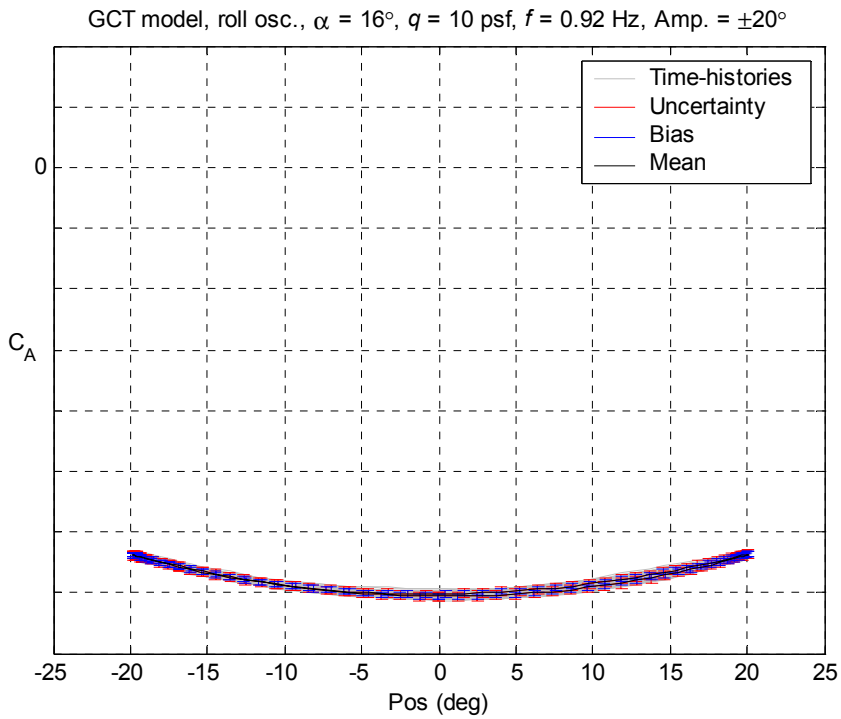

Figure 7.42 Time-history of 120 cycles for GCT oscillated at 0.92 Hz and uncertainty of 100 interpolated points around the mean cycle for axial force coefficient at α = 16º.

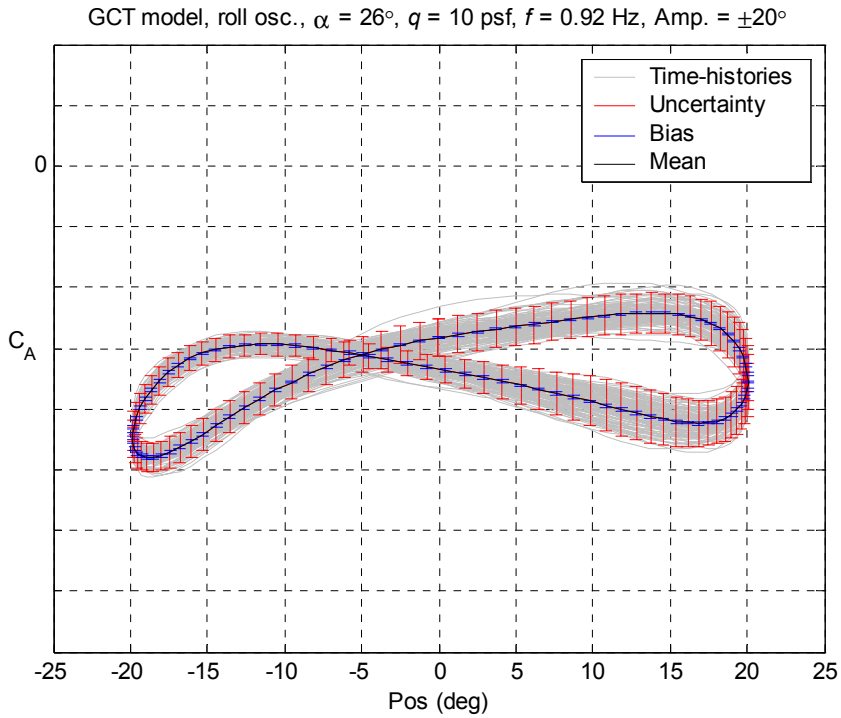

Figure 7.43 Time-history of 120 cycles for GCT oscillated at 0.92 Hz and uncertainty of 100 interpolated points around the mean cycle for axial force coefficient at α = 26º.

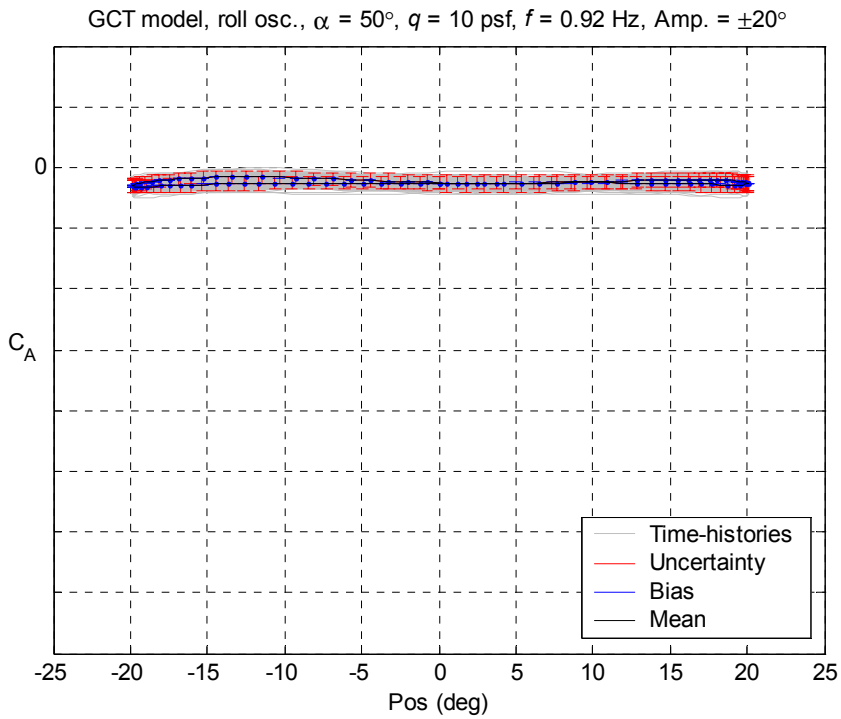

Figure 7.44 Time-history of 120 cycles for GCT oscillated at 0.92 Hz and uncertainty of 100 interpolated points around the mean cycle for axial force coefficient at α = 50º.

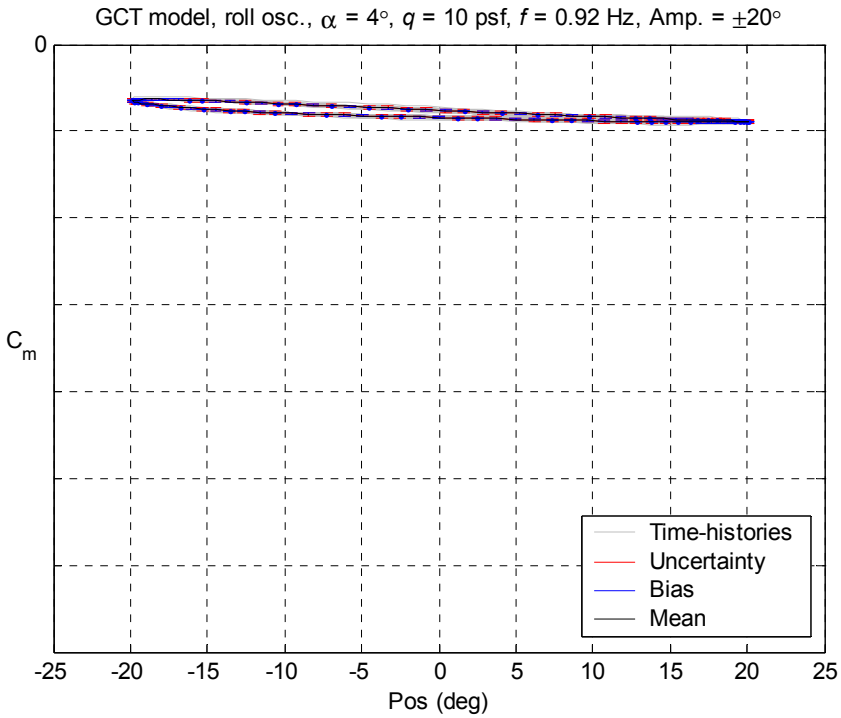

Figure 7.45 Time-history of 120 cycles for GCT oscillated at 0.92 Hz and uncertainty of 100 interpolated points around the mean cycle for pitching moment coefficient at α = 4º.

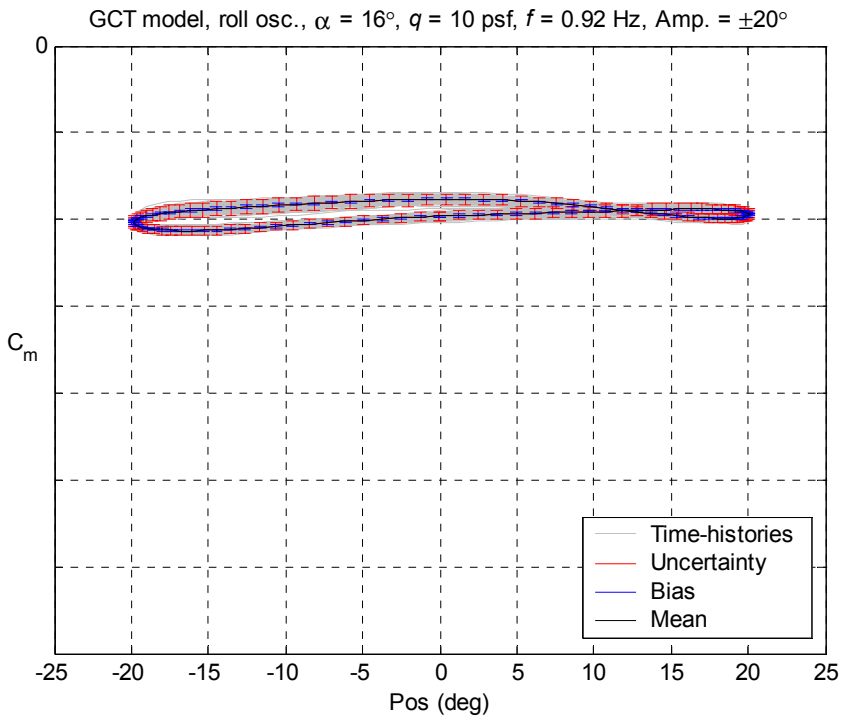

Figure 7.46 Time-history of 120 cycles for GCT oscillated at 0.92 Hz and uncertainty of 100 interpolated points around the mean cycle for pitching moment coefficient at α = 16º.

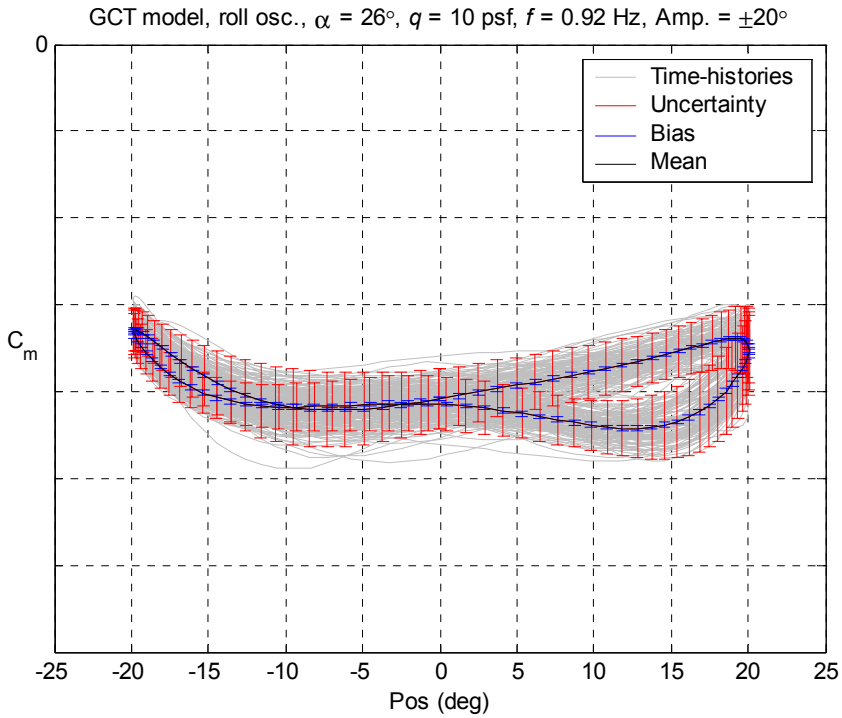

Figure 7.47 Time-history of 120 cycles for GCT oscillated at 0.92 Hz and uncertainty of 100 interpolated points around the mean cycle for pitching moment coefficient at α = 26º.

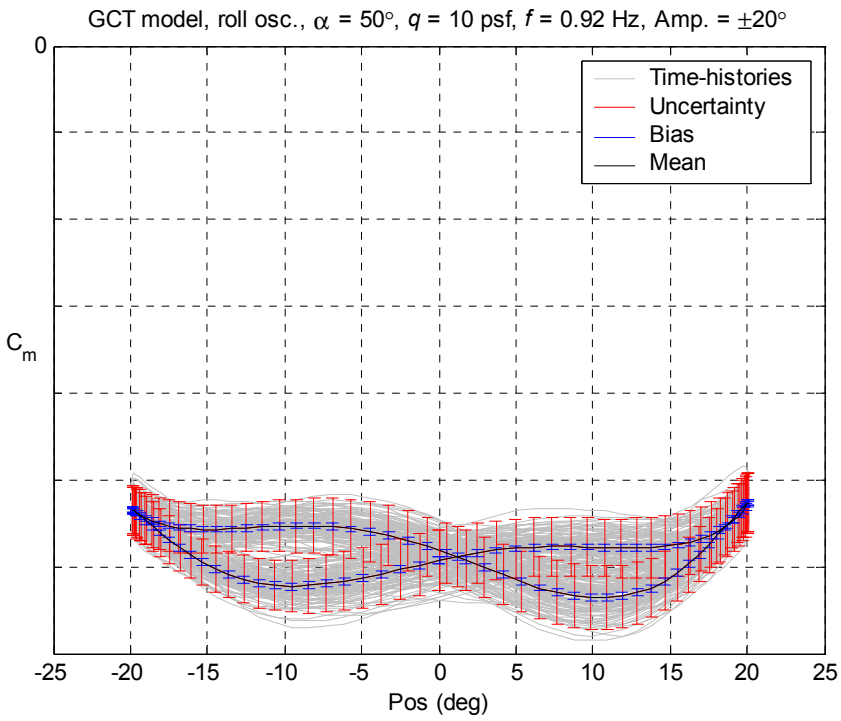

Figure 7.48 Time-history of 120 cycles for GCT oscillated at 0.92 Hz and uncertainty of 100 interpolated points around the mean cycle for pitching moment coefficient at α = 50º.

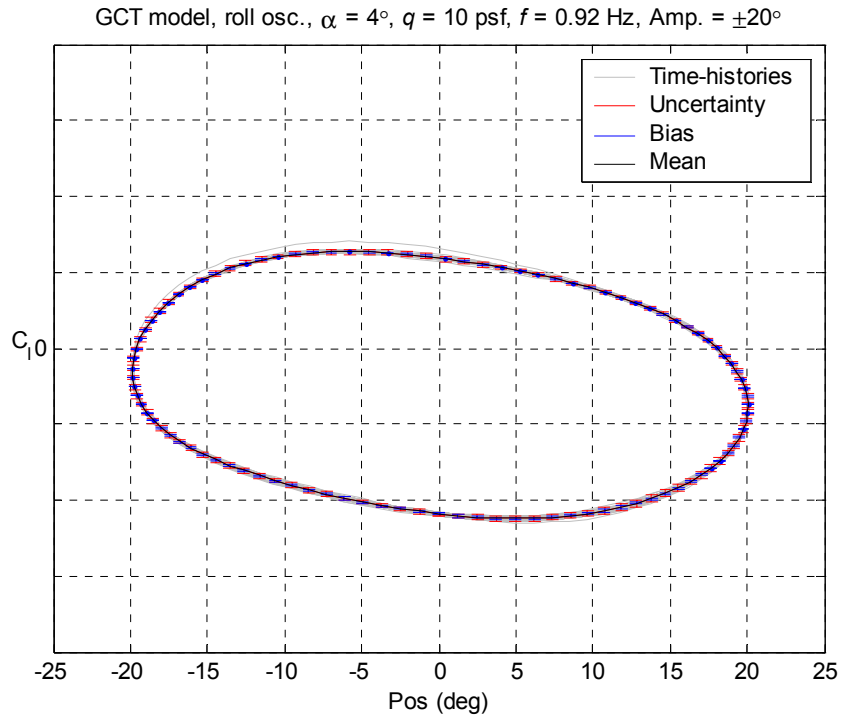

Figure 7.49 Time-history of 120 cycles for GCT oscillated at 0.92 Hz and uncertainty of 100 interpolated points around the mean cycle for rolling moment coefficient at α = 4º.

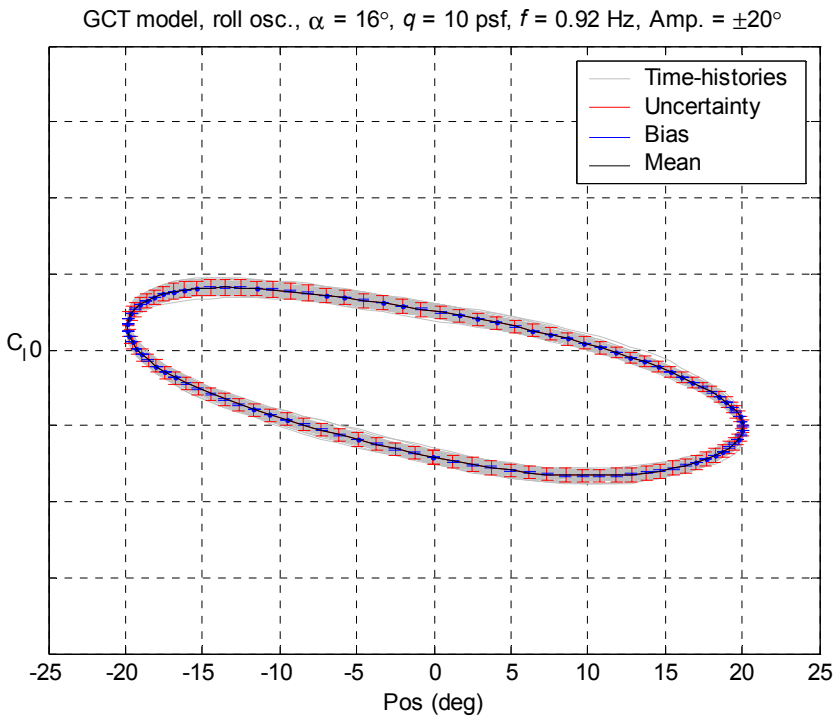

Figure 7.50 Time-history of 120 cycles for GCT oscillated at 0.92 Hz and uncertainty of 100 interpolated points around the mean cycle for rolling moment coefficient at α = 16º.

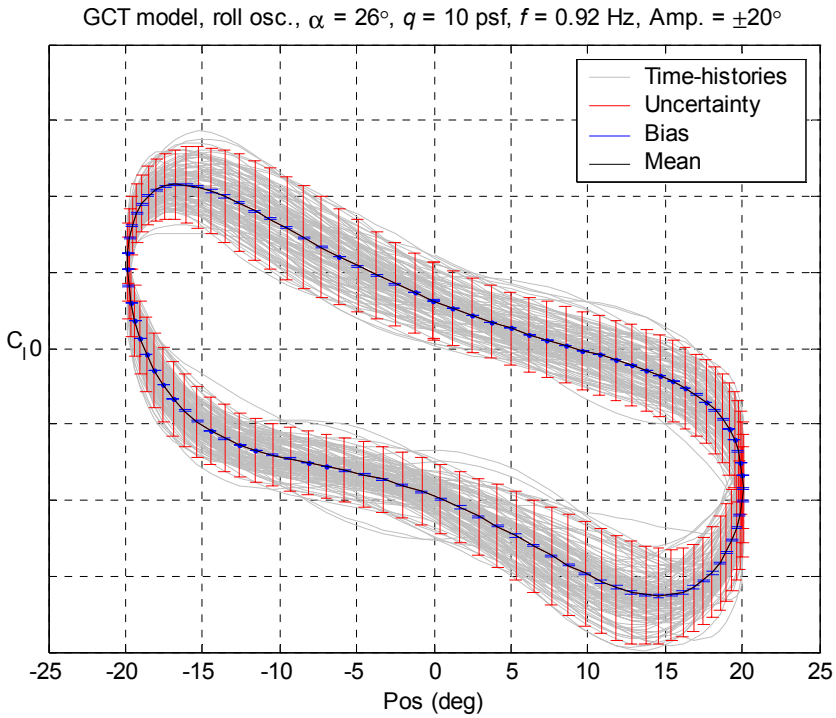

Figure 7.51 Time-history of 120 cycles for GCT oscillated at 0.92 Hz and uncertainty of 100 interpolated points around the mean cycle for rolling moment coefficient at α = 26º.

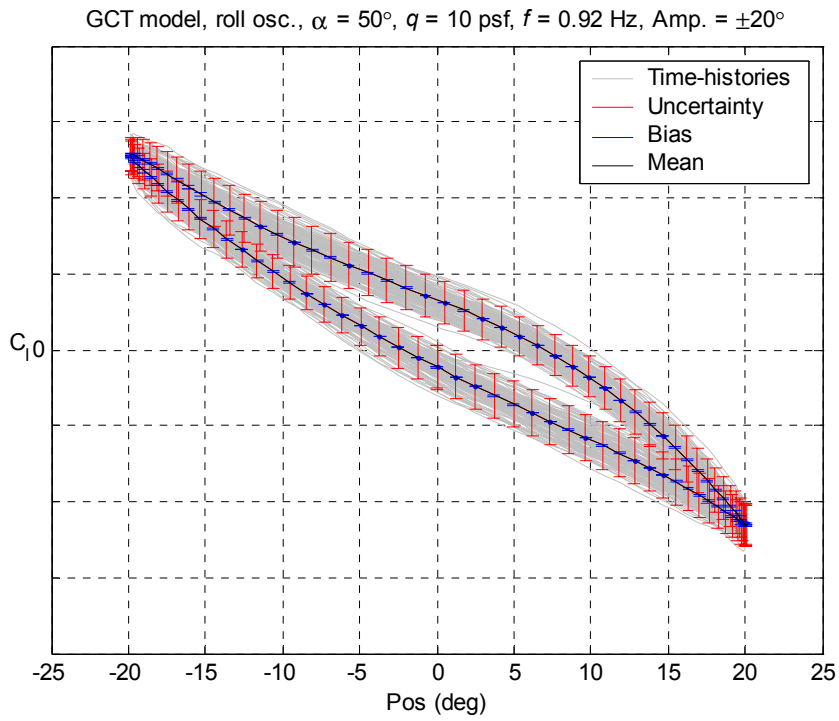

Figure 7.52 Time-history of 120 cycles for GCT oscillated at 0.92 Hz and uncertainty of 100 interpolated points around the mean cycle for rolling moment coefficient at α = 50º.

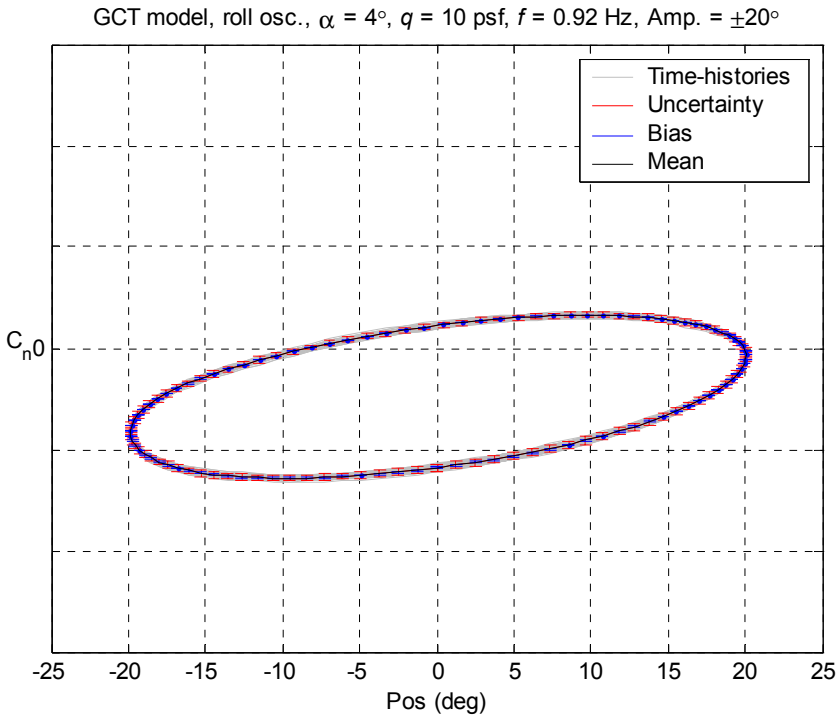

Figure 7.53 Time-history of 120 cycles for GCT oscillated at 0.92 Hz and uncertainty of 100 interpolated points around the mean cycle for yawing moment coefficient at α = 4º.

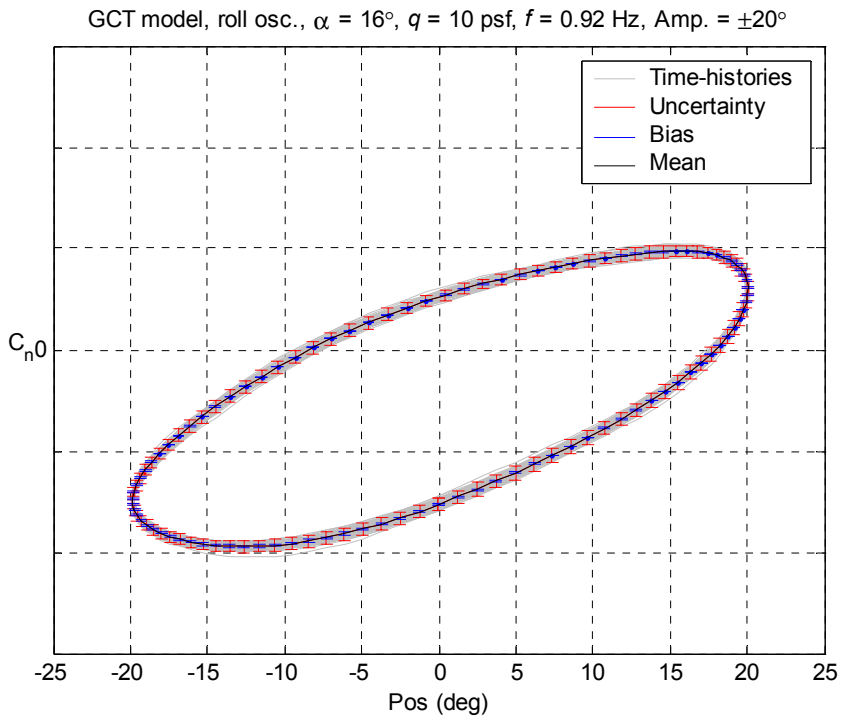

Figure 7.54 Time-history of 120 cycles for GCT oscillated at 0.92 Hz and uncertainty of 100 interpolated points around the mean cycle for yawing moment coefficient at α = 16º.

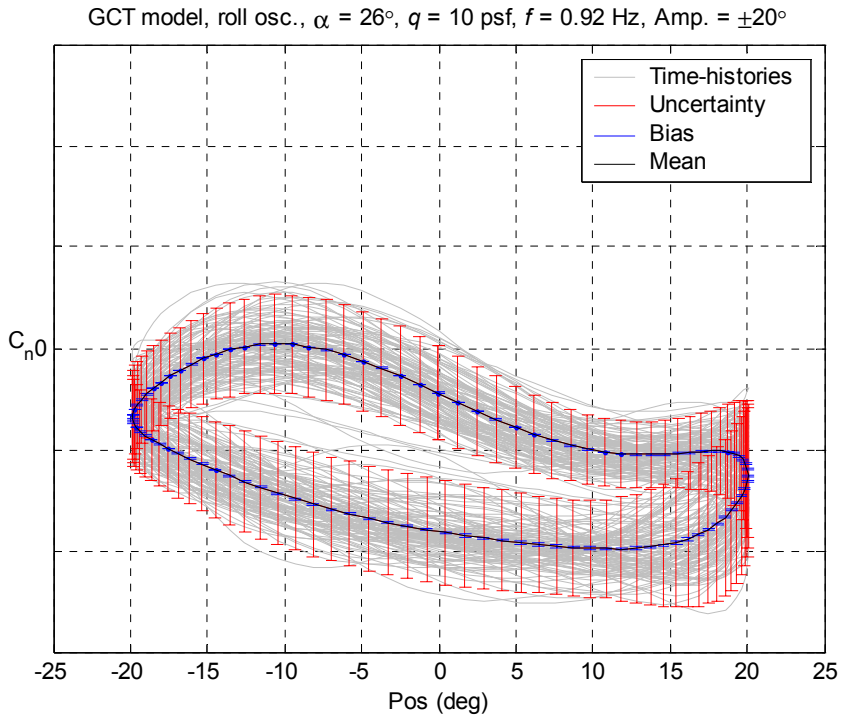

Figure 7.55 Time-history of 120 cycles for GCT oscillated at 0.92 Hz and uncertainty of 100 interpolated points around the mean cycle for yawing moment coefficient at α = 26º.

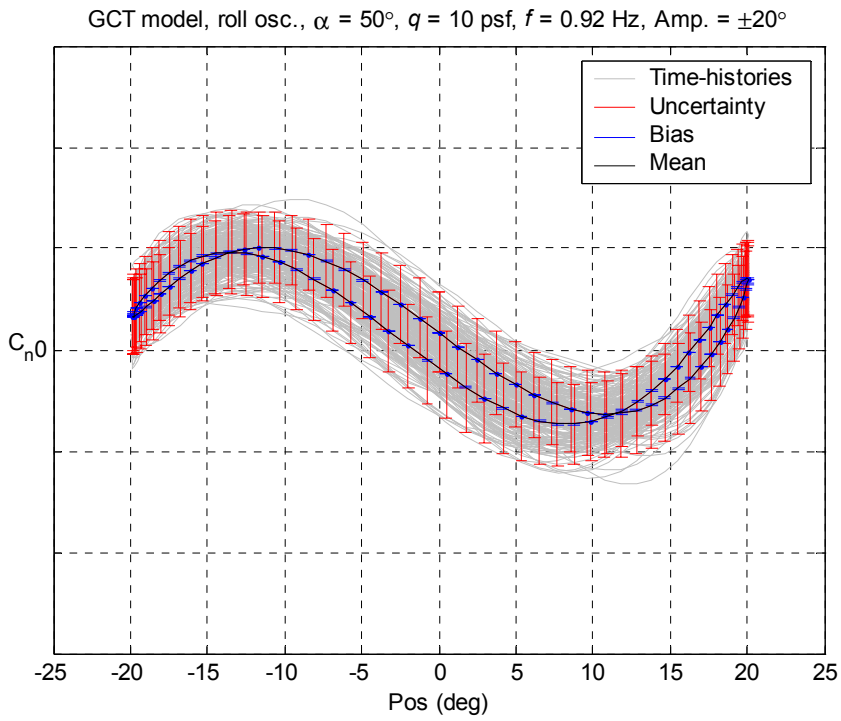

Figure 7.56 Time-history of 120 cycles for GCT oscillated at 0.92 Hz and uncertainty of 100 interpolated points around the mean cycle for yawing moment coefficient at α = 50º.

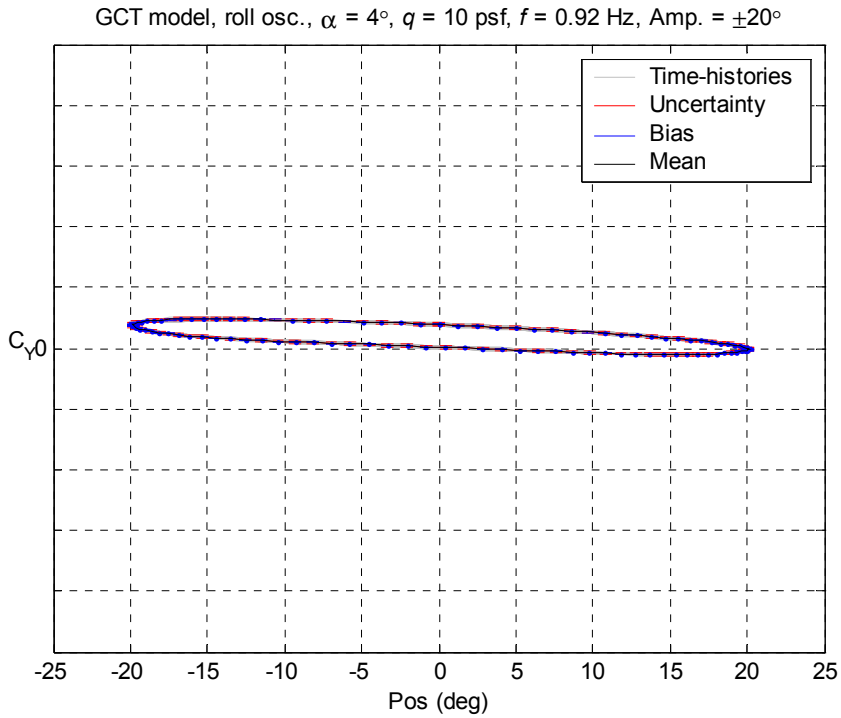

Figure 7.57 Time-history of 120 cycles for GCT oscillated at 0.92 Hz and uncertainty of 100 interpolated points around the mean cycle for side force coefficient at α = 4º.

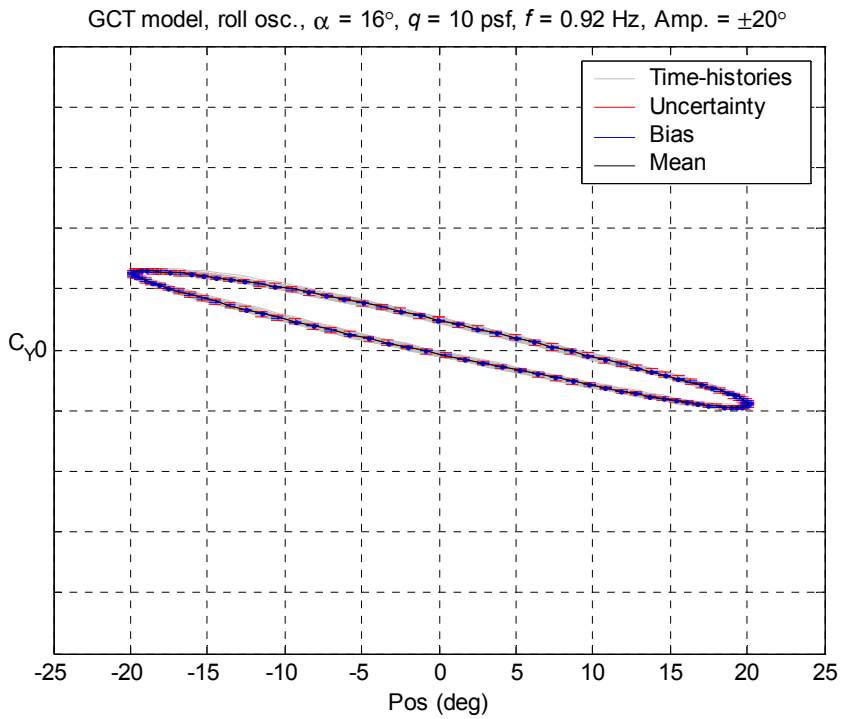

Figure 7.58 Time-history of 120 cycles for GCT oscillated at 0.92 Hz and uncertainty of 100 interpolated points around the mean cycle for side force coefficient at α = 16º.

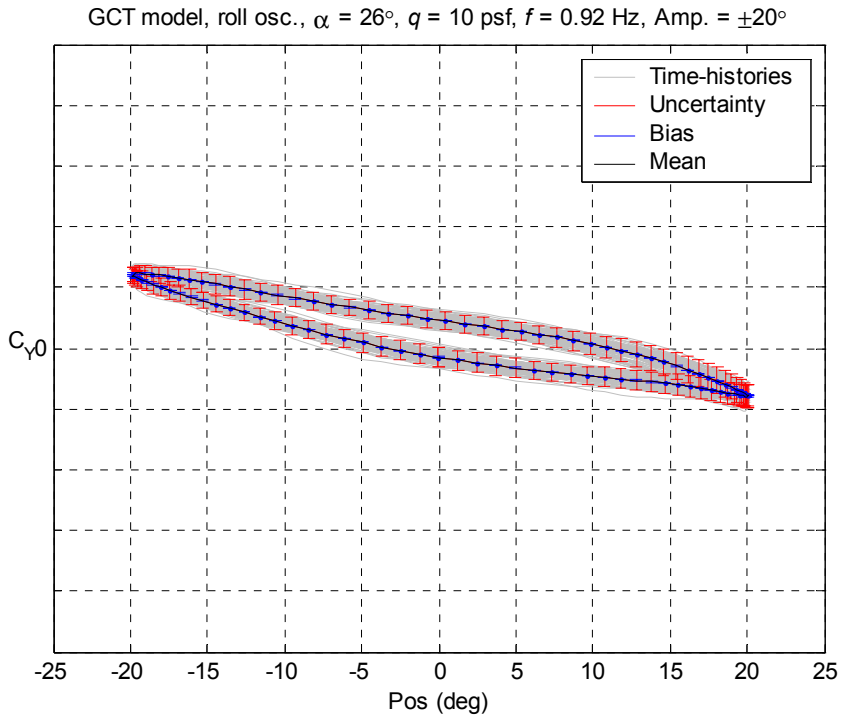

Figure 7.59 Time-history of 120 cycles for GCT oscillated at 0.92 Hz and uncertainty of 100 interpolated points around the mean cycle for side force coefficient at α = 26º.

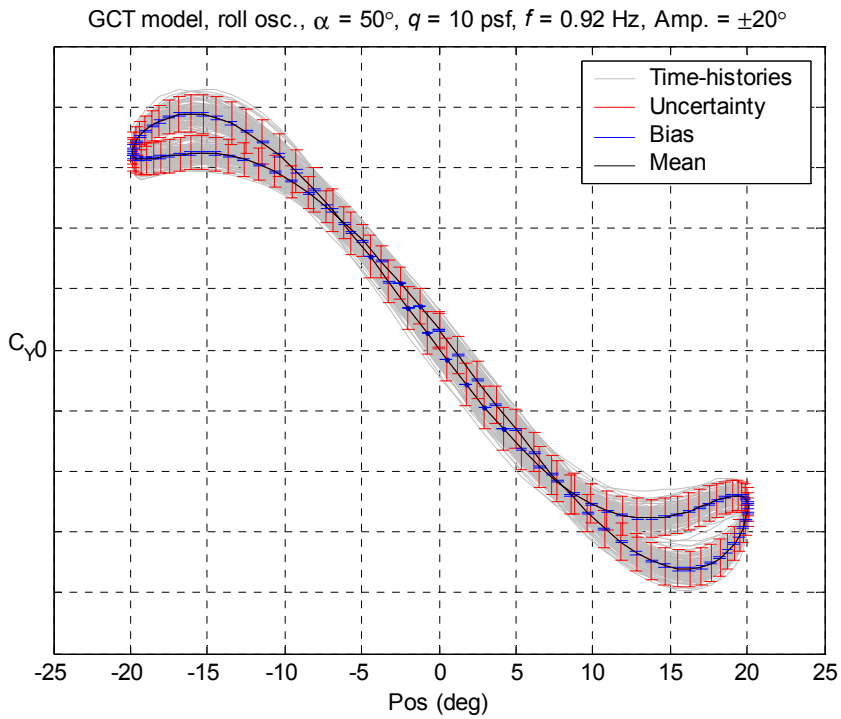

Figure 7.60 Time-history of 120 cycles for GCT oscillated at 0.92 Hz and uncertainty of 100 interpolated points around the mean cycle for side force coefficient at $\alpha = 50^{\circ}$.

8 Efficient Testing

8-1 Introduction

The material presented thus far provided a means of estimating the uncertainty of wind tunnel data. The techniques presented were applied after the complete data set was collected and thus provided an estimate of uncertainty after the test was over. One question every wind tunnel test engineer should ask himself/herself is, "Am I sampling long enough?" or conversely "Why am I sampling so long?" Coleman and Steele suggest 'data sets for determining estimates of standard deviations must be acquired over a time period that is large relative to the time scales of the factors that have a significant influence on the data and that contribute to the random errors.' Two questions then arise: what are the factors that have significant influence on the data and what factors contribute to the random error in the data? The "data" for any wind tunnel test are all measurements acquired. There is no doubt the inherent unsteady aerodynamics can be a significant factor for both the mean of the data and the random "error" or uncertainty. As stated many times before, the random uncertainty is a combination of unsteady aerodynamics, structural vibrations, electrical noise, etc. The hope is the latter are small with respect to the aerodynamics. The question still remains, how does one know how long to sample? Typically a spectrum of the data will provide insight to the lowest frequency of significance, i.e. the lowest frequency with a spike above the noise floor. This method works well if the signal to noise ratio is high enough. Another approach is to study how the mean and standard deviation of the data change with time. Chapters 6 and 7 described typical static and forced oscillation test techniques, which sampled data for 8 seconds and 40 cycles respectively. Each sample period whether it is measured in time or cycles was selected after a study of spectrums and rolling means of an increasing period for several models over a range of conditions. The goal at the time was to determine a sample period long enough to encompass any significant variation within the data from several different models at various conditions. Thus, the standard sample periods of 8 seconds for static tests and 40 cycles for forced oscillation tests were selected and remain the standard for testing in the subject tunnel with the test rigs used. The selection of the standard periods was primarily influenced by regions near and post stall, which require longer sample periods to estimate a "good" mean. Relatively benign regions, such as the linear region of the lift curve, are often over sampled. What is needed is a real-time or near real-time condition specific analysis of when is the "right" time to stop acquiring data at a given test condition.

8-2 Dynamic testing considerations

Forced oscillation testing stands to benefit the most from any kind of data acquisition optimization since it is much more time consuming than static testing. The frequencies tested ranged from approximately 0.30 Hz to 1.10 Hz. A low frequency run with 40 oscillations and with 20 angle-of-attack points would take about 45 minutes, neglecting time to set the angle-of-attack, bring the tunnel up to q and record the tare. The cost of a large subsonic wind tunnel can

range from $20,000 to $30,000 per day. The low frequency run above, with two 8 hr. shifts, equates to a $940 to $1400 investment.

The objective, for any measurement, is to estimate where in some n-dimensional space the true answer lies, usually within some bounds. This is certainly the case with wind tunnel tests. The mean serves as a reference point or expected value for the given conditions. The uncertainty bounds the range about the mean of inherent unsteady aerodynamics at that condition, with a specified confidence. It will be assumed the range of variation about the mean is symmetric, i.e. the uncertainty could equally be positive or negative, or Gaussian.

Equations (2.3) and (2.4) show the mean and the standard deviation of a Gaussian distribution will approach the true mean and true standard deviation as the number of readings approaches infinity. These mean and standard deviation histories, which are continuously recalculated as new readings are available will be defined as the "rolling mean" and "rolling standard deviation". The deltas between successive rolling means and rolling standard deviations or their gradients will generally decay as the number of readings approaches infinity. The gradients may oscillate in sign, as the random error is equally likely to be positive or negative, but the over all decay of the absolute value of the gradients will be similar to an asymptotic decay.

Consider the gradients of the rolling standard deviation of all 100 points around the cycle in figure 7.51. Every point will have a different gradient. The location on the cycle at which the maximum gradient occurs may be different from cycle to cycle. That maximum gradient can be used to identify how much the uncertainty of the entire cycle is changing from cycle to cycle. Now consider a 10-cycle moving average of the maximum gradients, g_m (figure 8.1). A moving average was necessary to smooth the maximum gradients. Ten cycles were chosen for the moving average so the precision limit could be estimated with 95% confidence by $2S_x$ [11]. The moments from the run and the tare were non-dimensionalized based on the mean dynamic pressure (or expected mean dynamic pressure when non-dimensionalizing the tare), the reference area and span from figure 3.2b. The non-dimensionalization was necessary to compare the gradients of the moments from the run and tare with the gradient of the coefficient. Notice, at the scale presented, the gradients level off around 60 cycles. The tare gradients level even sooner. A threshold could be set such that if a gradient crosses a prescribed tolerance there is no need to continue collecting data at that condition. The bias of the balance, for example would be a good tolerance limit. However there is no guarantee a threshold will be met especially when a new model is tested. Some flexibility needs to be built into the stopping criteria.

The goal is to stop when the mean and uncertainty (or standard deviation since the bias is fixed) stop changing significantly. It is proposed a threshold be set that is 10% of the average rate of change of the uncertainty after 11 cycles. The 11-cycle wait is needed because the standard deviation of the first cycle is zero. This would provide a metric, which is case specific, provides an upper bound on the uncertainty around the cycle, and is sensitive to variation of the mean. If the variation in the cycles is small, such as in the linear region of the lift curve slope, the 10% threshold will be very low. To prevent from sampling forever to reduce the already low values, another threshold is needed, and use of the known balance accuracies are proposed. The balance accuracy as a function of load is not available as discussed in chapter 4. However, experience has shown that balance measurements can be made to at least half of the full-scale accuracy reported by the calibration laboratory. Thus half the listed balance accuracy will be used as a fixed threshold. The final data acquisition stopping criteria is achieved when g_m is 10% of the g_m after the initial 11 cycles or less then half of the balance accuracy. Data

acquisition continues until these criteria are satisfied for all balance components. This process is outlined in Figure 8.2. Figures 8.3 through 8.14 show the time history of stopping criteria for the tare and the data from the roll oscillations of the GCT. The gradient of the mean is also shown for reference but is not used as a stopping criterion.

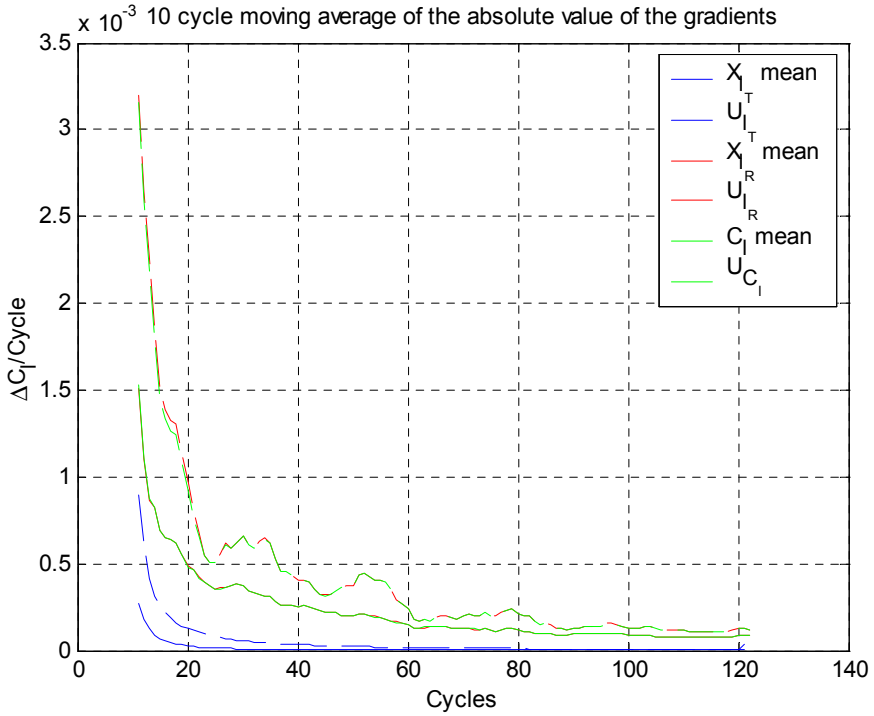

Figure 8.1 10 cycle moving average of the absolute value of gradients of mean and uncertainty as they vary with increasing cycles for the non-dimensionalized tare rolling moment, non-dimensionalized run rolling moment and rolling moment coefficient of the GCT, $\alpha = 26°$.

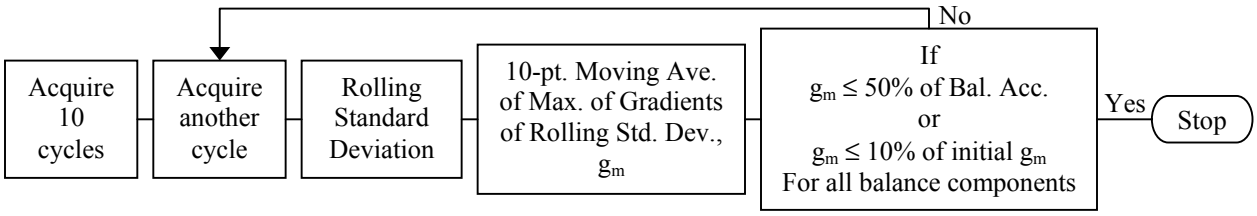

Figure 8.2 Flowchart of forced oscillation data acquisition termination process.

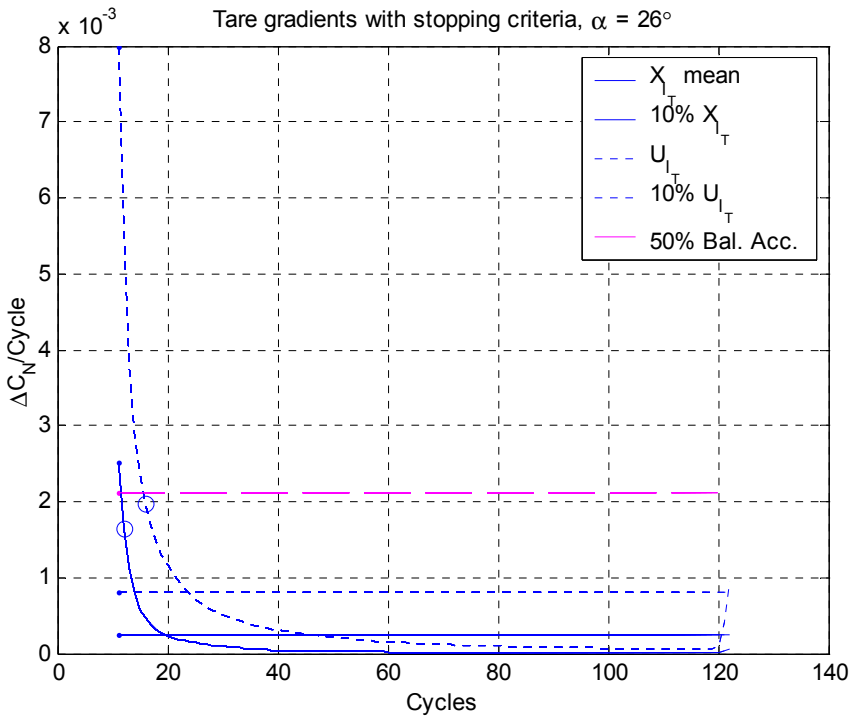

Figure 8.3 Time history of stopping criteria for normal force of tare for 121 cycles. Circles indicate what cycle stopping criteria is met.

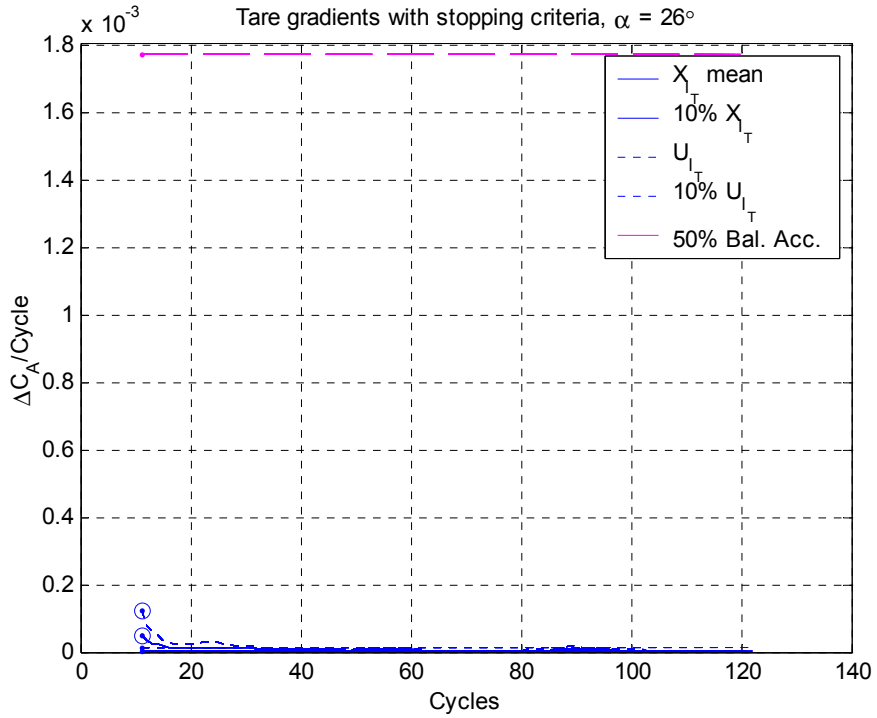

Figure 8.4 Time history of stopping criteria for axial force of tare for 121 cycles. Circles indicate what cycle stopping criteria is met.

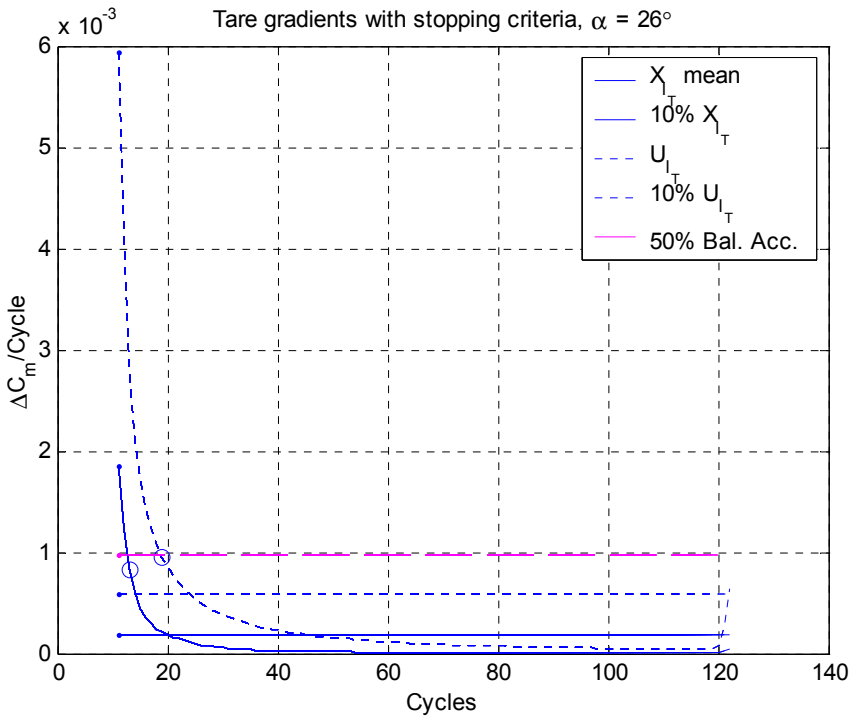

Figure 8.5 Time history of stopping criteria for pitching moment of tare for 121 cycles. Circles indicate what cycle stopping criteria is met.

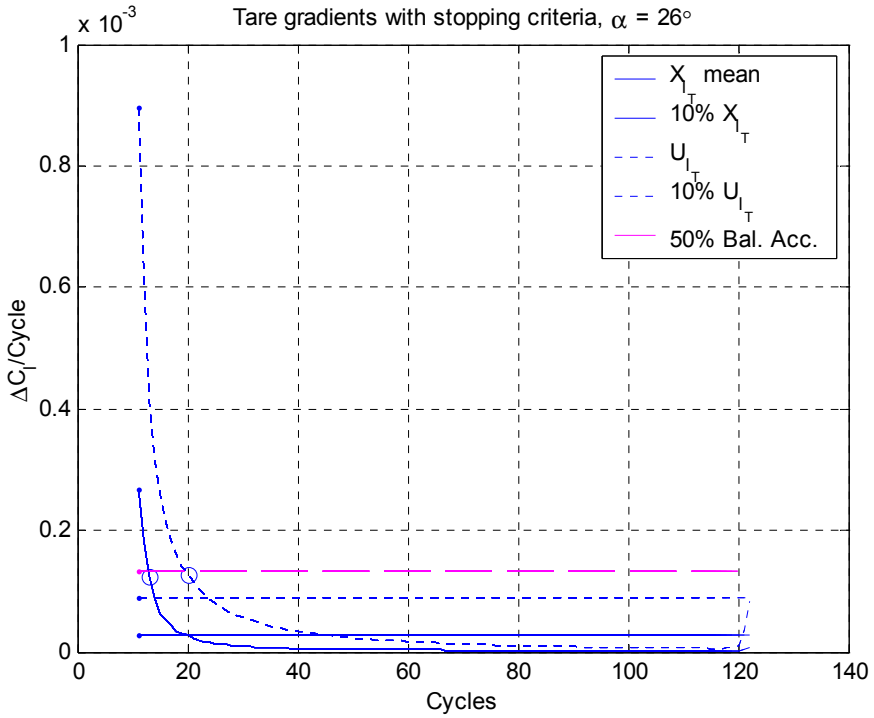

Figure 8.6 Time history of stopping criteria for rolling moment of tare for 121 cycles. Circles indicate what cycle stopping criteria is met.

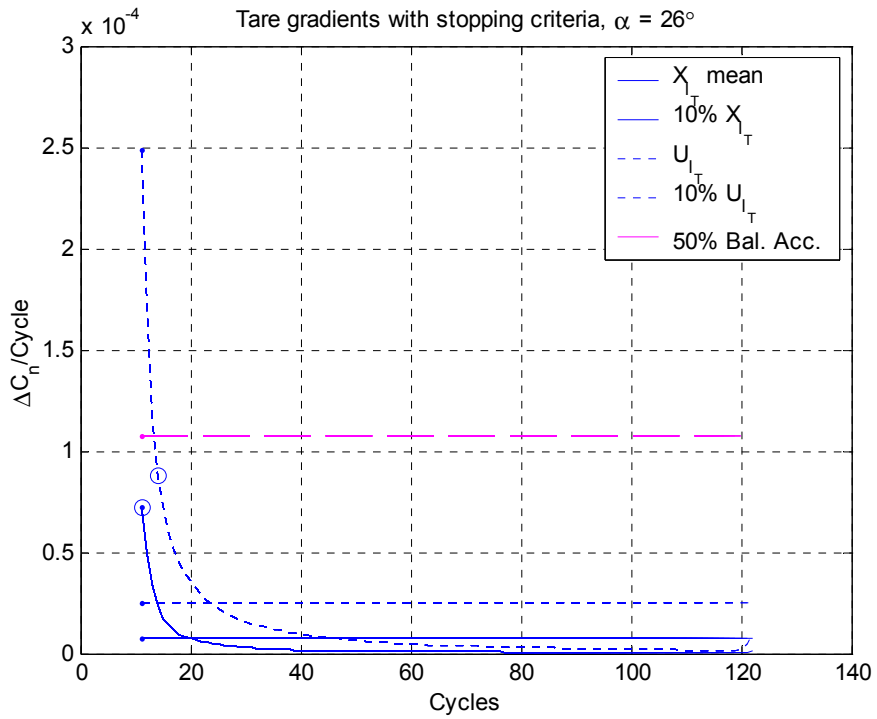

Figure 8.7 Time history of stopping criteria for yawing moment of tare for 121 cycles. Circles indicate what cycle stopping criteria is met.

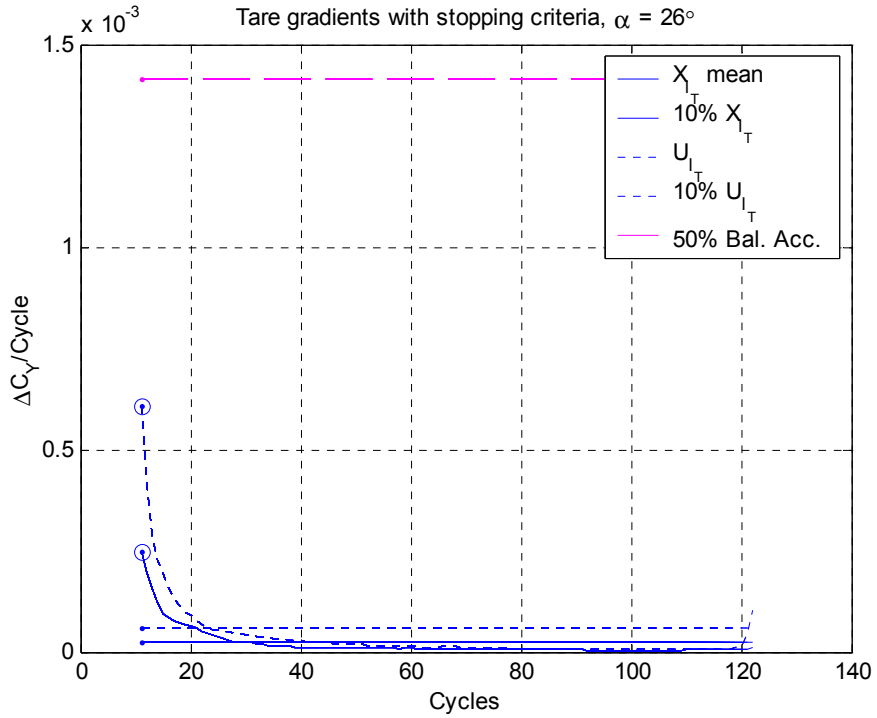

Figure 8.8 Time history of stopping criteria for side force of tare for 121 cycles. Circles indicate what cycle stopping criteria is met.

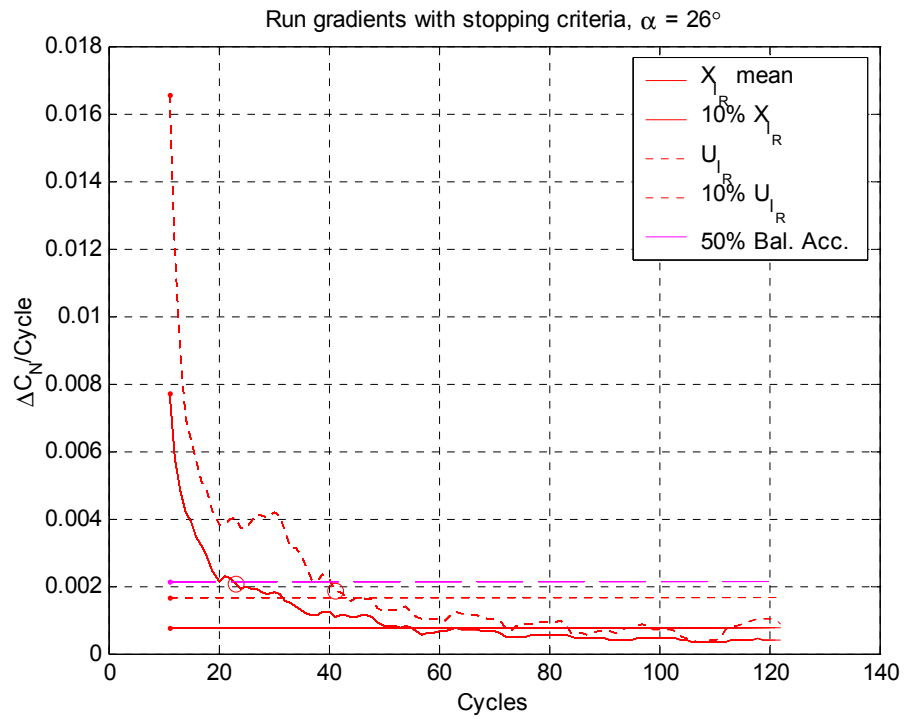

Figure 8.9 Time history of stopping criteria for normal force of run at 26 degrees for 121 cycles. Circles indicate what cycle stopping criteria is met.

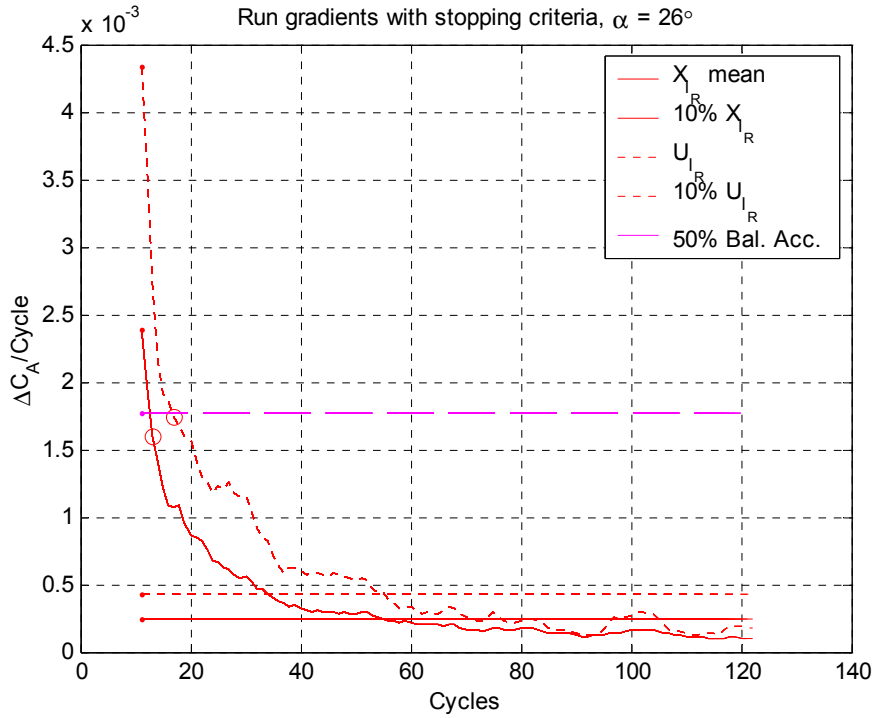

Figure 8.10 Time history of stopping criteria for axial force of run at 26 degrees for 121 cycles. Circles indicate what cycle stopping criteria is met.

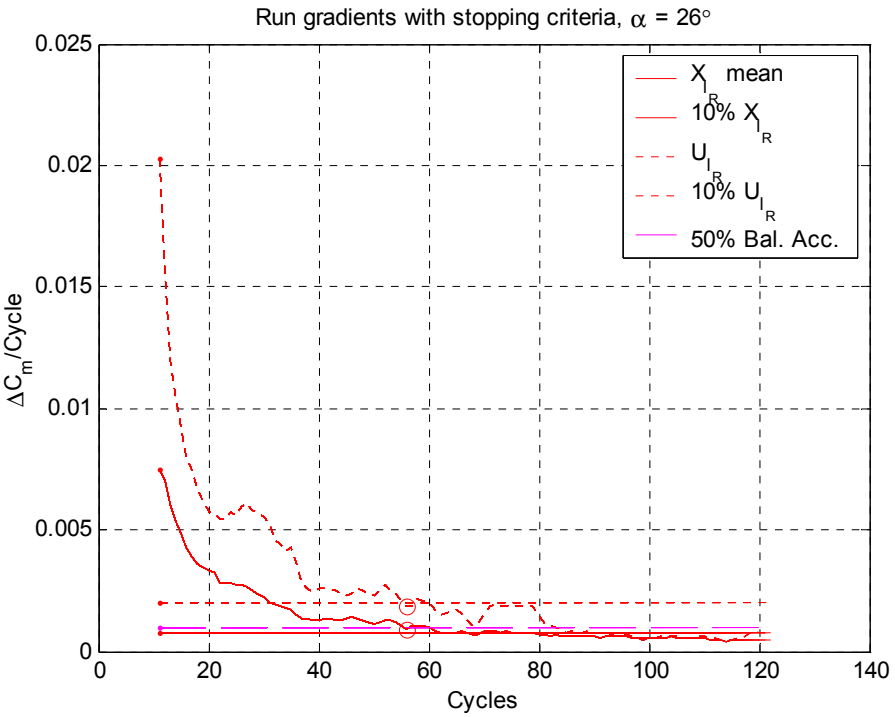

Figure 8.11 Time history of stopping criteria for pitching moment of run at 26 degrees for 121 cycles. Circles indicate what cycle stopping criteria is met.

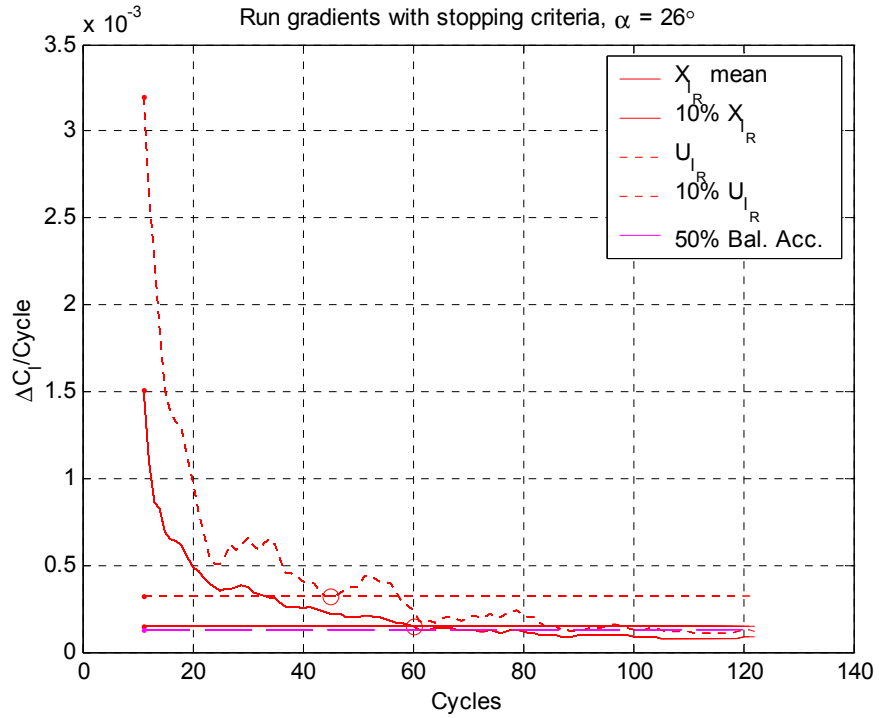

Figure 8.12 Time history of stopping criteria for rolling moment of run at 26 degrees for 121 cycles. Circles indicate what cycle stopping criteria is met.

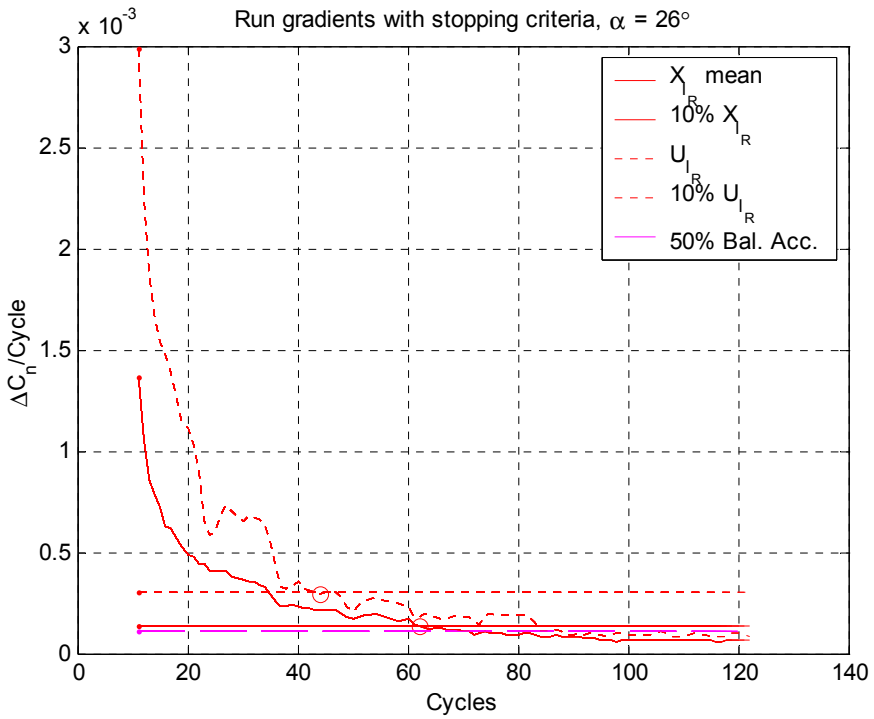

Figure 8.13 Time history of stopping criteria for yawing moment of run at 26 degrees for 121 cycles. Circles indicate what cycle stopping criteria is met.

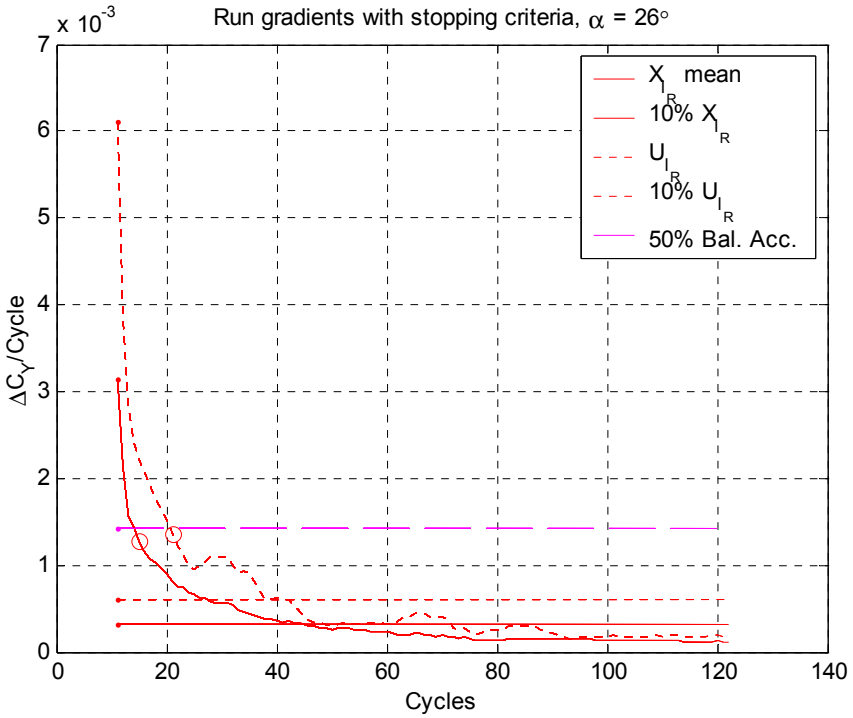

Figure 8.14 Time history of stopping criteria for side force of run at 26 degrees for 121 cycles. Circles indicate what cycle stopping criteria is met.

The stopping criteria presented applies to all corrected balance loads, i.e. after interactions are removed. Figures 8.9 through 8.14 show the stopping criteria are not met at the same time for all balance loads. Thus the last load to meet the terminating conditions will terminate sampling for that condition. Figures 8.3 through 8.8 show the tare could have been stopped after 20 cycles, likewise figures 8.9 through 8.14 show sampling at 26 degrees could have ended after 56 cycles. Pitching moment was the last to meet its threshold for the uncertainty. Note in this example yawing moment was the last to meet the criteria for the mean. Normally, the gradients of the uncertainty are more conservative, in terms of cycles, than that of the mean. Figures 8.15 and 8.16 show the results of the stopping criteria for the 120 cycle runs of the fighter model and GCT presented in chapter 7. The yaw oscillations for the fighter model presented in chapter 7 could have ended after 11 cycles for the tare and 11, 38, 37, 48 and 40 cycles at α = 10º, 38º, 40º, 50º and 60º respectively. The roll oscillations for the GCT could have stopped after 20 cycles for the tare and15, 24, 60, and 45 cycles at α = 4º, 16º, 26º and 50º respectively. The number of cycles for the fighter and the GCT examples were reduced by 23% and 18% respectively from the 40-cycle standard. Figures 8.18 and 8.19 give examples of how this technique can be used for post-analysis of standard 40-cycle data to see where more cycles were needed and where more cycles were recorded than necessary. Green is used to indicate the stopping criteria were meet before the cycle limits, 40-cycles, where reached. Red indicates the stopping criteria were not reached before reaching the end of the recorded data cycles. The first and last 450 points in the 40-cycle time-histories were removed to remove any transients from the filter. This is why the cycle limits do not reach exactly 40 in some cases, but do reach the total number of complete cycles. As one would expect more data is acquired than needed in the linear region and not enough near and post stall.

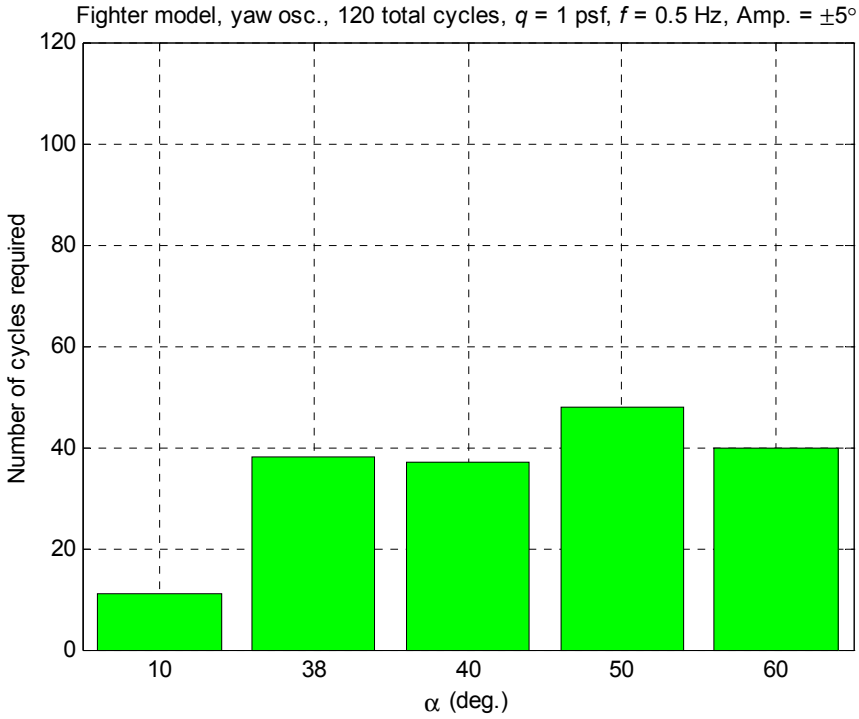

Figure 8.15 Cycles required for fighter model using stopping criteria.

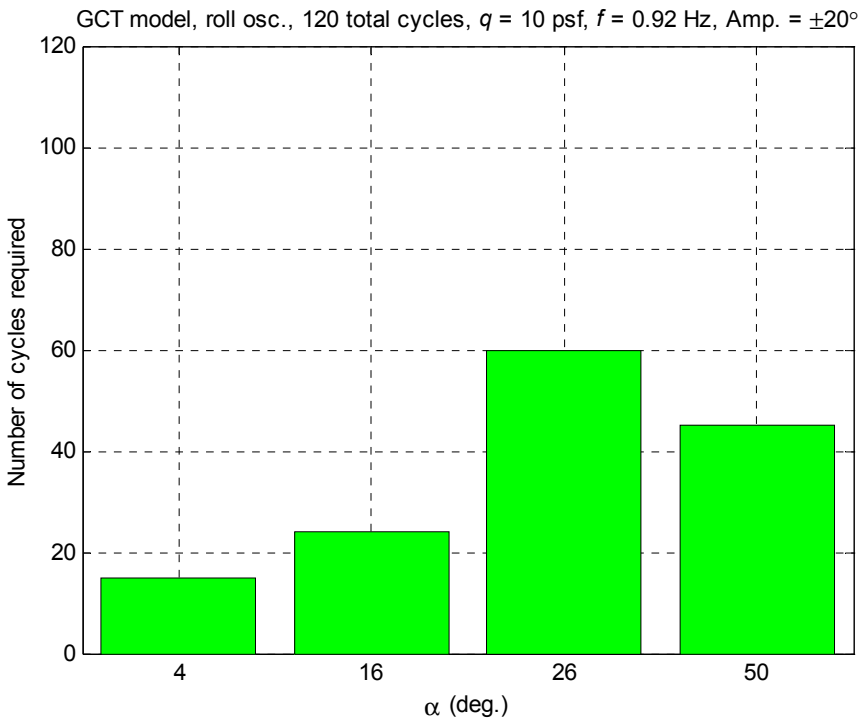

Figure 8.16 Cycles required for GCT model using stopping criteria.

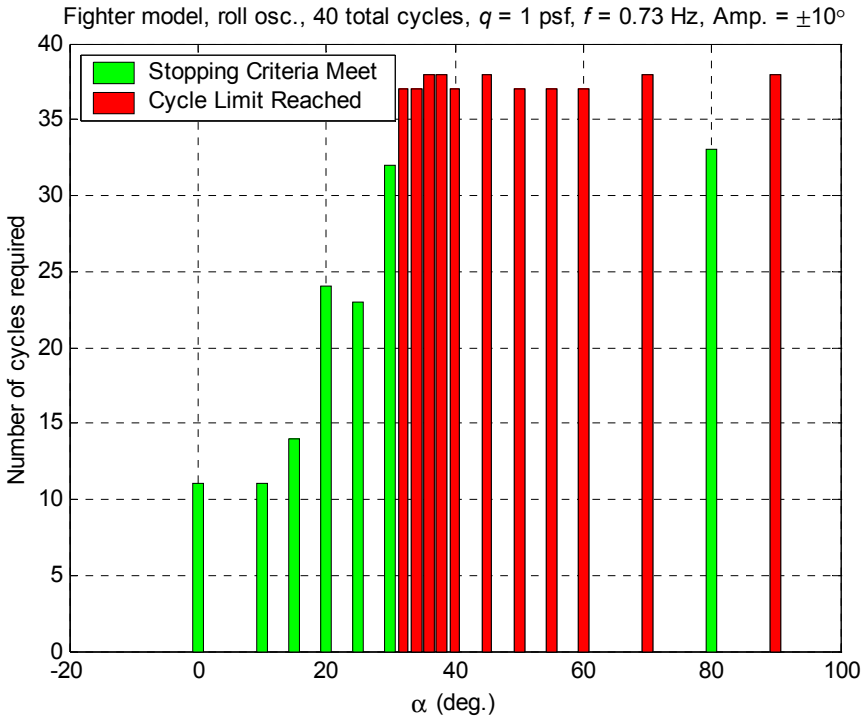

Figure 8.17 Example of post-analysis for fighter model.

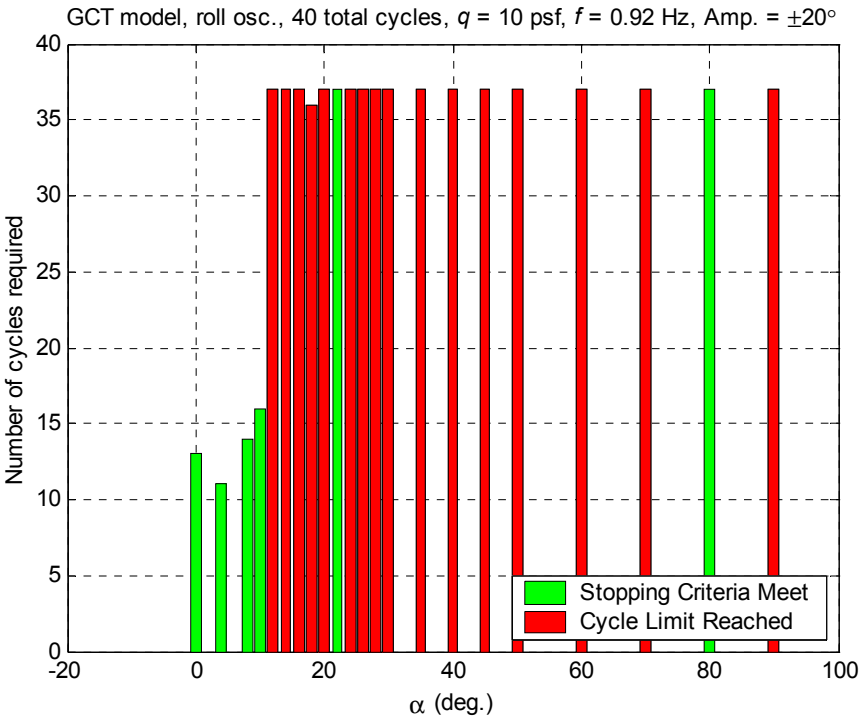

Figure 8.18 Example of post-analysis for GCT model.

9 Conclusions and Recommendations

9-1 Assessment of data integrity

Methods of providing a measure of data integrity through estimation of propagated uncertainty for body-axis aerodynamic coefficients from static and forced oscillation tests have been presented with examples. The only systematic error source of significance, relative to the random uncertainty, was the balance accuracy. It is recommended an uncertainty analysis be conducted on the balance during calibration to determine the uncertainty as a function of load. An investigation of the dynamic response of the balance is also recommended. The random uncertainty from propagation was approximately equal to the random uncertainty from direct determination of the result for the static test. Therefore any correlated random uncertainties are assumed negligible. The major contribution to the random uncertainty was due to the variation in the measured balance voltages as expected. Spectral analysis has shown significant high frequency content in the system. It is recommended a study be conducted of the effects of high frequency vibrations on static and dynamic aerodynamic coefficients. It is recommended all time histories of future tests be archived.

9-2 Efficient testing

A method for optimizing forced oscillation cycle time based on decay of uncertainty gradients and user specified threshold was presented. Utilization of the proposed procedure could reduce test time required to conduct a forced oscillation test substantially in addition to providing the test engineer with quantitative error bound estimates for the forced oscillation test results for the first time. The proposed threshold of half of the full-scale balance accuracy is certainly subject to the results of an uncertainty analysis of the balance, which should be conducted. The same approach could potentially be used to optimize when to start acquiring static data to remove any transients from setting the angle-of-attack as well as when to stop.

References

1. Owens, D. B.; Capone, F. J.; Hall, R. M.; Brandon, J. M.; Cunningham, K.; and Chambers, J. R.: Free-to-Roll Analysis of Abrupt Wing Stall On Military Aircraft at Transonic Speeds, AIAA-2003-0750.
2. Chambers, J. R. and Grafton, S. B.: Static and Dynamic Longitudinal Stability Derivatives of a Powered 1/9-Scale Model of a Tilt-Wing V/STOL Transport, NASA TN D-3591, 1966.
3. Murphy, P. C. and Klein, V.: Estimation of Aircraft Unsteady Aerodynamic Parameters from Dynamic Wind Tunnel Testing, AIAA-2001-4016.
4. Hall, R. M. and Woodson, S. H.: Introduction to the Abrupt Wing Stall (AWS) Program, AIAA-2003-0589.
5. Brandon, J. M. and Foster, J. V.: Recent Dynamic Measurements and Considerations for Aerodynamic Modeling of Fighter Airplane Configurations, AIAA-98-4447.
6. Wang, Z.; Lan, C. E.; and Brandon, J. M.: Unsteady Aerodynamic Effects of On the Flight Characteristics of an F-16XL Configuration, AIAA-2000-3910.
7. Lutze, F. H.; Fan, Y.; and Stagg, G.: Multiaxis Unsteady Aerodynamic Characteristics of an Aircraft, AIAA-99-4011.
8. Hemsch, M.; Grubb, J.; Krieger, W.; and Cler, D.: Langley Wind Tunnel Data Quality Assurance: Check Standard Results, AIAA-2000-2201, 21st AIAA Advanced Measurement Technology and Ground Testing Conference, Denver, CO. June 2000.
9. DeLoach, R.: The Modern Design of Experiments: A Technical and Marketing Framework, AIAA-2000-2691.
10. American Instituted of Aeronautics and Astronautics, Assessment of Experimental Uncertainty with Application to Wind Tunnel Testing, AIAA S-071A-1999.
11. Coleman, W. H. and Steele, W. G.: Experimentation and Uncertainty Analysis for Engineers, 2nd ed., John Wiley and Sons, New York, 1999.
12. Barlow, J. B.; Rae Jr., W. H.; and Pope, A.; Low-Speed Wind Tunnel Testing, 3rd ed., John Wiley and Sons, New York, 1999.
13. Ghee, T. A. and Kelley, H. L.: Exploratory Flow Visualization Investigation of Mast-Mounted Sights in Presence of a Rotor, NASA-TM-4634, March, 1995.
14. Shah, G. H.; Cunningham, K.; Foster, J.V.; Fremaux, C. M.; Stewart, E. C.; Wilborn, J. E.; Gato, W.; and Pratt, D. W.: Wind-Tunnel Investigation of Commercial Transport Aircraft Aerodynamics at Extreme Flight Conditions, SAE-2002-01-2912.
15. Application Note 505, Predicting Measurement Uncertainty Using Manufacturer's Specifications, http://www.neff.com/appn_505.pdf.
16. Ifeachor, E. C. and Jervis, B. W.: Digital Signal Processing: A Practical Approach, 2nd ed., Pearson Education Limited, 2002.
17. http://www.mathworks.com/access/helpdesk_r12p1/help/pdf_doc/signal/signal_tb.pdf
18. Hardin, J. C.: Introduction to Time Series Analysis, NASA-RP-1145, 1990.
19. Yigang, F and Lutze, F. H.: Identification of an Unsteady Aerodynamic Model at High Angles of Attack, AIAA Paper 96-3407, July, 1996.

Appendix A

A-1 Low-pass Inverse Fast Fourier Transform (IFFT) filter

This filter converts a digital signal to the time domain, nulls out energy at frequencies above cut-off frequency, and then converts the signal back to the time domain. The filter was designed and intended for use in MATLAB. Note the cutoff frequency must be a multiple of the fundamental frequency, ω_0 in the signal and the sample rate must be a constant.

Input:	Fs	sample rate
	x	original signal in column array or column ordered matrix
	fc	cutoff frequency
Parameters:	X	FFT of original signal
	c	index of cutoff frequency
	f	frequency array
	m	number of columns of x matrix
	n	number of rows of x matrix
Output:	y	filtered signal

Algorithm:

```
function  y = ifftfilter(Fs,x,fc)
[m, n] = size(x);
f = Fs*(0:m/2)/m;
c = find(f == fc);
X = fft(x);
y = real(ifft([X(1:(c-1),:); zeros(m-(2*c-2),n); X(m-(c-2):m,:)]));
```

Vita

The author, Eugene H. D. Heim, was born in March 1980 in St. Marys, Kansas. He received his B.S. of Aerospace Engineering in 2002 from Wichita State University. After graduation he worked as a graduate COOP at NASA Langley Research Center and came to the Aerospace and Ocean Engineering Department of Virginia Polytechnic Institute and State University for his M.S. study. He completed this work in January 2004. He has accepted a position as a Civil Servant in the Vehicle Dynamic Branch at NASA.